論文題目(Title of Thesis)

Genetic and optogenetic investigation of functional modularity in the rat brain

(遺伝学的、光遺伝学的手法を用いた、ラットにおける脳機能局在性の研究)

氏　　名(Name)　　坪田　匡史

追加情報(Additional information):

この論文の一部は以下のように出版されています。
(3 章、p.19-68)
Cofilin1 Controls Transcolumnar Plasticity in Dendritic Spines in Adult Barrel Cortex.
Tsubota T, Okubo-Suzuki R, Ohashi Y, Tamura K, Ogata K, Yaguchi M, Matsuyama M, Inokuchi K, Miyashita Y.
PLoS Biol 2015, 13(2): e1002070.
DOI:　doi:10.1371/journal.pbio.1002070
URL:
http://journals.plos.org/plosbiology/article?id=10.1371/journal.pbio.1002070

博士論文

Genetic and optogenetic investigation of functional modularity in the rat brain

(遺伝学的、光遺伝学的手法を用いた、ラットにおける脳機能局在性の研究)

坪田 匡史

Contents

1. Abstract

This thesis investigated localized functions in the rat brain via two different approaches: local gene knockdown (KD) and local optogenetic modulation of neuronal activity. The first part of the thesis examined layer- and column-restricted functions of cofilin1 (CFL1), an actin depolymerization factor expressed within dendritic spines, during circuit reorganization in the barrel cortex (**purpose i**). A lentivirus-based local RNA interference (RNAi) approach was utilized for this purpose. Rats underwent sensory deprivation of whisker input. Before initiation of sensory deprivation, lentiviral vectors were injected into layer 2/3 of the barrel column. CFL1 KD prevented experience-dependent potentiation of spared sensory input and increase in spine density in deprived-column dendritic branches that participate in transcolumnar signal processing. Thus, active reorganization of actin filaments is essential for experience-dependent plasticity in the deprived barrel column. The second part of the thesis developed a lentivirus-based technique for local perturbation of cerebellar functions via optogenetic manipulation of Purkinje cells (PCs), the sole output neurons of the cerebellar cortex (**purpose ii**). This technology showed that specific activation and inhibition of PC outputs in the cerebellar uvula, a cardiovascular regulatory region within the cerebellum, had opposing effects on resting blood pressure (BP), inducing

depressor and pressor responses, respectively. Furthermore, inhibition of PC output in the uvula attenuated BP recovery after postural change-induced BP increase, indicating that PCs in the uvula work to maintain BP during postural alterations. Taken together, the lentivirus-based experimental approaches described herein provide new insights into functional organization in the cerebral and cerebellar cortices.

2. Introduction

The cerebral cortex corresponds to the furrowed gray matter covering the cerebral hemisphere and has a number of precisely organized, functionally distinct regions. In a macroscopic view, the cerebral cortex is commonly divided into the sensory area, the motor area, and the association area. Each area can be further subdivided; for example, the sensory area can be subdivided into several specialized subregions, including the visual, auditory, and somatosensory areas. In a microscopic view, a number of functional columns exist in the cerebral cortex in which vertical clusters of neurons share the same response properties (exemplified by the receptive field in the somatosensory cortex) [1]. Such functional specializations of the cerebral cortex are thought to be mainly based on anatomical differences of input and output connectivity between each cortical region.

On the other hand, there are also genetic differences in molecular composition in the adult cortex [2] that can potentially affect various brain functions, including neuronal plasticity, which provides the foundation for learning and memory. Indeed, visual perceptual learning, during which the accuracy of visual discrimination improves after extensive training [3], sharpens neuronal receptive fields in the V4 visual area in the primate, but not in the primary visual area [4]. Similarly, there are cortical layer

differences in neuronal plasticity. In the rodent barrel cortex, for example, sensory deprivation of the principal whisker inputs affects neuronal responses in layer 2/3 (L2/3) and layer 5 (L5) neurons, but not in layer 4 (L4) neurons [5].

The existence of regional differences in molecular composition suggests that the same molecule can be differentially regulated depending on its locational context. Therefore, to empirically investigate the functions of specific molecules in, for instance, a particular cerebral cortical area, it is ideal to perturb gene expression in a single functional module-restricted manner. However, such restriction of gene manipulation has been technically difficult to achieve, especially on a cortical column and/or cortical layer scale (several hundreds of micrometers), because studies that typically use genetically modified animals rely on cell-type specific promoters for the restriction of gene manipulation.

In the first part of this thesis, I therefore aimed to address the issue of gene perturbation restriction by using a lentiviral vector-based gene knockdown (KD) technique [6] in the rat cerebral cortex (**purpose i**). Because viral vectors that are injected directly into the cortex are physically limited in their diffusion, they can be used for spatially restricted gene manipulation. Furthermore, I specifically selected lentiviral vectors for use in this work as opposed to other available vectors (e.g.,

adeno-associated viral vectors [7]), because they diffuse to a lesser extent *in vivo*.

For **purpose i**, I selected sensory-deprivation-induced, experience-dependent plasticity (EDP) in the rodent barrel cortex as an experimental model to show the impact of the local gene KD experimental approach. Each barrel column in the barrel cortex is discriminated on the basis of the barrel structure in L4, creating a barrel map that corresponds to the whisker map of the contralateral side of the face (Fig. 1a) [8]. Importantly, barrel map patterns can change in a sensory experience-dependent fashion, even in the adult cortex. In this regard, the response field corresponding to a spared whisker (or a spared column) expands during partial sensory deprivation, while that corresponding to a deprived whisker (or a deprived column) shrinks [9]. Furthermore, as mentioned above, EDP also shows inter-layer differences in the barrel cortex. These observations suggest that the molecular machineries exerted during EDP differ between the cortical layers and barrel columns, and thus, the EDP experimental model is especially well adapted to **purpose i** of my thesis.

Morphological studies have demonstrated that structural plasticity, including changes in the size and stability of dendritic spines, occurs during barrel map plasticity [10−12]. In particular, whisker deprivation induces the growth of persistent spines [10,11]. Because actin filaments are highly concentrated in dendritic spines and their

dynamics are closely related to spine shape [13], these observations indicate that the actin cytoskeleton is reorganized in these small membranous protrusions during EDP.

However, there is still no direct evidence to convincingly demonstrate how actin reorganization is actually involved in adult EDP. During actin reorganization, actin depolymerization factor (ADF)/cofilin participate critically in the regulation of the F-actin (filamentous)/G-actin (monomeric) ratio [15,16]. The activities of ADF/cofilin are reversibly regulated by phosphorylation (inactivation) and dephosphorylation (activation) at the serine-3 (Ser3) residue. The inactivation of ADF/cofilin shifts the F/G ratio towards F-actin, whereas the activation of ADF-cofilin shifts the F/G ratio towards G-actin. The inactivation and activation of cofilin are thus directly associated with spine enlargement and shrinkage, respectively [17]. Consistent with these observations, knockout of ADF/cofilin prevents both long-term potentiation (LTP) and long-term depression (LTD) in hippocampal slices [18]. Moreover, recent studies have shown that ADF/cofilin may regulate synaptic potentiation through regulation of AMPA (α-amino-3-hydroxy-5-methyl-4-isoxazolepropionic acid) receptor (AMPAR) trafficking [19,20]. These studies implicate ADF/cofilin as a predominant regulator of actin reorganization within the dendritic spine during synaptic plasticity. Nonetheless, the actions of ADF/cofilin in EDP have never before been examined.

Accordingly, the aim of **purpose i** was to investigate ADF/cofilin functions, and more particularly, cofilin 1 (CFL1) functions, in designated layers and columns of the barrel cortex. Specifically, I examined the effects of CFL1 KD on EDP in the L2/3 neurons of the deprived D2 barrel column in response to both spared and deprived whisker input during sensory deprivation. To do this, I employed a lentivirus-based RNAi approach to disrupt CFL1 gene expression *in vivo*.

I first employed wild-type (WT) rats to confirm that the responses to the spared and deprived whiskers increased and decreased, respectively, in the L2/3 neurons of the deprived D2 column during sensory deprivation. I then performed targeted electrophysiological recordings of optogenetically-labeled CFL1 KD neurons in the virus-injected rats, and showed that the response field expansion of spared whisker input was impaired, while the response field shrinkage of deprived whisker input was preserved. Morphological analysis demonstrated that the dendritic spine densities of the dendritic branches within the deprived D2 column that connect with spared D1 column projections increased in a CFL1-dependent manner, in the distal portion of the supragranular layers (layer 1 (L1) and L2/3), where most horizontal axonal projections from the spared column resided. By contrast, dendritic spine density was not affected by sensory deprivation in the proximal portion of the supragranular layers in the deprived

column, where feed forward-deprived inputs attributable to axons ascending from L4 of the same column are thought to be dominant. The sizes of the dendritic spines at transcolumnar (spared-to-deprived) connections did not change with sensory deprivation in either the distal or the proximal portion of the deprived-column supragranular layers. These observations suggest that CFL1 regulates experience-dependent functional barrel map plasticity by locally increasing dendritic spine density on the dendritic branches that participate in transcolumnar signal processing.

The second part of my thesis developed a new lentivirus-based approach for the optogenetic manipulation of the neuronal activities of Purkinje cells (PCs), the sole output neurons of the cerebellar cortex. This approach was then used for local perturbation of cerebellar functions related to the regulation of blood pressure (BP) (**purpose ii**).

The cerebellar cortex, which covers the surface of the cerebellum with finely spaced grooves, is thought to have functional modularity [21], in a manner analogous to that of the cerebral cortex. Although the cerebellar cortex has a mostly uniform cytoarchitectonic structure, anatomical studies demonstrate that the afferent and efferent

connections vary between distinct cerebellar cortical regions. These different connectivity patterns divide the cerebellar cortex into a number of longitudinal zones (Fig. 1b) [22], and electrophysiological evidence also supported this idea [23]. Moreover, regional differences are observed in the chemoarchitectonics of the cerebellar cortex. A series of marker genes expressed in PCs, such as Zebrin I, show characteristic expression patterns in this brain region, forming different patterns of parasagittal stripes (Fig. 1b) [24]. Accordingly, compartmentalizations that are based on anatomical, physiological, and/or genetic data support the presence of various cerebellar cortical functional units [21]. However, it remains poorly understood how the individual compartments contribute to specific aspects of cerebellar function [24]. This lack of understanding is due, in part, to a paucity of technologies that can specifically manipulate the activities of PCs.

Several perturbation techniques have been applied thus far to investigate the cerebellar cortical functional localization. Focal electrical microstimulation is a simple and effective technique for mapping cerebellar cortical functions. Cerebellar cortical regions related to eye blinking [25], saccadic eye movements [26], and cardiovascular regulation [27] are all mapped by using electrical microstimulation. Cerebellar cortical lesions (e.g., injuries created by tissue removal, chemical lesions, or electrolytic lesions)

have also been used to investigate the functions of different parts of the cerebellar cortex [28,29]. Although other circuits can compensate for those that are impaired by permanent lesions, reversible inactivation techniques that use either short-acting chemicals or cortical cooling largely avoid this problem [30,31].

In terms of spatial specificity, however, these techniques are associated with several drawbacks. For example, electrical stimulation preferentially activates passing fibers rather than the cell somata near the tip of the electrode [32]. Such non-specific activation may stimulate three different types of passing fibers: parallel fibers, mossy fibers, and climbing fibers. Activation of parallel fibers induced by focal electrical stimulation can spread for several millimeters along a cerebellar cortical lobule [33]. Given the longitudinal zonal organization of the cerebellar cortex, this type of electrical spread can yield non-specific effects across several different zones. By contrast, mossy fibers, which send excitatory inputs to granule cells, arise from numerous sources in the peripheral nerves, spinal cord, and brain stem. Climbing fibers originate from neurons in the contralateral inferior olive of the medulla. Antidromic activation of these fibers by cerebellar cortical electrical stimulation can therefore result in similar effects to direct stimulation of these nuclei and may cause non-specific functional modulations.

Other perturbation techniques, such as cerebellar cortical lesions and

pharmacological inactivation may also suffer from similar problems to electrical stimulation in terms of cell-type nonspecificity, making estimations of the precise tissue volumes affected by such interventions difficult. In addition, these perturbation techniques also lack fine temporal resolution. Given the importance of the temporal fidelity of PC firing in cerebellar functions [21], only a limited scope of functions can be studied with these techniques. Moreover, the lack of fine temporal resolution makes it difficult to discriminate effects caused by perturbation from compensatory mechanisms [34].

Another drawback of non-specific manipulations is that they cannot affect PC activity in a unidirectional manner, because of the non-specific effects on the stellate/basket cells that send inhibitory inputs to PCs. If non-specific stimulation simultaneously activates both stellate/basket cells and PCs, PC activities would not necessarily be increased by the stimulation. In such a case, the direction of modulation of the PC activities would be determined by the balance between the excitatory currents directly evoked by the stimulation itself and the inhibitory currents indirectly evoked through the activation of stellate/basket cells. Therefore, it is possible that the effects induced by non-specific stimulation of the cerebellar cortex are not solely the result of PC activations within a particular region of interest. Altogether, an alternative method is

necessary for precise functional mapping in the cerebellar cortex.

The aim of **purpose ii** was thus to address the issue of nonspecificity by developing a new lentiviral vector system that allows specific expression of light-sensitive proteins in PCs under the control of the L7 promoter, thereby enabling the optogenetic manipulation of PC activity. Optogenetics is a rapidly growing field that facilitates the assessment of various functions of specific cell types in diverse model organisms [35]. Illumination of neuronal populations that ectopically express specific types of engineered light-responsive proteins with precise wavelengths of light enables transient activation and inhibition of activities in these populations. Among the many reported light-responsive proteins, the microbial light-sensitive cation channel, *Chlamydomonas reinhardtii* Channelrhodopsin-2 (ChR2), and the chloride pump, *Natronomonas pharaonis* halorhodopsin (NpHR) [36], are now used widely for the activation and inhibition, respectively, of particular neuronal populations. These proteins are characterized by their fast photocycles and the ability to be genetically targeted to specific neuronal populations. For these reasons, I chose ChR2 and NpHR for manipulating PC activities.

As mentioned above, L7 (Pcp2) promoter was employed to target ChR2 and NpHR expression to PCs. The L7 promoter has been successfully utilized for PC-specific

transgene expression in transgenic mice [37−39]. Because lentiviral titers depend on the size of the packaged inserts, with larger inserts resulting in lower titers [40], short promoters are preferred. Although the L7 promoter originally used in the transgenic mice included a 4-kilobase (kb) 5' flanking region of the L7 gene [37], later work revealed that a 0.25-kb 5' flanking region is essential to achieve specific transgene expression in PCs [38]. Thus, the short sequence L7 promoter can be used in lentiviral vectors to target PCs specifically.

I first confirmed the selectivity of the transgene expression induced by the newly developed lentivirus-L7-optogenetics system. Immunohistochemical analysis conducted in lentivirus-injected rats showed that optogenetic proteins were expressed in PCs with high cell-type specificity. *In vivo* single-unit recordings of PCs revealed that almost all of the PCs expressing ChR2 or NpHR were activated or inhibited during blue or orange light illumination, respectively.

This system was next applied to the analysis of the cerebellar cardiovascular region situated within lobule IXb [41]. This was done to evaluate whether the manipulation of PC activity in opposite directions (activation versus inhibition) affected the BP in urethane-anesthetized rats. Although there is considerable evidence that electrical or chemical stimulation of lobule IXb evokes cardiovascular responses in cats and rabbits

[41−44], it is still not possible to determine the relationship between activity of PCs within lobule IXb and cardiovascular responses, because electrical or chemical stimulation cannot control PCs without affecting other neuronal types. I thus characterized this relationship by using optogenetic PC activity manipulation, and demonstrated that the ChR2-mediated photostimulation and NpHR-mediated photoinhibition of lobule IXab in rats evokes depressor and pressor responses, respectively.

Finally, I examined how the cerebellar uvula regulates BP during postural alterations in the rat. Anatomically, PCs in the uvula project to the lateral parabrachial nucleus, which then connects to the solitary tract nucleus (NTS) [43]. Since NTS neurons receive primary afferent fibers from the arterial baroreceptors, it has been suggested that cardiovascular controls by the uvula are elicited through these connections. Indeed, lesioning of the uvula significantly alters the baroreceptor reflex to increase the BP in decerebrate rabbits [45]. PCs in the uvula also project to the inferior and medial vestibular nuclei, which then mediate vestibular effects on the sympathetic nervous system during postural alterations [46]. Lesioning of the uvula affects cardiovascular responses to postural alterations in the cat [47], suggesting that the uvula regulates vestibular effects on cardiovascular responses during postural alterations. However,

chronic cerebellectomy not only affects PCs, but also other cell types, it is thus still unclear whether the previously reported effects of lesioning of the uvula on cardiovascular control were actually due to the absence of PCs. I clarified this question by demonstrating that the NpHR-mediated photoinhibition of PCs in the medial uvula dynamically altered BP maintenance during postural alterations in urethane-anesthetized rats. These observations provide direct evidence that PCs within the uvula do, in fact, participate in cardiovascular regulation during postural alterations.

To conclude this section of the document, I emphasize the overall goals of the present study: to develop new approaches for investigating functional modularity in the cerebral and cerebellar cortices, and provide new insights into functional organization in both structures.

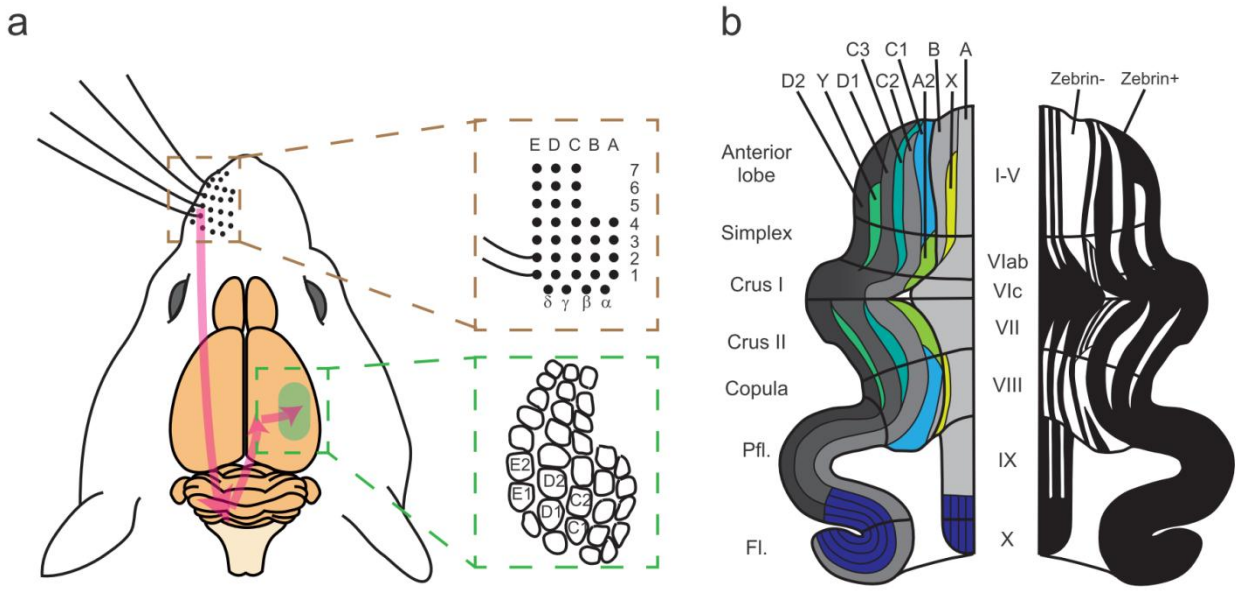

Figure 1. Schematic drawing of whisker barrel system and cerebellar cortical longitudinal zones [14] in the rat. (a) There are clear anatomical structures termed ‘‘barrels’’ in layer 4 of the primary somatosensory neocortex (S1), which are laid out in a near identical pattern to the whisker follicle pattern on the snout of the rat. The standard nomenclature for both whiskers and barrels consists of the rows A–E and the arcs 1, 2, 3, etc. (b) Longitudinal zones are illustrated on the left hemisphere of the flattened cerebellar cortex. The zones are defined by the anatomical patterns of the inferior olive climbing fiber inputs and the Purkinje corticonuclear outputs. Compartments shown in the same color are the same zone even if the compartments are spatially segregated. On the other hand, parasagittal bands defined by Zebrin I immunoreactivity are illustrated on the right hemisphere of the flattened cerebellar cortex. Zebrin I positive regions are shown in blue. Along the anterior-posterior axis, there are some discontinuities in patterns of parasagittal bands (for example between lobule VIa and VIb in the vermis). Abbreviations: Pfl, paraflocculus; Fl, flocculus. (b) was reprinted from *Behavioral Brain Research*, 255, Tsubota et al., P26-34, Copyright (2013), with permission from Elsevier.

3. CFL1 control of transcolumnar plasticity in dendritic spines during barrel map reorganization in adult rats

3.1 Materials and methods

3.1.1 Animals

All procedures were performed in accordance with a protocol approved by the University of Tokyo Animal Care Committee (Permit Number, MED: P09-092). All surgical procedures were performed under anesthesia, and all efforts were made to minimize suffering and the number of animals employed. Male Wistar rats (Nihon SLC, Shizuoka, Japan) were used for the study.

3.1.2 Whisker trimming and stimulation

A standard single whisker experience (SWE) protocol was employed [5]. All whiskers, except for the D1 whisker, on the left side of the face were trimmed by cutting the whiskers to fur level (< 1 mm) under brief isoflurane anesthesia (3%) by using an anesthetizer (MK-AT200D; Muromachi Kikai Co., Ltd, Tokyo, Japan). Ipsilateral whiskers were not trimmed. Rats were 10-weeks old at the onset of whisker trimming. Subsequently, the whiskers were re-trimmed every 2 days. Trimming was ceased at 1 week before the onset of electrophysiological recording to stimulate the growth of the trimmed whiskers.

Two neighboring whiskers (D1 and D2) were stimulated alternately by using custom-built piezo-stimulators. Each whisker was inserted under visual control into a glass capillary (inner diameter, 0.5 mm) glued to a piezoelectric bending element. A stereoscope was used to insert the whisker to a distance of 10 mm from the whisker pad. For electrophysiological recording, 200 μm ventral-dorsal deflections (10 ms at 1 Hz, repeated 50 times) were applied, resulting in an angular deflection of 1.14°. For intrinsic signal optical imaging, 1–2° amplitude ventral-dorsal deflections (50 ms at 10 Hz, repeated 50 times) were applied.

3.1.3 Intrinsic signal optical imaging

Functional maps of the barrel cortex were determined by using intrinsic signal optical imaging. The cortical surface was illuminated with a red light (wavelength, 705 nm) while stimulating a single whisker. Images were collected with a charge-coupled device (CCD) camera (Model CS8310, Tokyo Electric Industry, Tokyo, Japan) and digitized with an IBM/PC-compatible video system equipped with a video frame grabber board (Pulsar; Matrox Imaging, Quebec, Canada). The imaged area consisted of a 4.2 × 3.1 mm region with a spatial resolution of 320 × 240 pixels. Images of the surface blood vessels were photographed with the CCD camera under light with a wavelength of 540 nm. The focusing depth was adjusted to 500 μm below the cortical surface in the center

of the imaged area. For each recording trial, data were collected for 8 s with a frame length of 0.5 s (16 frames per trial). Reflectance changes in response to whisker stimulation were estimated by subtracting a 3 s averaged frame taken before the onset of whisker stimulation from a 3 s averaged frame taken at the time of whisker stimulation.

3.1.4 *In vitro* KD experiments

Oligonucleotides encoding micro RNAs (miRNAs) that target the CFL1 gene were designed with BLOCK-iT Pol II miR RNAi expression vector kits and the associated software (Invitrogen, Carlsbad, CA, USA). In this system, miRs are expressed under the control of the polymerase II promoter. The oligonucleotides encoding the designed CFL1-miRNAs (miR-CFL1_1 and miR-CFL1_2) and a negative control miRNA (miR-Neg) which has a random sequence were purchased from Invitrogen. MiR-CFL1_1 and miR-CFL1_2 target two different regions within the CFL1 gene (target sequences in CFL1 gene: miR-CFL1_1, 5'-AGGAATCAAGCACGAATTACA -3'; miR-CFL1_2, 5'-GTTCGCAAGTCTTCAACGCCA-3').

Human embryonic kidney (HEK) 293T-cells (for mRNA level KD) or rat phenochromocytoma (PC)-12 cells (for protein level KD) were used for the *in vitro* experiments. Plasmid vectors that express miR-CFL1 (pcDNA6.2-GW/EmGFP-miR vector, Invitrogen) and rat CFL1 gene (pCAG-rCFL1, kind gift from Dr. J. Noguchi,

University of Tokyo School of Medicine) were co-transfected to HEK293T cells. Three days after the transfection, total RNA was prepared and used as a template for real-time reverse-transcriptase PCR with the *StepOne*^{TM} Real-Time PCR system (Applied Biosystems, Carlsbad, CA, USA) to confirm the KD of CFL1 mRNA *in vitro*.

HEK293T cells (for mRNA level KD) or rat PC-12 cells (for protein level KD) were used for the *in vitro* experiments. For miRNA screening (Fig. 2a), plasmid vectors expressing miR-CFL1 (pcDNA6.2-GW/EmGFP-miR vector, Invitrogen) and the rat *CFL1* gene (pCAG-rCFL1, the kind gift of Dr. H. Kasai, University of Tokyo) were co-transfected into the HEK293T cells. Three days after transfection, total RNA was prepared and used as a template for real-time reverse-transcriptase PCR with the *StepOne*^{TM} Real-Time PCR system (Applied Biosystems).

For confirmation of the KD efficiencies of the miRNAs for the endogenous CFL1 protein (Fig. 2b and Supplementary Fig. 1a), the PC-12 cells (1×10^5) were transfected with the Lenti-CMV-hChR2-eYFP-miR-CFL1_1 or -miR-CFL1_2 vector (2.0×10^7 gc). Four days later, the cells were solubilized and the cell extracts were obtained. The extracts were immunoblotted by using following antibody combinations: rabbit antibody to cofilin (1:250; Cytoskeleton, Watertown, MA, USA)/horseradish peroxidase-conjugated antibody to rabbit IgG (1:2000; Rockland Immunochemicals Inc.,

Gilbertsville, PA, USA), or mouse antibody to β-actin (1:5000; Sigma-Aldrich)/horseradish peroxidase-conjugated antibody to mouse IgG (1:1000; Vector Laboratories, Inc., Burlingame, CA, USA). The band intensities were quantified by using ImageJ software (National Institutes of Health, Bethesda, MD, USA).

3.1.5 Lentiviral preparation

Three microRNA (miR)-based Lenti-CaMKIIα-hChR2-eYFP-miR vectors were produced for the *in vivo* electrophysiology experiments. These vectors co-expressed ChR2-enhanced yellow fluorescent protein (eYFP) as a light-activatable tag and miR-CFL1_1, miR-CFL1_2, or miR-Neg for the manipulation of CLF1 gene expression under the control of the CaMKIIα (Ca^{2+}/calmodulin-dependent protein kinase II) promoter. Three additional vectors were produced for the morphology experiments (analysis of spine density, spine area, and axonal density): the Lenti-CMV-tdTomato-WPRE vector, which expressed tdTomato under the control of the cytomegalovirus (CMV) promoter, and two Lenti-CaMKIIα-eGFP-miR vectors, which co-expressed enhanced green fluorescent protein (eGFP) and either miR-CFL1_1 or miR-Neg under the control of the CaMKIIα promoter. The lentiviral vectors were produced by co-transfection of HEK 293T-cells with a mixture of four plasmids by using the calcium phosphate precipitation method [48,49].

Briefly, 5×10^6–1×10^7 HEK 293T-cells were seeded onto a 150-mm^2 tissue culture dish (Iwaki Co., Ltd., Tokyo, Japan) in 25 ml of culture medium at 24 h before transfection. The four-plasmid mixture consisted of pCAGkGP1.1R (15 μg), pCAG4RTR2 (5 μg), pCAG-VSV-G (5 μg) [50], and transfer vector plasmid (25 μg). The plasmids were mixed and diluted to a total volume of 1.125 ml with double-distilled water, and 125 μl of 2.5M $CaCl_2$ was then added. Subsequently, 1.25 ml of two-fold concentrated (2 ×) HBSP buffer (280 mM NaCl, 50 mM HEPES, 1.5 mM Na2HPO4, 10 mM KCl, and 12 mM glucose, pH 7.00–7.05) was added dropwise while vortexing, and the precipitate was immediately added to the cultures. Sixteen hours after transfection, the cells were washed twice with phosphate buffered saline (PBS) and cultured in 20 ml of medium for an additional 24 h.

The conditioned medium containing lentiviral vector particles was harvested at 40 h after transfection, cleared by low-speed centrifugation, filtered through a 0.22 μm low protein-binding membrane, and centrifuged at 25,000 rpm for 90 min in a SW-28 rotor (Beckman Coulter, Brea, CA, USA). After centrifugation, the lentiviral pellets were resuspended in PBS at 4°C. Aliquots were quick-frozen and maintained at -80°C until use.

Next, titers of virus stocks were determined by the DNA titration method [51].

Serial dilutions of viruses were added to 4×10^5 HEK 293T-cells growing as a monolayer in six-well plates in 2 ml of culture medium. After 24 h, the medium was changed and the culture was continued for another 2 days. Genomic DNA (gDNA) from approximately $1-10 \times 10^5$ vector-transduced cells was then isolated by using the FastPure DNA Kit (Takara Shuzo, Co., Ltd.). The primers for quantitative real-time PCR analysis, eYFP-F (5'-CAA CAT CGA GGA CGG CAG-3') and eYFP-R (5'-CTC CAG CAG GAC CAT GTG-3'), were designed with the Primer Express software program and obtained from Applied Biosystems.

PCR reactions and data analysis were performed using the *StepOne*™ Real-Time PCR system (Applied Biosystems). The gDNA was diluted in the provided buffer, and 2 μl of the gDNA solution was mixed with 18 μl of a PCR master mix containing 1 × Fast SYBR Green Master Mix and 0.9 μM each of the forward and reverse primers. For the negative control, a gDNA solution (2 μl) from non-transduced cells was used.

Amplifications were performed that consisted of one cycle of 95°C for 20 sec, and 40 cycles of 95°C for 1 sec and 60°C for 20 sec. Amplification of the eYFP sequence-containing vector plasmid DNA for the generation of a standard curve was performed by using concentrations of the plasmids ranging from 10^7 molecules/μl to 10^2 molecules/μl, as determined by spectrophotometry with an Ultrospec (model 4000)

instrument (GE Healthcare, Buckinghamshire, UK). Plasmid DNA used for standard curve generation was diluted with gDNA from non-transduced cells to control for any inhibitory effect of the gDNA on the PCR reaction. All reactions were carried out in duplicate. The number of vector DNA molecules in the transduced cells was calculated by comparing threshold cycle values (C_T) of experimental samples to those of the plasmid standard curve. Copy numbers of gDNA were estimated by using the TaqMan Copy Number Reference Assay (Applied Biosystems). In determining the final DNA titers of the lentiviral vectors, the total number of vector DNA molecules in the transduced cells was corrected for dilution and the copy number of the gDNA.

3.1.6 Lentiviral injection into rats

Rats were 8 weeks old at the time of lentiviral vector injection. Each rat was anesthetized with inhaled isoflurane (3% induction, 1% maintenance) and positioned in a stereotaxic apparatus (SR-6R; Narishige, Tokyo, Japan). A midline sagittal incision was made, and the skull over the barrel cortex was carefully thinned to create a cranial window.

For electrophysiology experiments, the D2 barrel column was first identified via intrinsic signal optical imaging, and a glass pipette (tip diameter, ~40 μm) attached to a 1-μl Neuros syringe (7001 KH; Hamilton Company, Reno, NV, USA) was then

vertically inserted into the center of the D2 barrel column to a depth of 300 μm from the cortical surface. Next, a solution (200 nl; 1.0×10^{10} gc/ml stock solution) of the lentiviral vector (Lenti-CaMKIIα-hChR2-eYFP-miR vector containing the miR-CFL1_1, miR-CFL1_2, or miR-Neg sequence, n = 9, 4, and 3 rats, respectively) was injected at a flow rate of 25–50 nl/min with the aid of a micropump (UltramicroPump III; World Precision Instruments (WPI), Sarasota, FL, USA) and a microprocessor-based controller (Micro4; WPI). The needle was left in place for 15 min, at which time it was retracted from the brain. The scalp incision was carefully sutured, and the rat was returned to a standard cage after recovering from anesthesia.

For morphology experiments, both the D1 and the D2 barrel column were functionally identified via intrinsic signal imaging prior to lentiviral vector injection. Solutions containing either the Lenti-CMV-tdTomato-WPRE vector (200 nl; 1.0×10^{10} gc/ml) or the Lenti-CaMKIIα-eGFP-miR vector (200 nl; 3.0×10^{8}–1.0×10^{9} gc/ml; miR-CFL1_1, n = 3 rats; miR-Neg, n = 7 rats) were then injected into the central region of the D1 and the D2 barrel column, respectively.

3.1.7 *In vivo* electrophysiological recording

Each rat was anesthetized with ethyl carbamate (1.2 g/kg). The body temperature was maintained at 37.5°C throughout the experiment. A catheter (inner diameter, 0.5 mm;

outer diameter, 0.9 mm; polyethylene tube SP35; Natsume Seisakusho, Tokyo, Japan) was surgically inserted into the left femoral vein. Ringer's solution and additional doses of anesthesia (urethane, 0.2–0.4 g/kg) were then administered through the catheter. The skull over the barrel cortex was exposed and carefully removed. In vivo eYFP fluorescence was identified by using a cooled CCD camera (VB-7000; Keyence, Osaka, Japan) attached to a fluorescence stereoscopic microscope (VB-G05; Keyence).

The activities of single neurons were recorded extracellularly from the viral-injected site by using a glass-coated tungsten microelectrode (resistance < 1 MΩ) in WT rats, or a glass-coated tungsten optrode (resistance < 1 MΩ) [52] in virus-injected CLF1 KD rats. The electrode was vertically inserted into the cortex via a hydraulic micromanipulator (MO-10; Narishige). Neuronal signals were amplified with an AB651J amplifier (Nihon Kohden, Tokyo, Japan), band-pass filtered (0.4–5 kHz filter; Nihon Kohden), digitized at 25 kHz, and stored by using the Recorder Software (Neural Data Acquisition System, Plexon, TX, USA). Stored data were analyzed offline with the Offline Sorter program (Plexon) for sorting multi-unit data into single-unit data by waveform analysis. Single-unit data were analyzed with MATLAB software (Mathworks, MA, Natick, USA).

Recordings were performed from both L2/3 (depth from the pial surface, 0–500 μm)

and L5 (depth, 800–1250 μm) [53,54] neurons. In some cases, electrolytic lesions (1 μA, 5 sec, tip negative) were applied at a depth corresponding to L4 (750 μm) to map recording locations onto the barrel pattern (later visualized by cytochrome oxidase staining).

In parallel with the single-unit recordings, cortical electroencephalograms (EEGs) were also recorded to monitor the cortical state. A stainless steel screw was threaded into the bone above the occipital cortex (6 mm posterior from the bregma, 3.5 mm lateral from the midline). For reference, another screw was threaded into the bone above the cerebellum. Signals were amplified with an AB-610J amplifier, band-pass filtered (0.5–100 Hz), and stored. During whisker stimulation trials, anesthesia was maintained to a depth equivalent to stage III slow-wave sleep, as described previously[55].

3.1.8 Optical stimulation

A fiber in the optrode was coupled to a diode-pumped solid-state (DPSS) laser (peak wavelength at 473 nm, 200 mW; beam diameter, 2.0 mm; CNI Optoelectronics, Changchun, China). The timing of the stimulation was managed with an electrically controlled mechanical shutter (Model LS3, UNIBLITZ, Rochester, NY, USA). The light power was controlled with a Neutral Density (ND) filter (Thorlabs, Newton, NJ, USA). For each neuron, 10 × 10 light pulse trains, each with a duration of 5 ms, were delivered

at 1, 5, 10, 20, and 40 Hz. The interval between each train was 15 s. The light intensity was adjusted after observing the neuronal responses so as to avoid the skew of light-evoked spike waveforms from spontaneous spike waveforms [56]. More specifically, I used the maximum light intensity that did not skew waveforms under visual inspection. The light power at fiber input was in the range of 0.1–5 mW.

3.1.9 Histology and cell counting

Rats were perfused with saline, followed by 4% paraformaldehyde in phosphate buffer. The brains were post-fixed in 4% paraformaldehyde for 2−4 h and immersed in a solution of 20% sucrose in PBS.

To recover the location of the electrophysiological recordings and virus expression, the cortex was flattened between two glass slides, sectioned at 50 μm, and processed for cytochrome oxidase staining (2−3 h at room temperature (RT) in 20 ml phosphate buffer containing 10 mg diaminobenzidine (DAB), 10 mg cytochrome c, and 0.8 g sucrose) [57]. Blood vessels were used as a reference for projecting the barrel patterns in L4 onto the L2/3 sections where the eYFP fluorescence was observed.

For the detection of microtubule-associated protein 2 (MAP2) or neuronal-specific nuclear protein (NeuN) in selected neuronal populations, coronal sections (25 μm thick) were immunostained with either mouse anti-MAP2 antibody (1:2000; Sigma-Aldrich,

St. Louis, MO, USA) or mouse anti-NeuN antibody (1:1000; Millipore). The sections were reacted with an Alexa Fluor 647-conjugated anti-mouse secondary antibody (1:500; Invitrogen). Sections were counterstained with the DNA-specific fluorescent dye, Hoechst 33342 (Invitrogen). For CFL1 staining, sections were immunostained with a rabbit anti-cofilin antibody (1:250), followed by a horseradish peroxidase-conjugated anti-rabbit secondary antibody (Dako Corporation, Glostrup, Denmark) and DAB. Two successive sections were processed for NeuN and CFL1 staining, respectively, to confirm the lentiviral-mediated KD of the CFL1 protein. The stained images were obtained by using a BZ-9000 fluorescence microscope (Keyence) and a TCS-SPE confocal microscope (Leica, Solms, Germany).

MAP2-stained sections were used to count the percentages of the eYFP+ neurons in each cortical layer. Layers were manually identified based on differences in cell density and size in sections that were double-stained for MAP2 and Hoechst. Three non-adjacent sections were chosen that encompassed each injection point, and all eYFP+ neurons were counted in each section.

3.1.10 Morphometric analysis spine density, spine area and axonal density analysis

For all morphological analyses, parasagittal sections (50 μm thick) were prepared from the rat cortex that included both the D1 column and the D2 column. Sections were

immunostained with chicken anti-GFP antibody (1:1000; Abcam, Cambridge, UK) and rabbit anti-DsRed antibody (1:1000; Takara Shuzo), followed by Alexa Fluor 488-conjugated anti-chicken (1:500; Invitrogen) and Alexa Fluor 546-conjugated anti-rabbit (1:500; Invitrogen) secondary antibodies.

For morphometric analysis of dendritic spine density and area, confocal immunofluorescence images (voxel size, 0.1 × 0.1 × 0.5 μm^3) were acquired with a CSU-22 spinning-disc confocal unit (Yokogawa Electric, Tokyo, Japan) coupled to an Axiovert 200M microscope through a Plan Apochromat 63× objective (NA 1.4; Carl Zeiss, Göttingen, Germany). The acquired images were then analyzed by using MetaMorph software (Universal Imaging Corporation, West Chester, PA, USA). Given sets of tdTomato+ D1 axons and eGFP+ D2 dendritic spines were defined as synaptically connected if both fluorescent signals were found within the same voxel.

The density of the dendritic spines (including all types of spines, e.g., thin, mushroom-shaped, and stubby spines) was measured at dendritic branch segments that met the following criteria: 1) the segment was nearly parallel to the xy plane (1280 × 1010 pixels) in a stacked image of consecutive focal planes (typically, 10–50 stacked planes) taken at 0.5 μm intervals in the z direction; 2) at least one putative synaptic connection with a tdTomato+ axon was identified; 3) no bifurcations were present

within the segment; 4) the segment demonstrated no crossing with other branches. Branch segments in which the total measured length was less than 10 μm were discarded. Spines within 15 μm of the identified putative synaptic connection were counted, along with dendritic length. In some cases (8 of 51 dendrites in the distal portion and 5 of 41 dendrites in the proximal portion), two or more connections were identified on a single dendritic branch. If distance between a given connection pair was less than 2 × 15 μm (5 of 8 in distal and 4 of 5 in proximal), two connections were regarded as forming a single branch segment. If this was not the case (3 of 8 dendrites in distal and 1 of 5 in proximal), two connections were regarded as forming different branch segments with each other. I also measured spine densities within 30 μm from connections using the same criteria.

For measurement of dendritic spine area, the fluorescence images were first thresholded, where the threshold was more than the mean plus 5 × the standard deviation (SD) of the background intensity distribution. Spines that made synaptic connections with D1 axons were then identified. Next, a two-dimensional (2D) projection image was reconstructed from the z planes that included the identified spine. Spine area was estimated in the 2D image by manually enclosing the spine head, followed by measurement of the total pixel number included within the enclosure. All

types of spine morphologies were included in the analysis. Furthermore, all measurements of spine density and spine area were performed by investigators who were blind to the animal's sensory experience and the identity of the injected virus.

For analysis of axonal density, fluorescence images were acquired with a BZ-9000 microscope through a Plan Apochromat 20× objective (NA 0.75; Nikon, Tokyo, Japan). The intensity of the tdTomato fluorescence attributable to D1 column axons was measured within a region of interest (vertical dimension, 50 μm; horizontal dimension, 100 μm) localized within the D2 column where the eGFP signal was observed. The region of interest was vertically scanned from the surface of the cortex to the superior end of L4 (a depth of 500 μm from the cortical surface). Measurements were performed in three sections for each rat. The determined intensity of the tdTomato fluorescence was normalized to the value of both the maximum intensity and the background intensity measured within L4 for each section, and then averaged across the three sections.

3.1.11 Electrophysiology data analysis

Data analysis was performed with MATLAB software. Light-responsive neurons were identified by comparing firing rates as a function of stimulation latency during the first 100 ms after each light pulse with the firing rates obtained for similar time blocks after

shuffling the spike times of each cell within an interval [–100, +100 ms] around the light stimulus [58]. After each shuffling, spikes were counted in 1-ms bins, and the three successive bins with the maximum number of spikes during the 100-ms period after the stimulation were identified. For each cell, the spike times were shuffled 10,000 times. Three successive bins with a maximum number of spikes were also identified for the real data. Cells were classified as light-responsive if the number of spikes in the block with the maximal number of spikes in the real data exceeded the 99.9th percentile value of the distribution of the maximum number of spikes in the shuffled data. The latency of the response was taken as the mean latency of all spikes contributing to this three-bin block.

Repetitive light pulses were applied to each neuron to examine the probability of firing in response to high-frequency optical stimulation [59]. The first light pulse in each 10-pulse train was excluded from the analysis. The number of spikes evoked by 90 light pulses was estimated as the spike number detected during the 25 ms after light onset subtracted by the spike number detected during the 25 ms before light onset. For 40-Hz stimulation, the width of the window was set at 15 ms.

Recording locations were reconstructed based on the relative location of the lesion marks within the barrel patterns, as visualized by cytochrome oxidase staining in

tangential sections. To allocate each recording location within the D2 barrel column to three distinct areas according to the distance from the D1 barrel column, the center of the mass was calculated for both columns. A line passing through the center of both D1 and D2 was drawn, and the line was quartered within the D2 column. Each recording location was then vertically projected onto the line. When a projected location was included within I) the nearest portion, II) the second nearest portion, or III) the third nearest and/or the farthest portion of the line relative to the D1 column, the location was allocated to area I, II, or III, respectively.

All statistical tests for the *in vivo* study were performed with MATLAB and freely available R software. Data are given as the means, and error bars denote the standard error of the mean (SEM), except when indicated otherwise.

3.2 Results

3.2.1 D2 column- and L2/3-restricted KD of the *CFL1* gene

To manipulate *CFL1* gene expression, I used a microRNA (miRNA)-based gene KD system in which the polymerase II promoter was available for driving miRNA expression [6]. Because several weeks are typically required for the induction of EDP [60,61], I employed a lentiviral vector for the stable *in vivo* expression of miRNA for

CFL1 KD (Fig. 2c). The vectors co-expressed channelrhodopsin-2 (ChR2)-enhanced yellow fluorescent protein (eYFP), with ChR2 as a light-activatable tag for extracellular single-unit recordings [56,58,59] and eYFP as a fluorescent marker of CFL1 KD neurons, under the control of the excitatory neuron specific Ca^{2+}/calmodulin-dependent protein kinase II alpha (CaMKIIα) promoter [62].

Targeted injection of the lentiviral vector into the right D2 barrel column of rats was achieved by functionally identifying the column center via intrinsic signal optical imaging (Fig. 3a-d) [63]. For intrinsic signal imaging, the reflected light (705 nm) by the cortex was monitored to detect changes in blood flow derived from local neuronal activity induced by whisker stimulations (Fig. 3c) [64]. Single column-restricted expression of eYFP was confirmed in tangential sections that were processed via cytochrome oxidase staining (Fig. 3e,f) [57]. By targeting the vector injection to a shallow depth within the cerebral cortex (~300 μm from the pial surface), viral infection was restricted to L2/3 (Fig. 4a), and strong eYFP expression was confined to L2/3 (Fig. 4a). Due to the existence of axonal projections from L2/3 to L5 [65], weak fluorescence derived from eYFP-positive axons originating from L2/3 neurons was observed in L5 (Fig. 4b). Immunostaining of a neuronal marker, microtubule-associated protein 2 (MAP2), confirmed that most of the eYFP+ neurons resided within L2/3, whereas

eYFP+ neurons were rarely found in L5 (90.1% in L2/3 vs. 0.2% in L5) (Fig. 4b,c). These results demonstrate that viral expression was mostly restricted to the L2/3 neurons in the D2 barrel column.

In the present study, the CFL1 KD experiments made use of a negative control miRNA (miR-Neg) and two miRNAs (miR-CFL1_1 and miR-CFL1_2) with different target sequences within the *CFL1* gene. The KD efficiencies of miR-CFL1_1 and miR-CFL1_2 were first assessed *in vitro*. Both miRNAs showed high KD efficiency at the mRNA level in rat CFL1-overexpressing human embryonic kidney (HEK) 293T cells (miR-CFL1_1, 95.0 ± 0.9%; miR-CFL1_2, 89.3 ± 0.3%; n = 3; $P < 0.001$ vs. miR-Neg, Tukey's multiple comparison test) (Fig. 2a). Similar results were observed at the protein level in rat pheochromocytoma-12 (PC12) cells (miR-CFL1_1, 96.8 ± 1.5%; miR-CFL1_2, 83.8 ± 5.7%; n = 3; $P < 0.01$ vs. miR-Neg) (Fig. 2b). I next confirmed CFL1 KD *in vivo*. CFL1 protein expression is observed in neuronal somata, dendritic spines and astrocytes in the normal cortex [66]. Immunostaining of CFL1 in a miR-CFL1_1-expressing rat showed that CFL1 expression decreased locally in a L2/3 subregion corresponding to the region where eYFP expression was observed in the adjacent section (Fig. 5a). This is in clear contrast with the miR-Neg-expressing control section, where no decrease in CFL1 protein expression was observed (Fig. 5b).

3.2.2 ChR2-assisted identification of KD neurons

In the present study, recordings were only taken from regular-spiking neurons (Cauli et al., 1997) (Fig. 6a-c). Because miR-CFL1 and ChR2 were co-expressed (Fig. 2c) [6], I searched CFL1 KD neurons with illuminating light in extracellular single-unit recordings. However, due to the presence of local excitatory connections between L2/3 pyramidal neurons [67], ChR2– neurons can also be activated by light through the excitatory drive from surrounding ChR2+ neurons in L2/3 [56,59]. Therefore, light-responsive ChR2– neurons should be discriminated from ChR2+ neurons for the proper identification of CFL1 KD neurons.

I performed this discrimination by comparing the response reliability [52] of light-responsive L2/3 neurons (the combined population of ChR2+ and ChR2– neurons) to repetitive light (20 Hz) stimulation with that of light-responsive L5 neurons (a pure population of ChR2– neurons) (for details, see Experimental procedures). Putative ChR2+ L2/3 neurons were defined as those neurons exhibiting a higher reliability than the neuron which showed the highest reliability in L5 (Fig. 7a-d). A comparison of the response latency distributions between L2/3 and L5 neurons showed a tendency such that the putative ChR2+ neurons in L2/3 fired at a faster latency to light pulses than putative ChR2– neurons in L2/3 and light-responsive neurons in L5 (Fig. 8a-d), which

is consistent with earlier observations [58], although no statistically significant differences were discerned (L2/3 ChR2+ vs. L2/3 ChR2−, $P = 0.22$; L2/3 ChR2+ vs. L5 light-responsive, $P = 0.11$, Kolmogorov-Smirnov test).

3.2.3 CFL1 KD impairs experience-dependent expansion of spared whisker representation

To examine the effects of CFL1 KD on EDP, lentiviral vectors were injected at 2 weeks before the onset of sensory deprivation (Fig. 9a). Sensory deprivation was induced by using the single whisker experience protocol [60,68], in which all whiskers but the D1 whisker were trimmed on the left side of the face. I first confirmed that the L2/3 neurons in the D2 column of the right hemisphere showed increased responses to spared D1 whisker stimulation after sensory deprivation in wild-type (WT) rats (WT non-deprived vs. WT deprived, $P < 0.01$, Tukey-Kramer multiple comparison test) (Fig. 9b-e). This observation indicates that the cortical representation of spared whisker inputs expanded into surrounding deprived columns. In contrast, the neuronal response increase was almost completely absent in the putative ChR2+ neurons from which recordings were taken in the miR-CFL1_1-expressing deprived rats (WT deprived vs. miR-CFL1_1 deprived, $P < 0.01$) (Fig. 9c-e). On the other hand, expression of miR-CFL1_1 in non-deprived rats did not affect neuronal responses to D1 stimulation

(WT non-deprived vs. miR-CFL1_1 non-deprived, $P = 0.90$) (Fig. 9c-e), indicating that CFL1 KD in and of itself does not decrease responses to the D1 whisker.

I performed two additional control experiments. The first control experiment demonstrated that the enhanced spared whisker response was not altered in neurons in which miR-Neg and ChR2-eYFP were co-expressed (WT deprived vs. miR-Neg deprived, $P = 0.98$) (Fig. 10a). This suggests that the overexpression of miRNA and ChR2-eYFP itself does not affect the expansion of spared input representation. The second control experiment demonstrated that CFL1 KD with miR-CFL1_2 also impaired the increase in the spared whisker response as well as miR-CFL1_1 (WT deprived vs. miR-CFL1_2 deprived, $P < 0.01$) (Fig. 10a). This suggests that the observed effects were not due to "off-target" actions of miR-CFL1 [69].

To exclude the possibility that biased recording locations within the D2 column affected my results, I performed another analysis. Recording locations in the D2 column were reconstructed based on lesion marks (Fig. 11a,b). Responses recorded from CFL1 KD neurons of deprived rats were lower than that recorded from WT deprived rats, regardless of the distance from the D1 column (Fig. 11c) and the cortical depth (Fig. 11d) (comparison of distance distribution, WT deprived vs. miR-CFL1_1 deprived, $P = 0.37$; comparison of depth distribution, WT deprived vs. miR-CFL1_deprived, $P = 0.19$,

Mann-Whitney's U-test). Accordingly, the observed effects of CFL1 KD in this study were not due to recording location bias.

3.2.4 CFL1 KD preserves experience-dependent shrinkage of deprived whisker representation

I first confirmed that the L2/3 neurons in the D2 column showed decreased responses to deprived D2 whisker stimulation after sensory deprivation in WT rats (WT non-deprived vs. WT deprived, $P < 0.01$, Tukey-Kramer multiple comparison test) (Fig. 12a-c). This process is indicative of the shrinkage of deprived whisker input representation. I then examined the effects of CFL1 KD on this process, and found that experience-dependent response decrease to the deprived D2 whisker was preserved in either miR-CFL1_1-expressing neurons (WT deprived vs. miR-CFL1_1 deprived, $P = 0.89$) (Fig. 12b,c) or miR-CFL1_2-expressing neurons (WT deprived vs. miR-CFL1_2 deprived, $P = 0.89$) (Fig. 10b). Expression of miR-CFL1_1 in non-deprived rats did not affect L2/3 neuronal responses to D2 stimulation (WT non-deprived vs. miR-CFL1_1 non-deprived, $P = 0.81$) (Fig. 12b,c), suggesting that CFL1 KD itself does not affect L2/3 neuronal responses to whisker stimulation.

Taken together, these results suggest that CFL1-mediated actin dynamics is necessary for the experience-dependent expansion of spared input representation in L2/3,

but not for the experience-dependent shrinkage of deprived input representation.

3.2.5 CFL1-dependent increases in dendritic spine number during functional barrel map plasticity

Together with the fact that CFL1 is a predominant regulator of dendritic spine structure [17], my findings raise the possibility that CFL1-mediated structural modifications selectively occur at dendritic spines that synaptically connect with horizontal transcolumnar axons emanating from the spared barrel column.

To investigate this hypothesis by observing dendritic spine structure, I constructed a new set of lentiviral vectors expressing either tdTomato or eGFP/miRNA (Fig. 13a,b). Injection of these vector solutions was targeted to the D1 column (tdTomato) or the D2 column (eGFP/miRNA) by using intrinsic signal optical imaging (Fig. 13c). To avoid dense neuronal expression of eGFP, a lower-titer solution of the eGFP/miRNA co-expressing vector (3.0×10^8–1.0×10^9 gc/ml) was employed in this experiment (Fig. 13d,e) compared with the vector solutions employed in the other experiments (1.0×10^{10} gc/ml).

I first found that the tdTomato intensity emanating from the D1 axons peaked at 150–200 μm from the cortical surface in the D2 column, and decreased with cortical depth (Fig. 14a-c). This was in clear contrast to the vertical profile of L4 input strength

[70], which was fairly weak at shallow depths and stronger at deeper zones, forming a complementary pattern with that of the D1 axonal intensity profile (Fig. 14c). There was a significant difference in tdTomato intensity between the distal (0–200 μm from the cortical surface) and proximal (200–500 μm) portion ($P < 0.05$, paired *t*-test) (Fig. 14d). These results suggest that a greater number of transcolumnar synaptic connections from the D1 column are generated in the distal portion of the D2 column than in the proximal portion at which the ascending deprived axonal inputs from L4 are thought to predominate. I next tested the effects of sensory deprivation on dendritic spine number in the miR-Neg (non-deprived and deprived) groups. Learning/experience-driven dendritic spine formation and synaptic plasticity spatially cluster on dendritic branches in cortical pyramidal neurons [71–73], and thus dendritic spine densities were measured around (< 15 μm) transcolumnar synaptic connections (Fig. 14e). In non-deprived rats, spine densities were relatively low at the cortical region just below the surface and increased with depth, while densities were nearly constant throughout the supragranular layer in deprived rats (comparison of slopes of regression lines, miR-Neg non-deprived vs. deprived, $F_{1,63} = 9.33$, $P < 0.005$, *F*-test) (Fig. 14f).

These results demonstrate that sensory deprivation affects dendritic spine numbers in a cortical depth-dependent manner. I thus separately compiled dendritic spine

densities measured at distal and proximal portions of the D2 column supragranular layer, and examined the impact of CFL1 KD on these values. In the distal portion, spine densities significantly increased with sensory deprivation in the control miR-Neg-expressing neurons (miR-Neg non-deprived vs. miR-Neg deprived, $P < 0.005$, Student's *t*-test with Bonferroni correction), but this increase was impaired in the CFL1 KD neurons (miR-Neg deprived vs. miR-CFL1_1 deprived, $P < 0.005$) (Fig. 15a-c). In contrast, sensory deprivation did not affect dendritic spine densities in the proximal portion of the supragranular layer (miR-Neg non-deprived vs. miR-Neg deprived, $P = 0.34$; Fig. 15d-f). Importantly, the same conclusion was reproduced even if dendritic spine densities were measured in a broader region around transcolumnar connections (< 30 μm) (distal; 1.06 ± 0.07, 1.34 ± 0.05, and 1.08 ± 0.01 spines/μm for miR-Neg non-deprived, miR-Neg deprived, and miR-CFL1 deprived groups, respectively; mean ± SEM; $P < 0.005$ for miR-Neg non-deprived vs. miR-Neg deprived, and miR-Neg deprived vs. miR-CFL1 deprived, Student's *t*-test with Bonferroni correction) (proximal; 1.31 ± 0.06, 1.23 ± 0.05, 1.29 ± 0.08 spines/μm for miR-Neg non-deprived, miR-Neg deprived, and miR-CFL1 deprived groups, respectively). These observations suggest that during sensory deprivation, CFL1-mediated actin dynamics causally regulate the spine numbers around dendritic spines receiving horizontal transcolumnar synaptic

inputs from the spared D1 column. Moreover, these events take place in the distal portion of the D2 column supragranular layer, where dense horizontal transcolumnar projections reside.

In addition to the dendritic spine density, I also analyzed the sizes of the D2 spines that made putative synaptic connections with horizontally projecting D1 axons. Sensory deprivation did not influence spine sizes in miR-Neg-expressing neurons in either the distal or the proximal portion (distal, $P = 0.70$; proximal, $P = 0.70$; Student's *t*-test) (Fig. 16a,b). In agreement with a previous observation regarding the hippocampal neurons of CFL1 knockout mice [18], spine sizes increased in CFL1 KD neurons in the distal portion (miR-Neg non-deprived vs. miR-CFL1_1 deprived, $P < 0.05$; miR-Neg deprived vs. miR-CFL1_1 deprived, $P < 0.05$, Student's *t*-test with Bonferroni correction) (Fig. 16a,b). However, this increase did not correlate with the neuronal response changes described above (Figs. 9 and 12), suggesting that the observed spine size changes might not contribute to the functional barrel map plasticity induced by sensory deprivation.

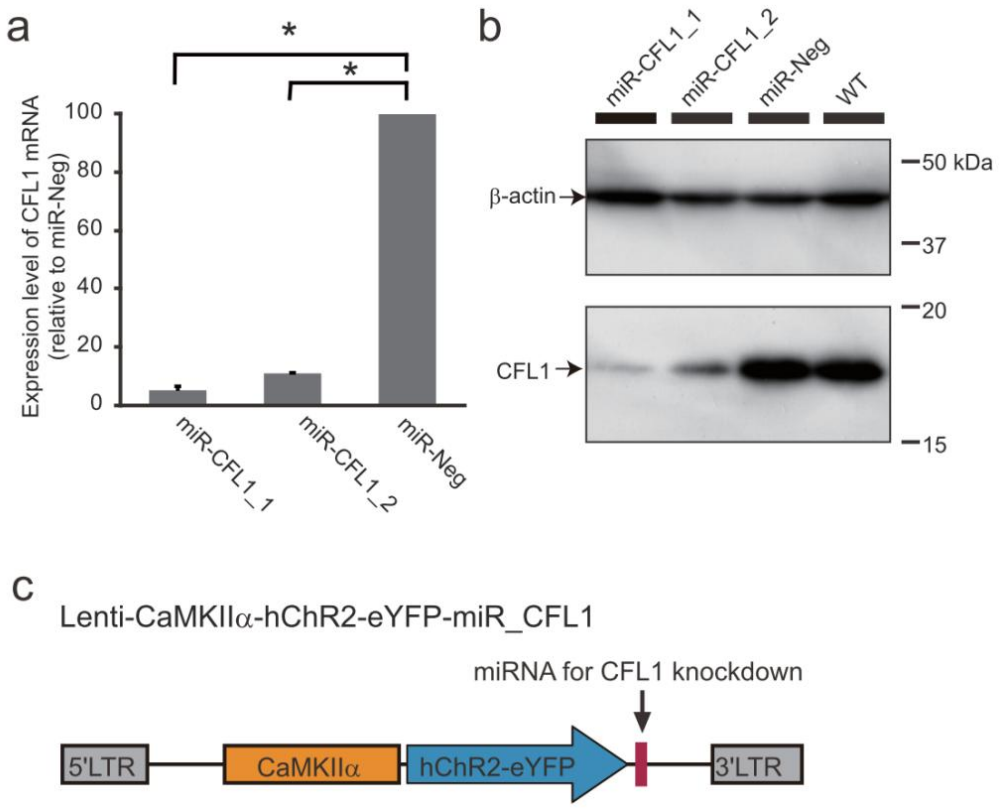

Figure 2. Lentiviral vector-mediated knockdown of CFL1 *in vitro*. (a) KD ability of two miRNAs each targeted to different sequence of CFL1 gene shown in CFL1-overexpressed HEK293T cells. CFL1 mRNA levels were normalized to that of the miR-Neg group. *$P < 0.01$, Student's *t*-test with Bonferroni correction. n = 3 for all groups. (b) KD of endogenous CFL1 protein with the two miRNAs shown in PC-12 cells. 'WT' indicates PC-12 cells that did not express any miRNA. (c) A schematic diagram of lentiviral vectors for co-expressing miRNA and fusion protein of ChR2-eYFP.

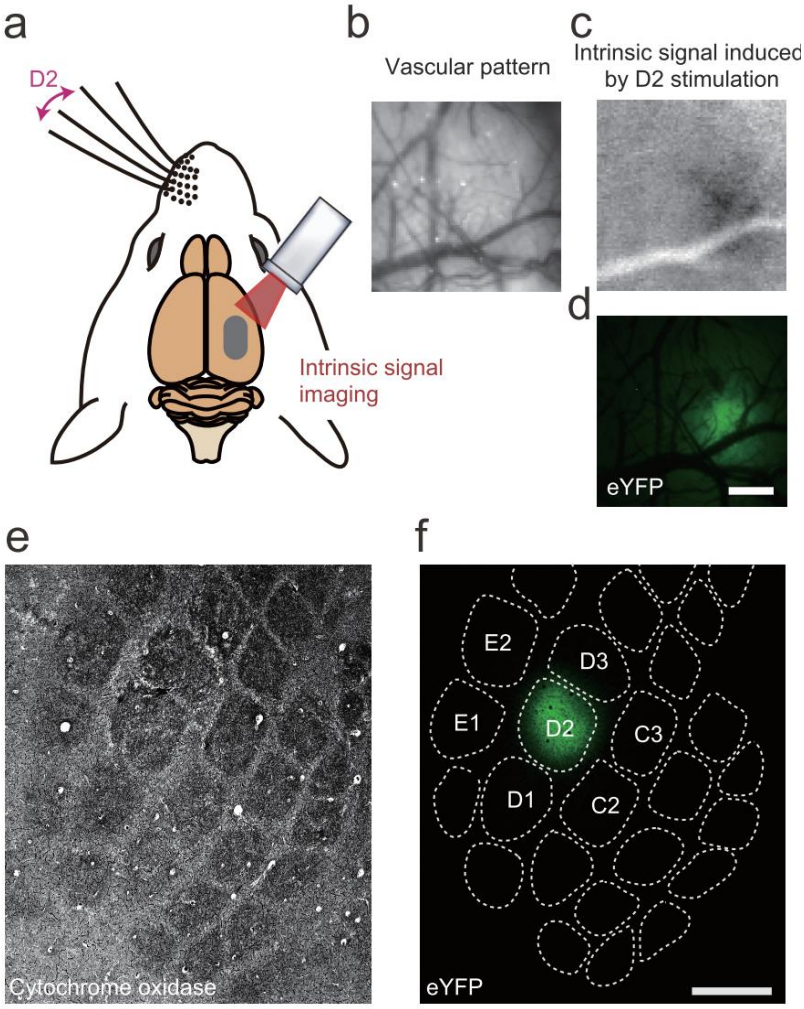

Figure 3. Intrinsic signal optical imaging-guided lentiviral targeting to D2 barrel column. (a) A schematic diagram of intrinsic signal optical imaging of the right barrel cortex while stimulating left D2 whisker. (b,c) A vascular pattern image (b) and intrinsic signal induced by D2 stimulation (c) of an example imaging session. (d) eYFP fluorescent image of the same cortical area of the same rat shown in b and c. Scale bar, 500 μm. (e,f) Tangential sections corresponding to L4 (e) and L2/3 (f) of a rat which was injected lentivirus to the D2 column. The L4 section was stained with cytochrome oxidase to visualize barrel patterns, which were projected onto L2/3 image based on vascular patterns. Scale bar, 500 μm.

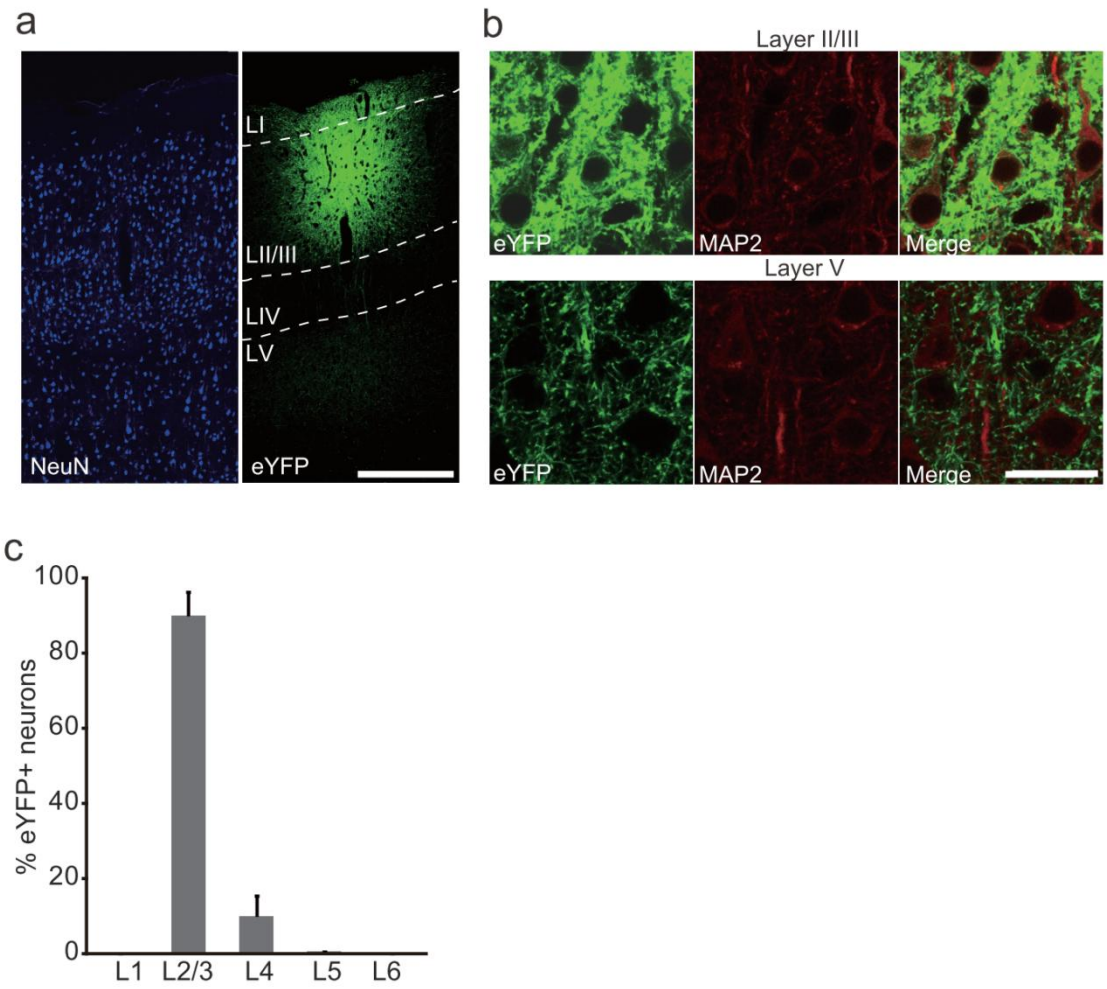

Figure 4. Lentiviral targeting to L2/3. (a) A NeuN-stained coronal section of a virus-injected rat. Scale bar, 300 μm. (b) Magnified images of L2/3 (top row) and L5 (bottom row) of a MAP2 stained coronal section. Scale bar, 20 μm. (c) Percentage of eYFP+ neurons in each cortical layers. n = 5 injection points.

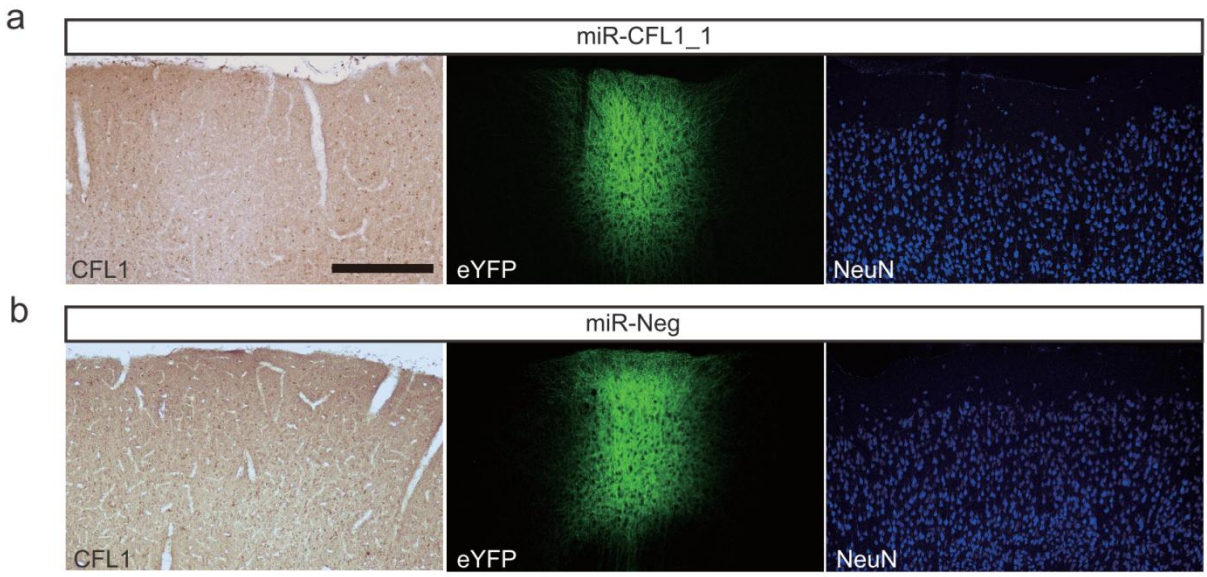

Figure 5. L2/3-restricted knockdown of CFL1 protein. (a) Two neighboring coronal sections each stained with CFL1 (left) or NeuN (right) obtained from a miR-CFL1_1 virus injected rat are shown. The eYFP fluorescence image (middle) was obtained from the NeuN-stained section. Scale bar, 300 μm. (b) Same as (a), but a section obtained from a miR-Neg virus injected rat.

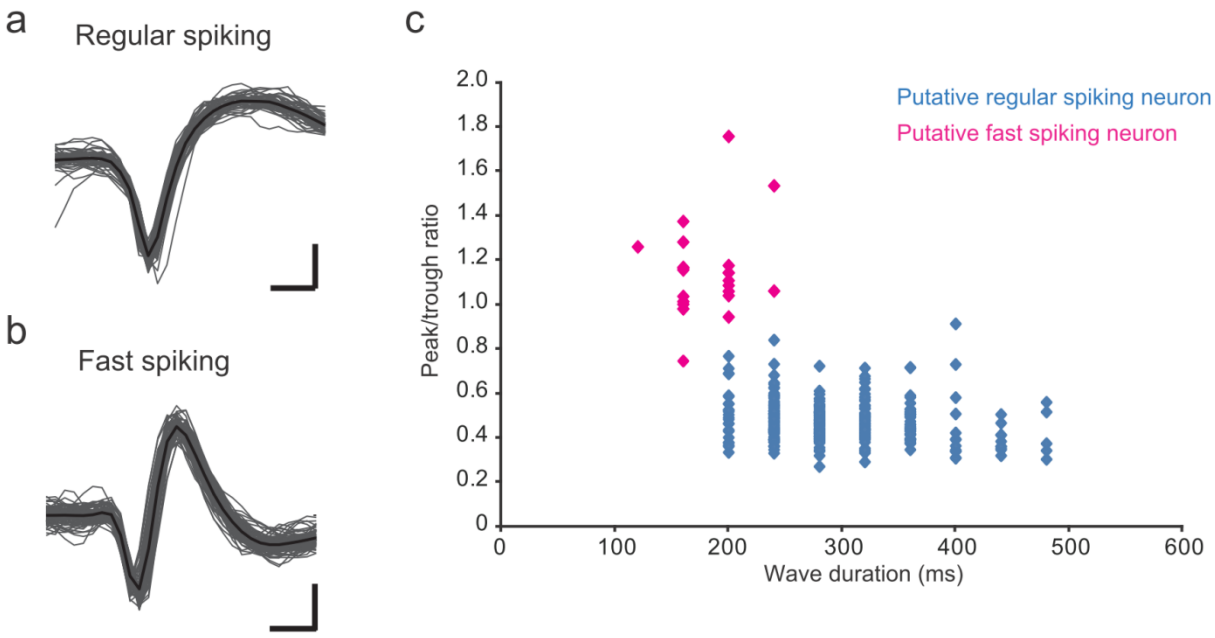

Figure 6. Cell classification based on spike waveforms. (a, b) Example waveforms of a regular spiking (a) and a fast spiking neuron (b). Gray lines indicate single spike waveforms, and black lines show averaged waveforms. Horizontal scale bar, 200 μs. Vertical scale bar, 150 μV. (c) Population data. Wave duration and peak/trough ratio of each neuron's waveform are plotted (n = 381). Neurons labeled with magenta were classified as fast spiking neurons.

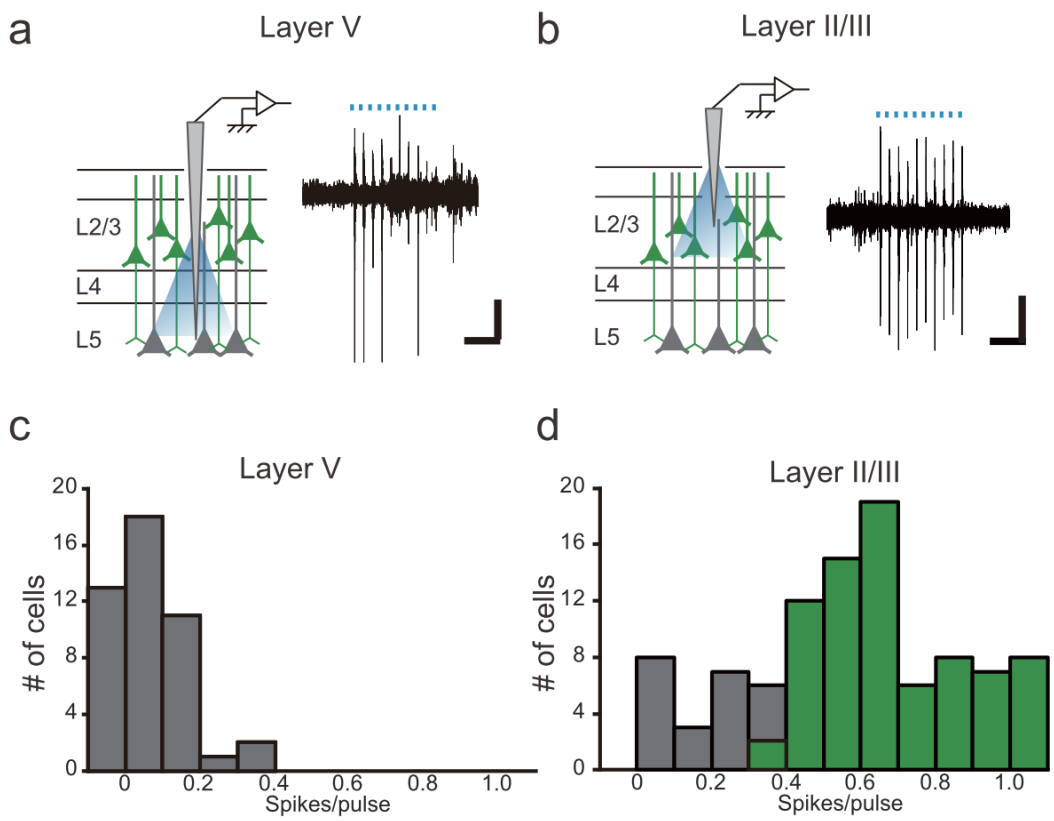

Figure 7. Reliability of light-evoked spikes at 20 Hz stimulation frequency. (a,b) Example response patterns of L5 (a) and L2/3 neuron (b) to 20Hz repetitive light stimulation. Scale bars: horizontal, 200 ms; vertical, 200 μV. (c, d) Distribution of spike probability in light-responsive neurons of L5 (c) and L2/3 neurons (d). Population labeled with green in (d) indicates neurons that were determined as putative ChR2+ and with gray as putative ChR2−.

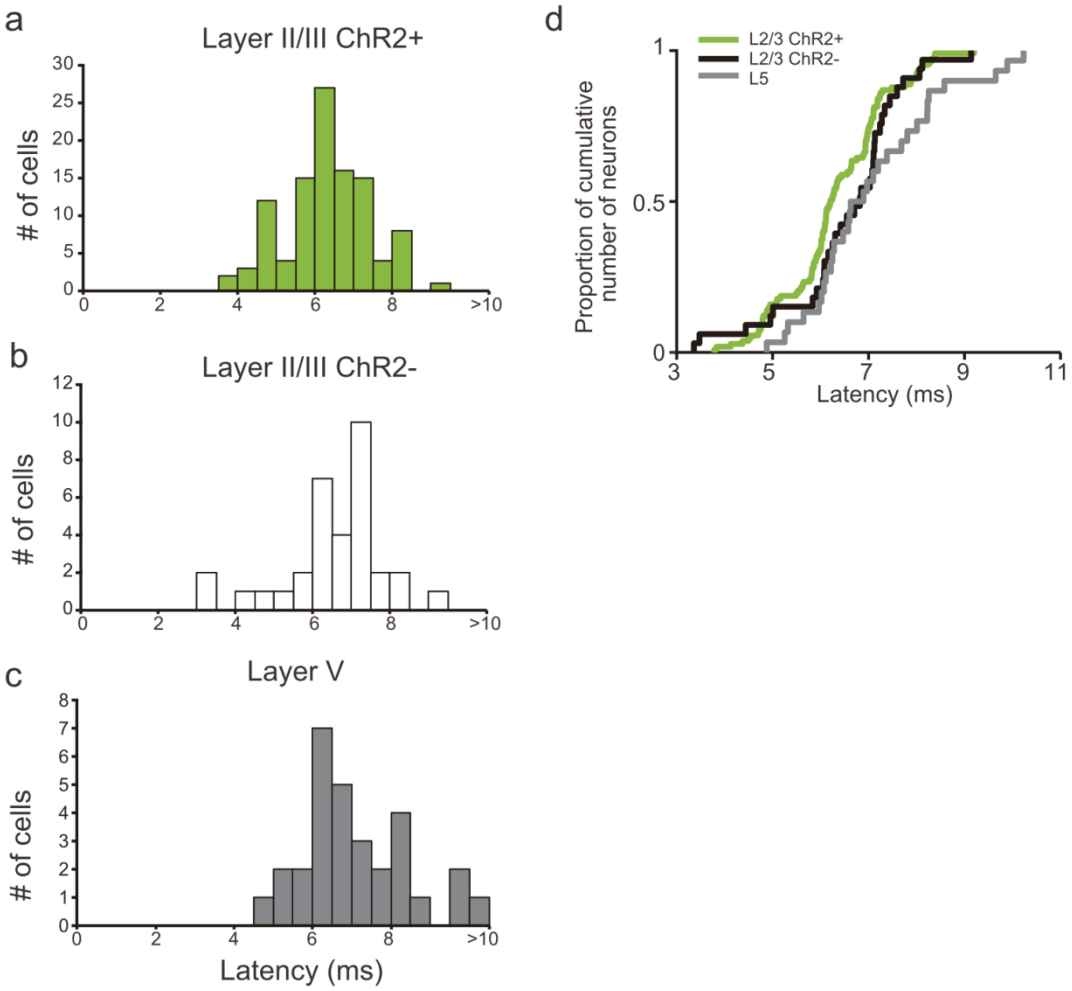

Figure 8. Latencies of light-evoked spikes. (a−c) Latency distribution of L2/3 putative ChR2+ (a) and ChR2− (b) neurons, and L5 light-responsive neurons (c). n = 107 (L2/3 ChR2+), 34 (L2/3 ChR2−) and 31 (L5 light-responsive). (d) Cumulative frequency histogram of latency for each group of neuron. None of the combination showed significant difference (L2/3 ChR2+ vs. L2/3 ChR2−, P = 0.22; L2/3 ChR2+ vs. L5 light-responsive, P = 0.11; L2/3 ChR2− vs. L5 light-responsive, P = 0.43; Kolmogorov-Smirnov test).

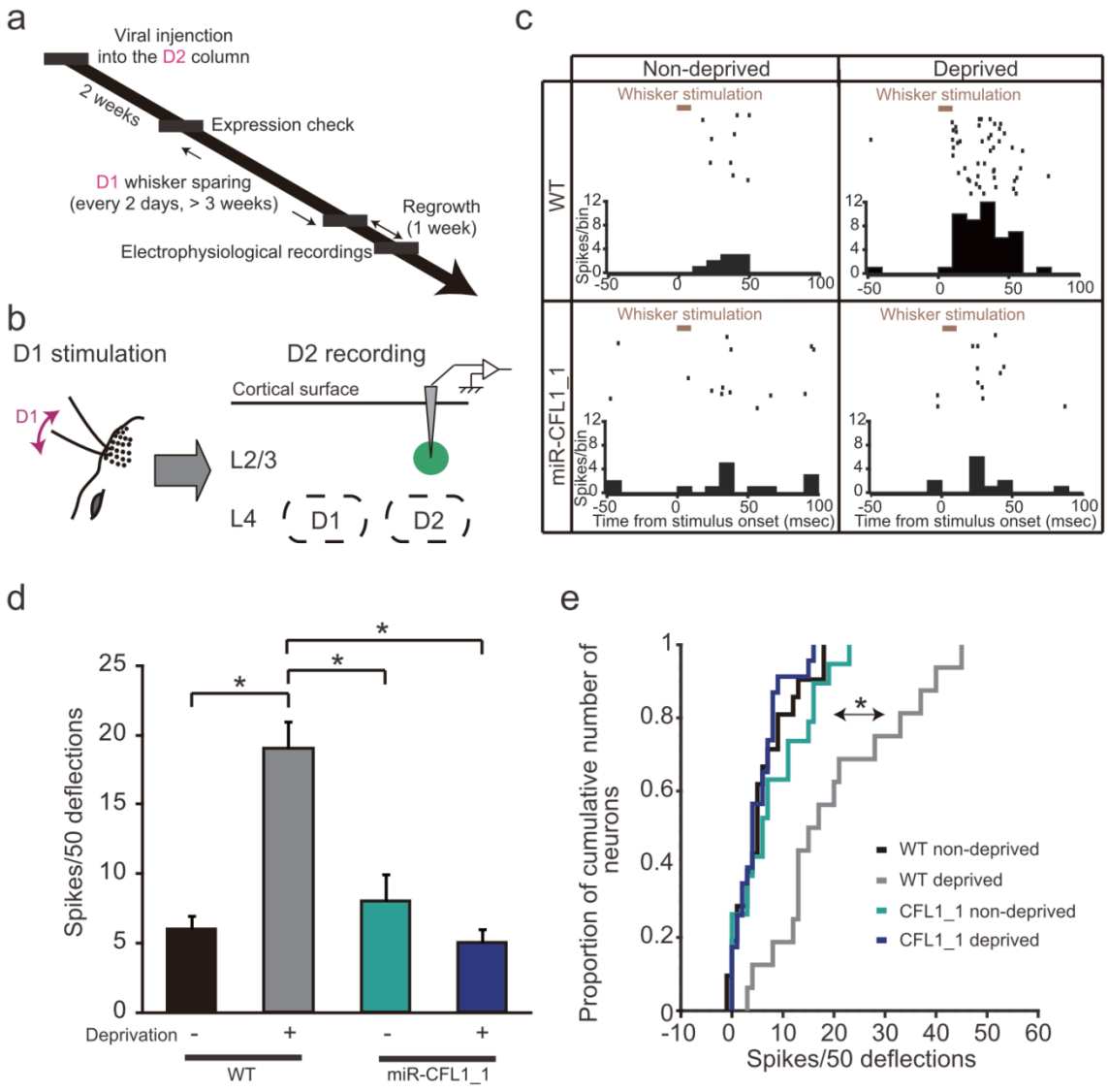

Figure 9. Effects of CFL1 KD on D2 neuronal responses to spared D1 inputs. (a) Experimental time course of virus injection, whisker sparing and electrophysiological recordings. (b) A schematic diagram of the experiment. Optogenetically-labeled CFL1 KD neurons in L2/3 of the D2 barrel column were recorded while D1 whisker was stimulated. (c) Example raster plots and peristimulus time histograms (PSTHs) of WT non-spared, WT spared, miR-CFL1_1 non-spared and miR-CFL1_1 spared rat. (d) Average number of spikes measured in response to D1 whisker stimulation in D2 column L2/3 neurons of each rat group. n = 21, 33, 20 and 23 units for WT non-spared, WT spared, CFL1_1 non-spared, CFL1_1 spared, respectively. *P < 0.01, Tukey-Kramer multiple comparison test. (e) Cumulative frequency histogram of spike number. *P < 0.01, Kolmogorov-Smirnov test with Bonferroni correction.

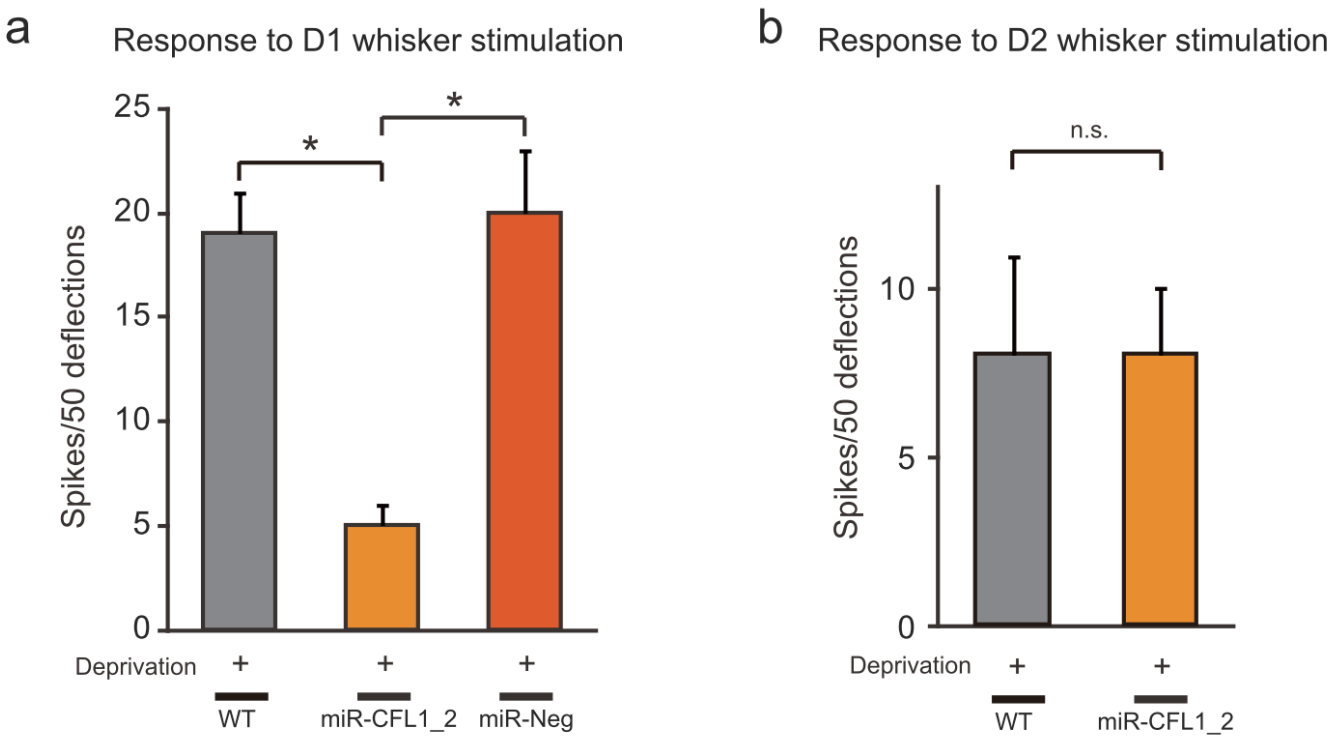

Figure 10. Effects of miR-CFL1_2 or miR-Neg expression on experience-dependent plasticity in D2 neuronal responses. (a) Average number of spikes measured in D2 neurons in response to D1 whisker stimulation for each rat group is shown (n = 33, 18, and 16 units for WT deprived, miR-CFL1_2 deprived, and miR-Neg deprived, respectively; *P < 0.01, Tukey-Kramer multiple comparison test). (b) Average number of spikes measured in D2 neurons in response to D2 whisker stimulation for each rat group (n = 33 and 18 units for WT deprived and miR-CFL1_2 deprived groups, respectively; P = 0.89, Student's t-test).

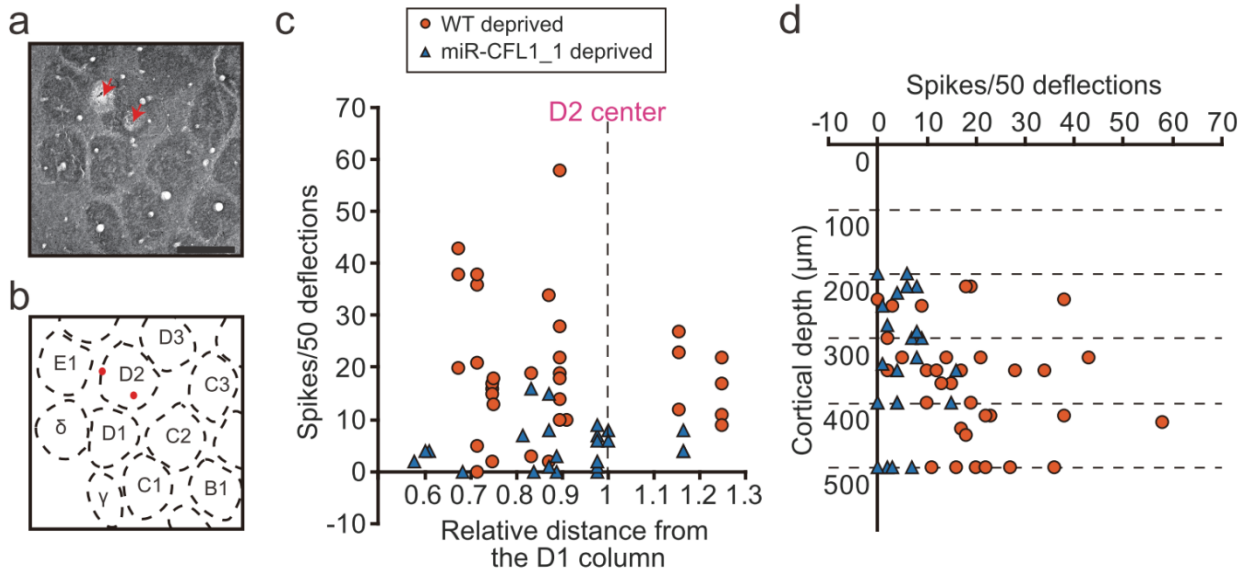

Figure 11. Relationship between response strength and recording location. (a) An example tangential section of cortical L4 in which two electrolytic lesions were made (indicated with red arrows). Scale bar, 500 μm. (b) An schematic drawing of the barrel pattern indicates both lesion marks were in the D2 barrel column. (c) Relationship between recording location and CFL1 KD effects. Recording locations in the D2 column were classified into 3 areas as shown in the left panel. Average number of spikes measured in each area of WT spared and miR-CFL1_1 spared rats are shown in the right panel. *P < 0.05, Student's t-test with Bonferroni correction. (d,e) Distribution of average spike number in response to D1 whisker stimulation vs. cortical depth of neurons recorded from WT spared rats (d) and miR-CFL1_1 spared rats (e).

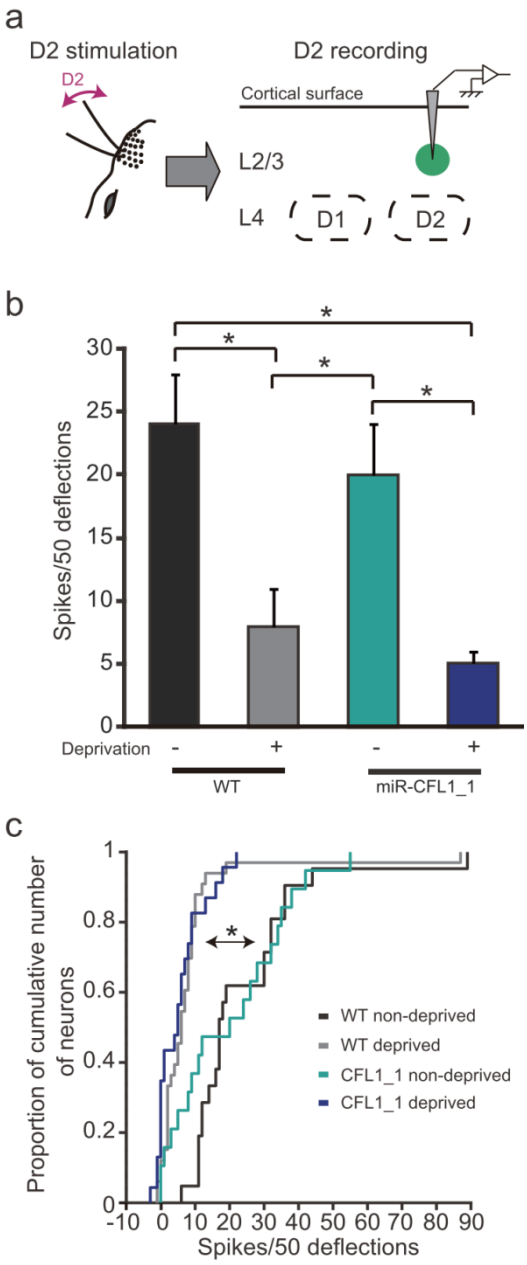

Figure 12. Effects of CFL1 KD on D2 neuronal responses to deprived D2 inputs. (a) A schematic diagram of the experiment. Optogenetically-labeled CFL1 KD neurons in L2/3 of the D2 barrel column were recorded while D2 whisker was stimulated. (b) Average number of spikes measured in response to D2 whisker stimulation in D2 column L2/3 neurons of each rat group. *P < 0.01, Tukey-Kramer multiple comparison. n = 21, 33, 20 and 23 units for WT non-spared, WT spared, CFL1_1 non-spared, CFL1_1 spared, respectively. (c) Cumulative frequency histogram of spike number. *P < 0.01, Kolmogorov-Smirnov test with Bonferroni correction.

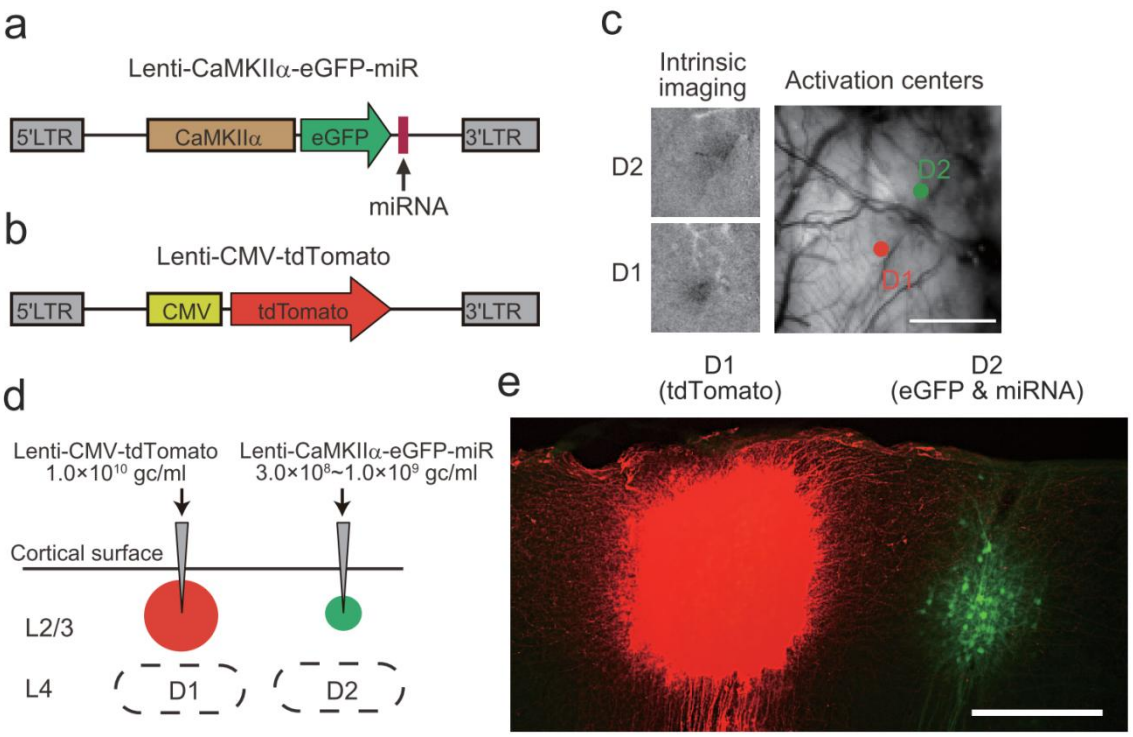

Figure 13. Virus injection for morphology experiments. (a,b) Schematic diagrams of lentiviral vectors for co-expressing eGFP and miRNA under the control of CaMKIIα promoter (a) and for expressing tdTomato under the control of CMV promoter (b). (c) Viruses were injected into center of each barrel column identified with intrinsic signal optical imaging. Scale bar, 500 μm. (d) Virus injection was targeted to L2/3 of each column. (e) A representative parasagittal section which expresses tdTomato (D1 column) and eGFP (D2 column). Scale bar, 300 μm.

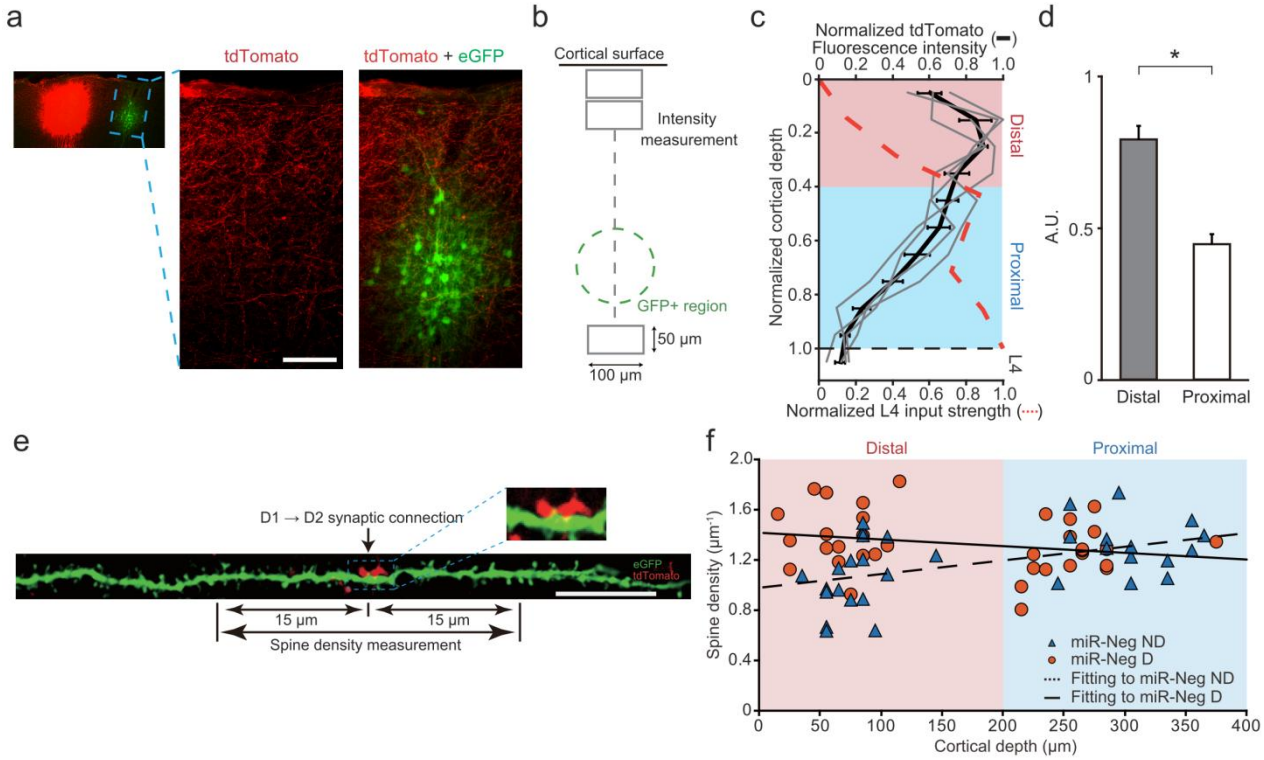

Figure 14. Effects of sensory deprivation on spine density. (a) Magnified view of GFP expressing region in the parasagittal section shown in Fig. 13e. Scale bar, 100 µm. (b) TdTomato fluorescence intensity derived from D1 axons was measured in a rectangle ROI. The rectangle was vertically scanned within the D2 column. (c) An averaged vertical profile of normalized tdTomato fluorescence intensity (black line). Gray lines indicate data of each rat (n = 4 rats). See Materials and Methods for details about normalization of fluorescence intensity and cortical depth. A vertical profile of L4 input strength measured in [70] was also plotted on the same graph (orange dashed line). (d) TdTomato fluorescence intensity averaged in either the distal or proximal part of the supragranular layer. *P < 0.05, paired t-test. (e) A representative dendritic branch which made a synaptic connection with a tdTomato+ D1 axonal bouton. Magnified view of the synaptic connection is shown in the inset. Scale bar, 10 µm. (f) Dendritic spine densities of dendritic branches that receive D1 inputs in the miR-Neg non-deprived (ND) and deprived (D) groups were plotted against cortical depth of measured dendrites. Each dot represents a dendritic branch segment. Dashed and solid lines correspond to lines fitted to distribution of miR-Neg ND and D groups, respectively, by linear regression. *P < 0.005, $F_{1,63}$ = 9.33, F-test (the null hypothesis stated that slopes of fitted lines by linear regression were equal).

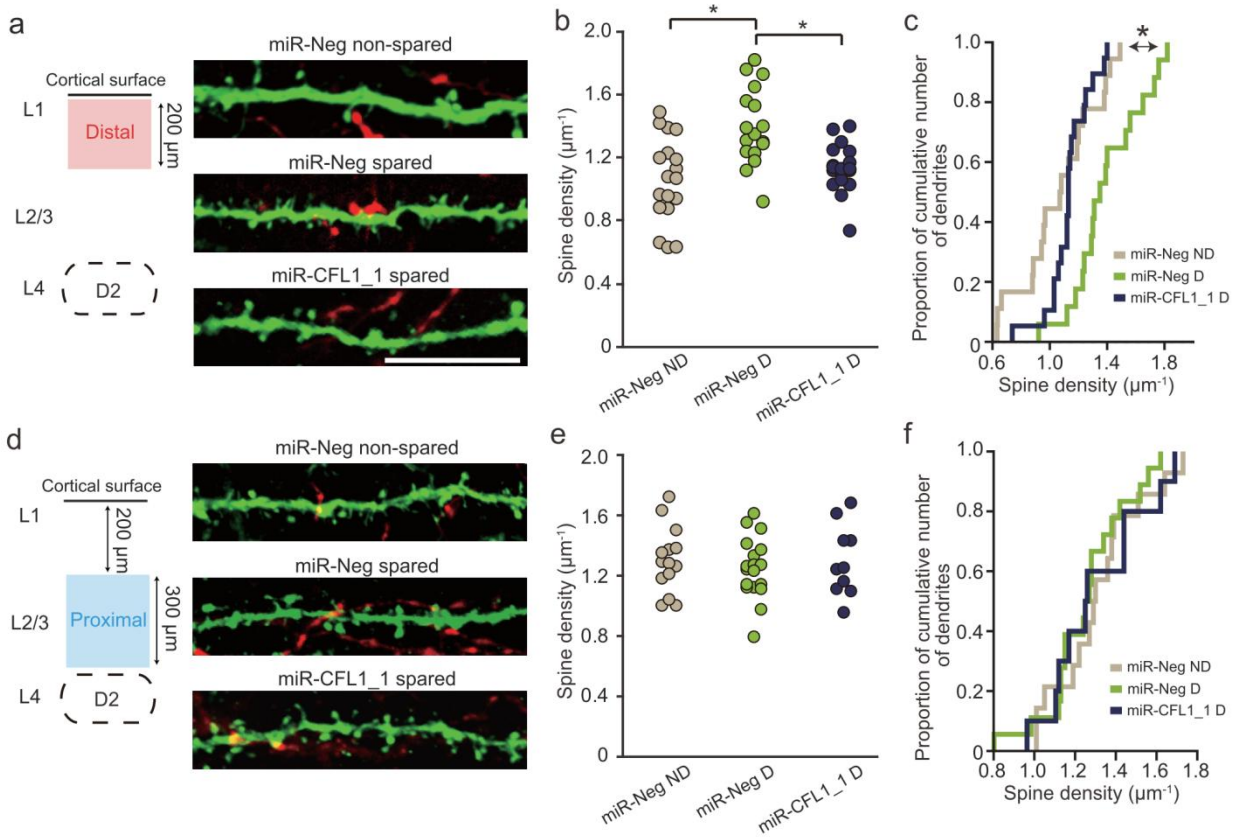

Figure 15. Effects of CFL1 KD on spine density during sensory deprivation. (a) Representative images of dendritic branches within the distal part of L2/3. Scale bar, 10 µm. (b) Spine densities measured in the distal part. **P* < 0.005, ***P* < 0.001, Student's *t*-test with Bonferroni correction. n = 18, 17 and 19 branch segments for miR-Neg non-deprived (ND), miR-Neg deprived (D) and miR-CFL1_1 deprived, respectively. (c) Cumulative frequency histogram of spine density. **P* < 0.05 (miR-Neg ND versus miR-Neg D and miR-Neg D versus miR-CFL1_1 D), Kolmogorov-Smirnov test with Bonferroni correction. (d−f) Same as a-c but of dendritic branches measured within the proximal part of L2/3. n = 14, 18 and 10 branch segments for miR-Neg ND, miR-Neg D and miR-CFL1_1 D, respectively.

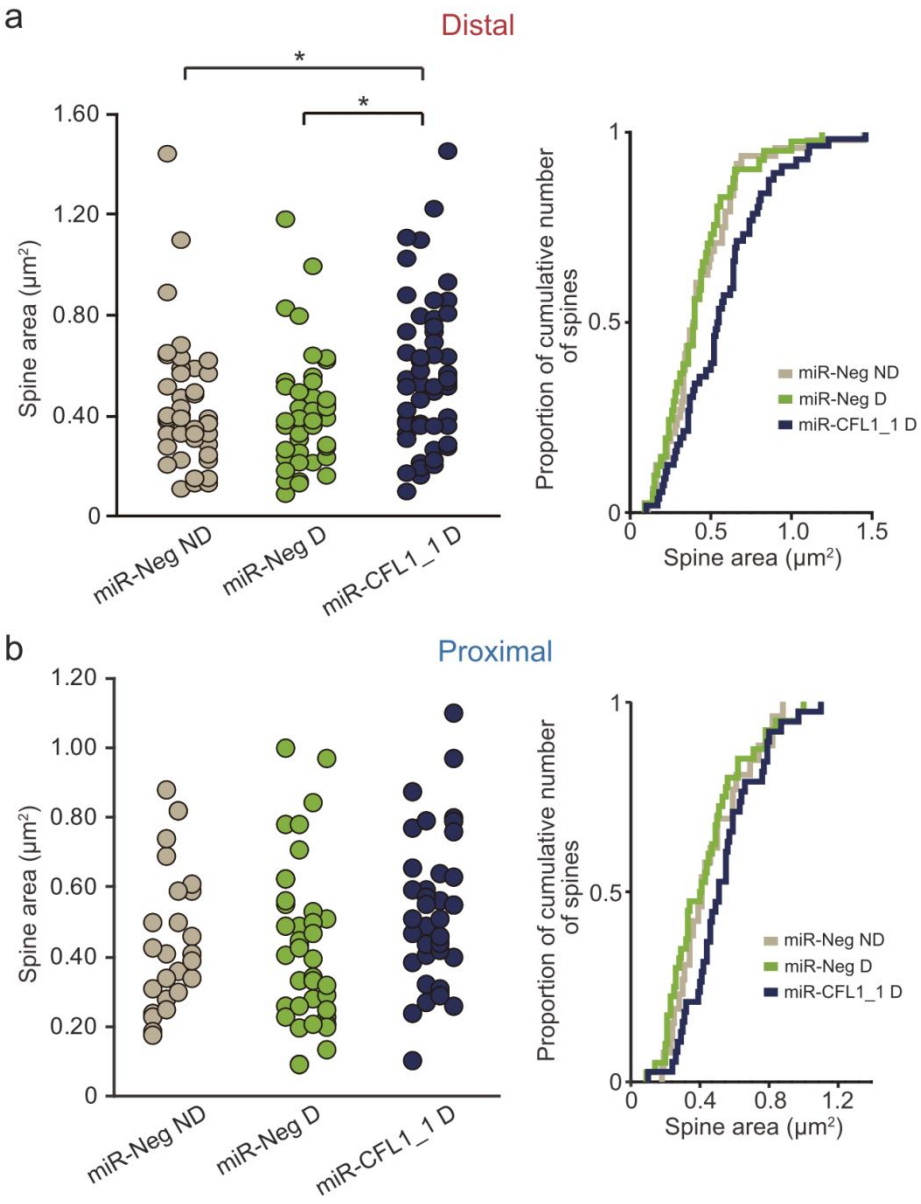

Figure 16. Spine area analysis. (a) Plots of spine area measured in distal part of L2/3 in each rat group (left) and cumulative frequency histogram (right). *P < 0.05, Student's *t*-test with Bonferroni correction. n = 48, 41 and 56 spines for miR-Neg ND, miR-Neg D and miR-CFL1_1 D, respectively. (b) Same as (a) but of spine area measured in the proximal part. n = 26, 40 and 38 spines for miR-Neg ND, miR-Neg D and miR-CFL1_1 D, respectively.

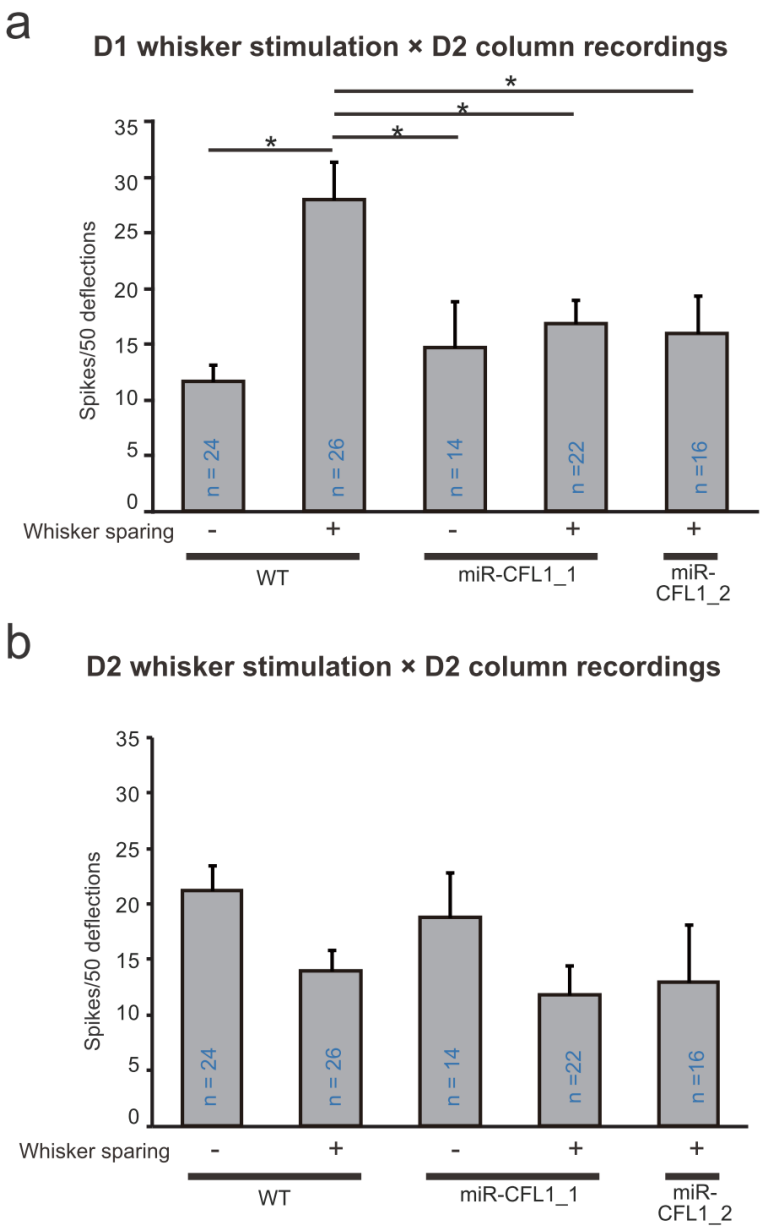

Figure 17. Effects of CFL1 KD in L2/3 neurons on L5 neuronal responses. (a, b) Average number of spikes measured in response to D1 (a) and D2 (b) whisker stimulation in D2 column L5 neurons of each rat group. Data of each L5 neuron was included regardless of whether or not it was classified as light-responsive. *$P < 0.05$, Tukey-Kramer multiple comparison test.

3.3 Discussion

In the present study, CFL1 was locally knocked down in L2/3 excitatory neurons of a deprived column (the D2 column) by using a lentiviral vector-based RNAi approach. In rats injected with miR-CFL1-expressing vectors, the experience-dependent expansion of spared input representation was prevented in CFL1 KD neurons, while the shrinkage of deprived input representation was preserved. Furthermore, the spine density around dendritic spines receiving transcolumnar axonal projections from the spared D1 column was increased in L2/3 neurons of the deprived D2 column, and this occurrence was impaired by CFL1 KD. These results provide, to the best of my knowledge, the first direct evidence that the CFL1-mediated actin dynamics is necessary for plasticity in horizontal transcolumnar circuits during adult cortical EDP.

For *in vivo* RNAi experiments, I selected lentiviral vectors because they diffuse to a lesser extent *in vivo* than other available vectors, such as adeno-associated viral vectors [7]. Although L2/3 of the D2 column contains axons emanating from other layers and columns, as well as apical dendrites extending from deeper-layer neurons and not just the cell bodies of L2/3 neurons, viral expression was successfully confined to the L2/3 neurons of the D2 column (Fig. 4). This observation suggests that my lentiviral vectors mainly infected neurons through their cell bodies. The rodent barrel cortex has clear

anatomically-separable column patterns in L4, which correspond to whisker patterns in the face, where each whisker activates a slightly larger but corresponding barrel column [8]. Previous studies reported that within-column L4 to L2/3 connections showed a different direction of plasticity changes in their synaptic efficacies between spared and deprived columns [5,9]. This observation suggests that different molecular machineries are exerted, or that the same sets of molecules are differentially regulated between spared and deprived columns during EDP. To investigate the roles of CFL1 KD in D2 (deprived) column neurons, therefore, the effects of gene manipulation should be restricted to the D2 column, so that CFL1 expression in the D1 column neurons remains intact. Similarly, layer-specific gene manipulation is also essential to conclusively demonstrate gene functions in the neurons of a specific cortical layer. Indeed, L2/3-specific CFL1 KD also affected the potentiation of spared whisker responses in L5 neurons (Fig. 17). If gene manipulation was not restricted to L2/3, the results will be confounding, because L2/3 neurons also receive extensive inputs from L4 and L5 neurons of the same column [8]. The present study achieved both column- and layer-restriction of gene manipulation, and demonstrated that synaptic locus of plastic changes that was affected by CFL1 KD could be clearly defined as L2/3 pyramidal neurons in D2 barrel column.

I used ChR2 as a light-responsive tag for the effective identification of CFL1 KD neurons. The major technical problem regarding ChR2 as a tag is the difficulty in discrimination of ChR2+ and light-responsive ChR2– neurons [52,56,58,59]. Accordingly, I identified ChR2+ neurons in L2/3 by taking advantage of the properties of ChR2– light-responsive neurons in L5. The properties of these neurons could be estimated precisely, because ChR2+ neurons were rarely found in L5 (Fig. 4b,c). Light-responsive neurons in L5 showed low reliability to high frequency stimulation at 20 Hz (Fig. 7c), which is in agreement with the work of others concerning ChR2– light-responsive neurons [52,56,58,59], raising confidence in the validity of the reliability criteria derived from the L5 cells.

The current investigation employed the mouse CaMKIIα promoter (1.3 kb) to drive the expression of miRNA. This promoter drives transgene expression in an excitatory neuron-specific manner when it is loaded onto lentiviral vectors [62]. To efficiently record CFL1 KD neurons in extracellular recording, I thus targeted regular-spiking neurons and excluded fast-spiking neurons (Fig. 6) most of which correspond to parvalbumin-positive GABAergic interneurons [74].

I showed that the effect of KD was consistent between the two miR-CFL1s with different target sequences within *CFL1* gene (Figs. 9 and 10a). Because miRNAs can

downregulate genes bearing sequences complementary to their seed sequences (positions ~ 2–7 of the guide strand) [75], evidence of the same outcome with different RNAi sequences reduces concerns about the target specificity of RNAi experiments [69]. The results presented here therefore suggest that the effects observed in the CFL1 KD rats were not due to off-target actions of the miRNAs.

The technique for simultaneous labeling of the D1 and D2 column (Fig. 13) allowed the demonstration of CFL1-dependent changes in dendritic spine density that could not heretofore be accomplished (Fig. 15a-c). The current results are consistent with those from previous studies, in that sensory deprivation promotes the formation of stable dendritic spines in a deprived column located adjacent to a spared column [10,76], and also increases the density of horizontal projections from a spared column to the adjacent deprived columns [77]. In contrast, the absence of dendritic spine structural plasticity in the proximal portion of the D2 column supragranular layer (Figs. 15d-f and 16b) is consistent with the idea that CFL1-mediated actin dynamics do not involve a decrease in deprived input representation, because intracolumnar deprived inputs from L4 are thought to prevail in the proximal portion (Fig. 14c) [70,78]. The present results, together with the earlier data, may suggest that dendritic spines receiving horizontal transcolumnar inputs from the spared column are selectively generated in deprived

column neurons during sensory deprivation.

I showed that CFL1 KD impaired the neuronal response increase to spared inputs but did not affect the response decrease to deprived inputs (Figs. 9 and 12). This phenotype is similar with that observed in mice in which autophosphorylation of CaMKIIα was blocked [79]. As well as CaMKIIα [80], ADF/cofilin is necessary for hippocampal long-term potentiation [15,18,19]. However, a direct link between CFL1 and CaMKIIα has never been reported. Nonetheless, because calcium signaling regulates the activity of ADF/cofilin [17,81], it may be possible that CaMKIIα influences barrel map plasticity by regulating the CFL1 activity. Interestingly, CFL1 is also under the control of calcineurin, a regulator of long-term depression (LTD) [82], and is necessary for the dendritic spine shrinkage associated with hippocampal LTD [83]. Given that the LTD contributes to the response decrease to deprived inputs in the barrel cortex [84,85], it is expected that CFL1 also participates in this process. In hippocampal neurons, however, it is also known that spine shrinkage and the decrease in synaptic transmission efficacy during LTD are dissociated processes at the level of molecular pathways [83]. The present data, together with these previous observations, suggest that the functional depression of deprived input representation is likewise dissociated from the CFL1-dependent structural changes in the dendritic spines in the

rat barrel cortex.

The activity of CFL1 is reversibly regulated by dephosphorylation (activation) and phosphorylation (inactivation) at the serine-3 residue [81]. Phosphorylation of CFL1 is performed by LIM-kinase 1 [86], one of the genes missing in individuals with Williams syndrome [87]. Patients with Williams syndrome exhibit various forms of mental retardation including learning and intellectual disabilities [88]. It is therefore possible that the impaired plasticity in horizontal transcolumnar connections caused by CFL1 inactivation contributes to Williams syndrome.

In conclusion, I demonstrate here that CFL1-mediated actin dynamics function in a horizontal connection-specific manner during EDP induced by the single whisker experience protocol. In addition to the rodent vibrissal system, the primate brain is characterized by a highly sophisticated neocortical columnar organization [89]. Cortical circuit reorganization across functional columns through horizontal connections is necessary for functional cortical recovery after peripheral deficits, such as focal retinal lesions [90]. Moreover, plasticity in horizontal transcolumnar or interareal connections is also critical for learning [91,92]; thus CFL1-mediated circuit reorganization may possibly be a general mechanism for the flexible nature of the human brain. However, this proposal will require further study.

4. Cell-type specific optogenetic investigation of a cerebellar cardiovascular module situated within the uvula

4.1 Materials and Methods

4.1.1 Plasmid construction

The shortened L7 (sL7) promoter, comprising a 1 kb sequence upstream of the first ATG within exon 2 of L7 gene, was cloned by PCR from the template plasmid, pL7-tWGA (kindly provided by Dr. Y. Yoshihara, RIKEN Brain Science Institute, Wako, Japan). A half nanogram of plasmid template was amplified in a 25 μl reaction mixture containing 0.2 μM of each primer, 200 μM of each dNTP, 1 × PrimeSTAR buffer and 0.625 U PrimeSTAR HS DNA polymerase (Takara Shuzo, Co., Ltd., Shiga, Japan). The primer combinations were as follows: sense 5'-GTT CCA CCC TCA TGT TGG TTG-3' and antisense 5'-CGA TCG CCC TGC ACG TG-3'. PCR was performed at 98ºC for 5 min and then for 35 cycles at 98ºC for 10 sec, 60ºC for 5 sec and 72ºC for 1 min in a Program Temp Control System PC-800 (ASTEC, Fukuoka, Japan). The PCR product was electrophoresed on agarose gel (1% w/v), extracted using QIAquick Gel Extraction Kit (QIAGEN, Hilden, Germany), subcloned into pGEM-T Easy Vector (Promega, Madison, WI, USA) and sequenced.

4.1.2 Lentiviral preparation and injection

I produced two lentiviral vectors, Lenti-sL7-hChR2-EYFP-WPRE (sL7-ChR2) and Lenti-sL7-eNpHR-EYFP-WPRE (sL7-eNpHR), in this section (Fig. 18). Eight- to twelve-week-old male Wistar rats were used for lentiviral or PBS injection. Each rat was anesthetized with ketamine/xylazine (90 mg/kg and 10 mg/kg, respectively), and positioned in the stereotaxic apparatus. A midline sagittal incision was made, and the skull over the cerebellum was exposed. For targeting of vector solution to lobule IXab or VIII, a small hole was drilled 14.0 mm posterior to bregma and on the midline. A glass pipette (~50 μm tip diameter) was attached to a 32-gauge blunt end needle, and the needle was then attached to a 10 μl gas-tight Hamilton syringe (Hamilton Company). The glass pipette was tilted 20° forward in the sagittal plane, and lowered into the cerebellum to a depth of 4.1 mm (for IXab targeting) or 2.85 mm (for VIII targeting) from the dura mater [93]. Then virus solution (6 μl), at a titer of > 10^{10} genome copies/ml, was injected at a flow rate of 200 nl/min using the micropump and microprocessor-based controller. The needle was left in place for an additional 10 min before being retracted from the brain. The scalp incision was sutured, and the rat was returned to a standard cage after recovering from the anesthesia.. Rats injected with a lentiviral vector into lobule IXab (sL7-ChR2 rats, n = 8; sL7-eNpHR rats, n = 11) were used for immunohistochemical, electrophysiological and blood pressure experiments.

Rats injected with a lentiviral vector into lobule VI (sL7-ChR2 rats, n = 2; sL7-eNpHR rats, n = 5) or lobule VIII (sL7-ChR2 rats, n = 4; sL7-eNpHR rats, n = 3) were used only for electrophysiological or blood pressure experiments, respectively. Rats injected with PBS into lobule IXab (n = 3) were also used for blood pressure experiments. Animals were maintained for more than 8 days before use in physiological experiments.

4.1.3 Immunohistochemistry and cell counting

Sections (25 μm thick) were blocked with 5% normal goat serum (WAKO) and incubated for 24 h at 4 ºC with one of the following antibodies: mouse anti-parvalbumin monoclonal antibody (1:4000, Sigma-Aldrich), mouse anti-calbindin-D28k monoclonal antibody (1:3000, Sigma-Aldrich), mouse anti-NeuN monoclonal antibody, or mouse anti-mGluR2 monoclonal antibody (1:500, kind gift from Dr. R. Shigemoto, National Institute for Physiological Sciences, Japan) [94]. Then the sections were incubated for 3 h at room temperature with AlexaFluore647-conjugated goat anti-rabbit antibody (1:500, Invitrogen). For staining of the representative sagittal and horizontal sections shown in Fig. 23, rabbit anti-GFP polyclonal antibody (1:5000, Medical & Biological Laboratories, Aichi, Japan) was used to enhance EYFP signals. These sections were then incubated for 3 h at room temperature with AlexaFluore488-conjugated goat

anti-rat IgG antibody (1:500, Invitrogen), and counterstained with Hoechst. The stained images were obtained using a fluorescence microscope (BZ-9000, Keyence).

For counting of particular cell type, three sagittal sections (separated from each other by 100 μm) around the center of the injection site were used for each rat. To calculate the percentage of each cell type among all EYFP-positive cells, I used sections stained with anti-parvalbumin antibody. I counted all EYFP-positive cells in each section, and then counted EYFP-positive stellate/basket cells and PCs. Stellate/basket cells and PCs were discriminated by their morphology and the locations of cell bodies in the cerebellar cortex. EYFP-positive cells considered to be neither stellate/basket cells nor PCs were designated 'other'. Then the numbers counted were summed across three sections and percentages were calculated by dividing the number of EYFP-positive cells of each type by that of all EYFP-positive cells. To measure the transduction efficiencies into each cell type, EYFP-positive cells were counted and scored for co-labeling with each cell type marker, calbindin-D28k (PC), parvalbumin (stellate/basket cell), NeuN (granule cell) or mGluR2 (Golgi cell). Cell counting for calculation of transduction efficiencies was performed within the surface area (0-500 μm depth from cortical surface) of lobule IXab in each section.

4.1.4 Electrophysiological recording and optical stimulation

Each rat injected with a lentiviral vector into cerebellar lobule VI, or IXab was anesthetized with ethyl carbamate (1.2 g/kg) and then positioned in a stereotaxic apparatus. The skull around the virus-infected area of each rat was exposed and carefully removed by a drill. The activity of single neurons was recorded extracellularly from the infected area using a glass-coated tungsten microelectrode (resistance < 0.6 MΩ). The microelectrode was advanced through the intact dura mater into the cortex using the hydraulic micromanipulator. Neural signals were amplified using the amplifier and band-pass filtered (0.05-5 kHz), and then digitized at 25 kHz and stored using the Recorder Software. Stored data were analyzed offline with the 'Off-line Sorter' program (Plexon) for sorting into single-unit data by waveform analysis. Single-unit data were then analyzed with MATLAB. A neural signal was considered to originate from a PC if it exhibited two types of spiking activity: simple spikes (SSs) characterized by a single depolarization occurring between 20 and 200 Hz and complex spikes (CSs) characterized by an initial fast depolarization followed by smaller and relatively constant spikelets [95]. Simple and complex spikes were judged to have originated from the same PC when a transient pause (~20 ms) in SS firing followed each CS.

The blue light source was a diode pumped solid state (DPSS) laser (peak wavelength at 473 nm, 200 mW; beam diameter, 2.0 mm; CNI Optoelectronics,

Changchun, China). The outgoing beam was passed through an ND filter (Thorlabs) to calibrate the output power and then an electrically controlled mechanical shutter (hole diameter, 2.0 mm; Model LS3, UNIBLITZ) to control the length of each light pulse. The mechanical shutter was controlled by an electronic stimulator (NIHON KOHDEN). The beam was next entered into an optic fiber (core diameter, 62.5 μm) through a fiber collimator. The laser, ND filter, shutter and collimator were mounted on an optics breadboard. The output beam from the optic fiber was also passed through another fiber collimator (focal length, 4.50 mm; beam waist diameter of output beam, 0.9 mm). The power of the output beam was measured with a power meter (PM100D, Thorlabs). The optic fiber was held in a micromanipulator to control the position of the beam spot on the surface of the cerebellum. The orange light source was another DPSS laser (peak wavelength at 593 nm, 200 mW; beam diameter, 3.0 mm; CNI Optoelectronics). The outgoing beam was passed through an ND filter. Then the beam was passed through two lenses (focal length: 1^{st} lens 60 mm, 2^{nd} lens 30 mm) to thin the beam diameter from 3.0 to 2.0 mm. The beam was next entered into an optic fiber through a fiber collimator. The output beam from fiber collimator was also passed through another collimator (focal length, 4.50 mm; beam waist diameter, 0.9 mm). The tip of fiber and cerebellar surface was separated at approximately 8 cm. The divergent angle of the output beam was

0.045°. Therefore the beam spot diameter on the cerebellar surface was calculated as approximately 1.0 mm. Light intensity was set at ~50 mW/mm^2 in all electrophysiological experiments [96]. To effectively illuminate the medial part of lobule IXb where electrical stimulation evokes the strongest cardiovascular responses in anesthetized rabbits [41], a tungsten microelectrode was positioned at lobule IXb (coordinates from the bregma: AP, 15.2 mm; ML, 0.0 mm; DV, 6.0 mm) and used to record PC activity. The position of light illumination was then adjusted so as to maximize the effect of light illumination on that cell.

The effect of optical stimulation on each PC's firing rate was heard on a sound monitor. It was therefore possible to roughly determine the effective site of stimulation for each cell by ear. To characterize the responses of PCs to blue or orange light in sL7-ChR2 or sL7-eNpHR rat cerebellum, I used a light pulse of 100 ms duration with the interstimulus interval set at 500 ms. I performed 100 trials for each cell. Light-responsive PCs were classified by performing a paired *t*-test between the SS firing rate during the 50 ms period before light onset and that during the 50 ms period after latency across all trials for that cell, and thresholded at the $P < 0.05$ significance level [97]. To determine the latency between light onset and neural response, a 6 ms-long sliding window was swept through the electrophysiology data to search for the

earliest 6 ms period that deviated from baseline SS firing rate (which was calculated from the SS firing rate during the 6 ms period before light onset), as assessed by paired *t*-test between the SS firing rate during each window and that during the baseline period, across all trials for each cell. An SS firing rate modulation index (MI) was calculated using following equation: (firing rate during the 50 ms period before light onset)/(firing rate during the 50 ms period after latency).

4.1.5 Arterial blood pressure measurement

Each rat injected with a lentiviral vector into lobule IXab or VIII was anesthetized with ethyl carbamate (1.2 g/kg). Body temperature was maintained at 37.5ºC using a homeothermic heating pad (BioResearch Center, Aichi, Japan). A catheter (inner diameter, 0.5 mm; outer diameter, 0.9 mm, Natsume Seisakusho) was inserted into the left femoral artery and connected to a blood pressure transducer (DX-360, NIHON KOHDEN) to measure BP continuously [98]. BP signals were amplified using a blood pressure amplifier (AP-641G, NIHON KOHDEN), digitized at 1 kHz and analyzed offline. Mean arterial pressure (MAP) was calculated as diastolic pressure plus one third of the pulse pressure for each beat. To calculate normalized MAP (nMAP) in each trial, average MAP during 0-5 sec before light onset was used.

For light illumination onto lobule IXab or VIII, the skull around the lobule IX or

VIII of each rat was exposed and carefully removed. Then a tungsten microelectrode was positioned at lobule IXb (AP, 15.4 mm; ML, 0.0 mm; DV, 6.0 mm from bregma) or lobule VIII (AP, 15.4 mm; ML, 0.0 mm; DV, 3.6 mm from bregma) and used to record PC activity. The position of light illumination was then adjusted so as to maximize the effect of light illumination on that cell.

To investigate the effects of ChR2-mediated photostimulation on resting BP, blue light was illuminated for 5 sec at 50 Hz (10 ms light/10 ms interval) in each trial. Blue light intensity was ~50 mW/mm^2. The intertrial interval was at least 1 min. I performed at least 20 trials per each rat.

To investigate the effects of eNpHR-mediated photoinhibition on BP at rest or during postural alteration, orange light was illuminated for 10 sec continuously in each trial. Orange light intensity was ~50 mW/mm^2. The intertrial interval was at least 1 min. I performed at least 30 trials per each rat.

For electrical stimulation experiments, I used 4 male Wister rats (10 weeks old). Each rat was anesthetized, and received surgery in the same way with lentivirus-injected rats. Electrical stimulation of lobule IXb was via a Platinum/Iridium microelectrode (0.2-0.3 MΩ, MicroProbes, MD, USA) using a monopolar 5 sec pulse train (0.2 ms, 50 Hz) of cathodal current. Stimulation sites were 0.5 mm depth from cortical surface at

lobule IXb (AP, 15.4 mm; ML, 0.0 mm; DV, 6.0 mm from bregma). The intertrial interval was at least 1 min. I performed at least 30 trials for each current condition (100, 200, 300, 400 and 500 μA) in every rat.

To investigate the effects of eNpHR-mediated photoinhibition on BP during postural alterations, orange light was illuminated for 10 or 20 sec continuously in each trial (a trial was defined as 1 min period centered on the time of light onset). Thirty-degree head-up (0 → 30° head-up) and head-down (0 → -30° head-down) tilts were performed by manually rotating a tilt table (a generous gift from Dr. Nisimaru) [99] on which the stereotaxic frame was fixed. Each tilt was initiated at 1 or 10 sec after the onset of illumination. A postural change experimental session consisted of the following successive manipulations: 1) head-up tilt with orange light → 2) head-down tilt with light → 3) head-up tilt without light → 4) head-down tilt without light. Each manipulation was separated from the others by at least 2 min, and at least 20 sessions were performed for each rat. All rats were perfused with saline followed by 4% paraformaldehyde in phosphate buffer at the end of the experiment, and their EYFP fluorescence within lobule IXab were confirmed by stereoscopic fluorescence microscope analysis. ΔMAP in head-up and -down conditions was defined as differences in baseline-normalized MAP between light-ON and light-OFF conditions.

ΔMAP in resting condition was calculated by subtracting baseline value (= 1) from baseline-normalized MAP.

To estimate the effects of photoinhibition on the recovery from tilt-induced changes in BP, ΔMAP was averaged using a 3 sec time window (10-13 sec after tilt-onset for the head-up condition, 5-8 sec after tilt-onset for the head-down condition). These time windows were set at steady-state phases immediately after transient tilt-induced BP changes. Averaged ΔMAPs were then further normalized to the maximum BP change during tilts. Maximum BP changes were calculated using data from the light-OFF condition for each rat; the maximum BP change was regarded as the difference between the baseline BP and the earliest minimum (for the head-up data) or maximum (for the head-down data) value of the tilt-induced BP change.

4.1.6 Statistics

All statistical analyses were performed using SAS/STAT (SAS institute, NC, USA) and MATLAB software. Tukey-Kramer multiple comparison test was used for histological and BP data analysis. One-way repeated measures ANOVA with the Bonferroni-corrected *t*-test was used to evaluate time-dependent effects of ChR2-mediated photostimulation and eNpHR-mediated photoinhibition of lobule IXab on BP. An error bar denotes SEM except when indicated otherwise.

4.2 Results

4.2.1 Genetic targeting of ChR2- or eNpHR-expression to PCs

I used the L7 (Pcp2) promoter [37,93] to target optogenetic transgenes to PCs. The L7 promoter was shortened to 1 kb length, to load it into lentiviral vectors (abbreviated as sL7 promoter) [101]. Two lentiviral vectors were constructed, one of which was Lenti-sL7-hChR2-EYFP-WPRE, and the other one of which was Lenti-sL7-eNpHR-EYFP-WPRE (abbreviated as sL7-ChR2, sL7-eNpHR, respectively, Fig. 18). To investigate the expression pattern of ChR2-EYFP, cerebellar sections of sL7-ChR2-injected rats (sL7-ChR2 rats) were stained for calbindin-D28k, parvalbumin, NeuN and mGluR2, which are markers of Purkinje, stellate/basket, granule and Golgi cells [87,95], respectively. Strong ChR2-EYFP expression was observed in PCs (Fig. 19a–c), but not in stellate/basket cells (Fig. 19d–f), granule cells (Fig. 19g–i) or Golgi cells (Fig. 19j–l). To compare ChR2-EYFP expression among different cell types, I calculated the percentage of each cell type among all ChR2-EYFP-positive cells. Almost all of the ChR2-EYFP-positive cells were PCs (95.0 ± 2.1%, n = 4 rats, 12 sections, Fig. 19m). The percentages of stellate/basket cells and other cell types (potentially including granule, Golgi, Lugaro and unipolar brush cells) were quite low

(0.9 ± 0.5% for stellate/basket cells, 3.2 ± 2.4% for other cell types, Fig. 19m). I also estimated the transduction efficiency into each cell type to examine how effectively ChR2-EYFP was expressed in each cell type. ChR2-EYFP expression was detected in most PCs (92.6 ± 3.1%), but in only very small percentages of other cell types (0.2 ± 0.0% for stellate/basket cells, 0.0% for granule cells, 2.8 ± 2.8% for Golgi cells, Fig. 19n). These results show that the ChR2-EYFP expression induced by the sL7 promoter was highly specific to PCs.

I next examined the expression pattern of eNpHR-EYFP in sL7-eNpHR-injected rats (sL7-eNpHR rats). As in the case of ChR2, strong eNpHR-EYFP expression was observed in PCs (Fig. 20a–c). However, there was also moderate expression of eNpHR-EYFP in both stellate/basket cells and Golgi cells (indicated by arrows, Fig. 20d–f, j–l). No eNpHR-EYFP-positive granule cells were observed (Fig. 20g–i). The percentages of PCs, stellate/basket cells and other cell types among eNpHR-EYFP-positive cells were 66.5 ± 3.5, 23.1 ± 3.2 and 10.3 ± 0.7%, respectively (n = 8 rats, 24 sections for Purkinje, stellate/basket and granule cells. n = 7 rats, 21 sections for Golgi cells, Fig. 20m). Transduction efficiencies into PCs, stellate/basket cells, granule cells and Golgi cells were 95.3 ± 1.9, 7.1 ± 1.7, 0.0 and 32.7 ± 9.4%, respectively (Fig. 20n). These results suggest that the eNpHR-EYFP expression induced

by the sL7 promoter was less specific for PCs than the ChR2-EYFP expression induced by the same promoter, although the transduction efficiency into PCs was significantly higher than that into other cell types ($P < 0.01$, Tukey-Kramer multiple comparison test).

4.2.2 Electrophysiological characterization of ChR2- or eNpHR-expressing PC responses with light illumination *in vivo*

To test the functional expression of optogenetic transgenes in PCs, I performed electrophysiological single-unit recordings and examined how the firing rates of light-responsive PCs in sL7-ChR2 or sL7-eNpHR rats are affected by blue or orange light illumination *in vivo*. The blue light source used for illuminating sL7-ChR2 rat cerebellum was a DPSS laser (peak wavelength at 473 nm). I considered a neural signal to originate from a PC if it exhibited two types of spiking activities: simple spikes (SSs) and complex spikes (CSs) (Fig. 21a). SSs and CSs were judged to originate from the same PC when a transient pause (~20 ms) in SS firing followed each CS in the raw trace (Fig. 21b), and the peri-CS histogram of SSs (Fig. 21c) [96,97]. In this study, I recorded only single units identified as PCs. When a PC in sL7-ChR2 rat was illuminated by blue light, strong and time-locked elevation of SS firing rate was observed (Fig. 21d). In contrast, CS firing was not affected by blue light illumination (Fig. 21e). I recorded total

of 23 light-responsive PCs (n = 4 rats), and a histogram of their SS firing rate modulation levels are shown in Fig. 21f. All increased SS firing rate in response to blue light (median of modulation index (MI) = 1.49), and some were strongly activated to above 100% compared to spontaneous firing rates.

For electrophysiological recordings of light-responsive PCs in sL7-eNpHR rats during orange light illumination, I used another DPSS laser (peak wavelength at 593 nm). The activity of a representative light-responsive PC is shown in Fig. 22a and b. This cell strongly decreased SS firing rate in response to orange light (Fig. 22a), though eNpHR-mediated inhibition did not affect CSs (Fig. 22b). I recorded from a total of 32 light-responsive PCs (n = 7 rats), and their SS firing rate modulation levels are shown in Fig. 22c. Most of them decreased SS firing rate in response to orange light (median MI = 0.25). Although two cells slightly increased SS firing rate, SS modulation levels of these cells were relatively weak, and the percentage among all light-responsive PCs was also small (6.3%, Fig. 22c). I therefore concluded that population PC activity in sL7-eNpHR rats is strongly inhibited by orange light illumination.

4.2.3 ChR2-mediated photostimulation of PCs in the uvula provokes depressor responses

I next examined whether ChR2-mediated photostimulation of PCs within the cerebellar

uvula evokes depressor responses as well as electrical stimulation in anesthetized animals [41]. The lentiviral vectors were targeted to lobule IXab (Fig. 23a). Transgene expression in lobule IXab was confirmed by stereoscopic fluorescence microscope analysis (Fig. 23b), and also by immunohistochemical analysis of sagittal (Fig. 23c) and horizontal (Fig. 23d) sections of the cerebellum. Blue light was illuminated onto lobule IXab for 5 seconds (50 Hz, 10 ms pulses, ~50 mW/mm^2), the same duration as in the previous study of electrical stimulation [41]. I first confirmed that SS firing was strongly activated during 5-sec light illumination (n = 10 units from 2 rats, Fig. 24a–c), and then tested the effects of photostimulation on BP. When lobule IXab was illuminated by blue light, a slight decrease in BP was observed (Fig. 24d). Normalized mean arterial pressure (nMAP) averaged across animals showed that BP was significantly lower during and after light illumination than that before light onset (P < 0.01 at 5 sec, P < 0.05 at 7.5 sec after light onset, one-way repeated-measures ANOVA followed by Bonferroni-corrected t-test, n = 6 rats, Fig. 24e). The magnitude of the depressor effect induced by photostimulation (~1.3% fall) was comparable to that induced by electrical stimulation of lobule IXab using 200 μA current in anesthetized rats (Fig. 25). The effect of ChR2-mediated photostimulation of lobule IXab on BP was significantly larger than that of blue light illumination onto lobule IXab injected with

PBS or ChR2-mediated photostimulation of neighboring lobule VIII ($P < 0.05$ by Tukey-Kramer multiple comparison test, n = 3 for PBS and n = 4 for lobule VIII, Fig. 24f). These results demonstrate that activation of PCs within lobule IXab leads to depressor responses in anesthetized rats.

4.2.4 eNpHR-mediated photoinhibition of PCs in the uvula provokes pressor responses

I next examined the effects of eNpHR-mediated photoinhibition of PCs on resting BP in sL7-eNpHR rats. Orange light was continuously illuminated onto lobule IXab for 10 seconds (~50 mW/mm^2). During this period, SS firing was almost completely inhibited in the representative PC shown in Fig. 26a and 26b. CSs still fired during light illumination (Fig. 26a). The population average of SS responses to orange light showed that decrease in SS firing rate was prominent immediately after light onset, then gradually increased until light offset, and then returned to the baseline level after light offset (n = 9 units from 2 rats, Fig. 26c).

I then tested the effects of eNpHR-mediated photoinhibition on BP. When lobule IXab was illuminated by orange light, a slight increase in BP was observed (Fig. 26d). nMAP data averaged across animals showed that BP was significantly higher during and after light illumination than that before light onset ($P < 0.01$ at 10, 15 and 20 sec from

light onset, one-way repeated-measures ANOVA followed by Bonferroni-corrected *t*-test, n = 9 rats, Fig. 26e). The effect of eNpHR-mediated photoinhibition of lobule IXab was significantly larger than that of orange light illumination onto lobule IXab injected with PBS or eNpHR-mediated photoinhibition of neighboring lobule VIII ($P < 0.05$ by Tukey-Kramer multiple comparison test, n = 3 for PBS and lobule VIII, Fig. 26f). These results demonstrate that inhibition of PCs within lobule IXab of anesthetized rats leads to pressor responses, opposite those to ChR2-mediated photostimulation.

4.2.5 Photoinhibition of uvular PCs attenuates BP recovery during head-down tilts

I next examined how eNpHR-mediated photoinhibition of the uvula affected BP regulation in anesthetized rats during postural alterations. The effects of photoinhibition were investigated during 30° head-up tilts as well as 30° head-down tilts (Fig. 27a_i, b_i). BP decreased or increased transiently after a head-up tilt or head-down tilt, respectively, but then recovered to the baseline level (Fig. 27a_{ii}, b_{ii}). These results are consistent with previous observations in anesthetized cats and rabbits [27,98]. I next compared the baseline-normalized MAP between two conditions, light-ON and light-OFF, in both head-up and head-down tilt trials. In the light-ON condition, illumination with orange light was initiated 1 sec before the tilt-onsets and persisted for 10 sec. Because the

latency of eNpHR-mediated photoinhibition is millisecond-timescale (Zhang et al., 2007), orange light illumination strongly inhibits PC activity already at 1 sec after onsets of illumination. In the light-OFF condition, no light was employed. Four different trials (light-ON/head-up, light-OFF/head-up, light-ON/head-down, and light-OFF/head-down) were performed within the same experimental session, and at least 20 sessions were performed for each rat (Fig. 27a_{iii}, b_{iii}). During head-down tilts, photoinhibition of the uvula resulted in a transient increase in BP in the light-ON condition compared with the light-OFF condition (Fig. 27b_{iii}). By contrast, no effect of photoinhibition was observed during head-up tilts (Fig. 27a_{iii}).

To analyze the statistical significance of the eNpHR-mediated photoinhibition effects on BP, I compared differences in the baseline-normalized MAP (ΔMAP) between light-ON and light-OFF conditions during the 10-second period corresponding to light illumination (Fig. 28). Because photoinhibition of the uvula also evokes pressor responses during the resting condition (Fig. 25d–f), I simultaneously compared ΔMAP measured during the head-up, head-down and resting conditions. Two-way repeated measures ANOVA [factor 1, tilt condition (head-up, head-down or resting); factor 2, time] for ΔMAP showed a significant interaction between tilt condition and time ($F_{20, 180}$ = 4.11, $P < 1\times10^{-6}$, Fig. 28a). Post-hoc comparisons at each time point showed

significant differences for ΔMAP between head-up and head-down conditions ($P < 0.05$ at 4 sec, $P < 0.005$ at 2 and 5-10 sec, one-way ANOVA followed by Fisher's least significant difference (LSD) test, Fig. 28a). Furthermore, the effect of photoinhibition during head-up tilts was also significantly different from that during the resting condition ($P < 0.05$ at 8 and 10 sec, $P < 0.005$ at 9 sec, Fisher's LSD test, Fig. 28a). These results demonstrate the time-dependence of the effect of photoinhibition on BP between different tilt conditions.

To investigate the functional role of this dynamic regulation of BP by the uvula, I next evaluated whether photoinhibition differentially affected the ability of rats to recover from tilt-induced BP changes in head-up vs. head-down conditions (see Materials and Methods for calculations). ΔMAP values were normalized to reflect the ratio of ΔMAP to the maximum BP change during tilts. This analysis revealed a significant difference in BP recovery between head-up and head-down conditions ($P < 0.005$, paired *t*-test, Fig. 28b). Furthermore, the BP was unable to recover to the baseline level during head-down tilts ($P < 0.005$, *t*-test) although a full recovery was observed during head-up tilts ($P > 0.8$, *t*-test, Fig. 28b). These results suggest that PCs in the uvula dynamically regulate BP maintenance during head-down tilts.

4.2.6 Effects of 20-second photoinhibition on recovery from BP changes induced by

postural alterations

Because the effects of photoinhibition on BP were most prominent toward the end of the 10-sec period of orange light illumination (Fig. 28a), it is possible that the impact on BP immediately after tilt-onset was not fully evaluated with my initial photoinhibition protocol. I therefore performed an experiment in which the period of photoinhibition was prolonged so that its effect on BP was already prominent at tilt-onset. Uvular PCs were illuminated with orange light for a period of 10 sec before tilt-onset for a total of 20 sec in this experimental protocol. Comparison of baseline-normalized MAP between the light-ON and -OFF conditions confirmed that BP was actually increased already at the tilt-onsets in the light-ON condition (Fig. 29a,b). Consistent with the data of the 10-sec illumination protocol, recovery from tilt-induced BP change was impaired by photoinhibition during head-down tilts (Fig. 29b), but not during head-down tilts (Fig. 29a). However, comparison of ΔMAP between three tilt conditions (head-up, head-down and resting) shows that the effects of 20-sec photoinhibition immediately after the tilt-onset were more pronounced compared with those in the 10-sec protocol (particularly demonstrated in a sudden dip of ΔMAP after the tilt-onset observed in the head-up condition, Fig. 29c). Two-way repeated measures ANOVA [factor 1, tilt condition (head-up or head-down or resting); factor 2, time] for ΔMAP showed a

significant interaction between tilt condition and time ($F_{40, 200}$ = 3.18, $P < 1\times10^{-7}$, Fig. 29c). This result was consistent with the results from the previous 10-sec protocol. Post-hoc comparisons at each time point showed significant differences in ΔMAP between head-up and head-down conditions ($P < 0.05$ at 15 and 19 sec; $P < 0.005$ at 12, 14 and 16-18 sec; one-way ANOVA followed by Fisher's LSD test, Fig. 29c). Significant differences were also found between the head-up and resting conditions ($P < 0.05$ at 12 and 17 sec; $P < 0.005$ at 18 sec, Fig. 29c). These data suggest that the effects of photoinhibition were mostly consistent between the 10- and 20-sec protocols. However, the dynamics of the photoinhibition effects in 20-sec protocol, in which the variance between the head-up and the resting condition was already detected at 2 sec after tilt-onset, were slightly different compared with those in the 10-sec protocol.

Finally, I examined the effects of photoinhibition on BP recovery during tilts in the 20-sec protocol. The extent of BP recovery was significantly different between the head-up and head-down conditions ($P < 0.005$, paired *t*-test; Fig. 29d). Moreover, ΔMAP was significantly higher than zero in the head-down condition ($P < 1\times10^{-4}$, *t*-test), but not in the head-up condition ($P > 0.27$, Fig. 29d). These results further support the hypothesis that PCs in the uvula regulate BP maintenance during head-down tilts.

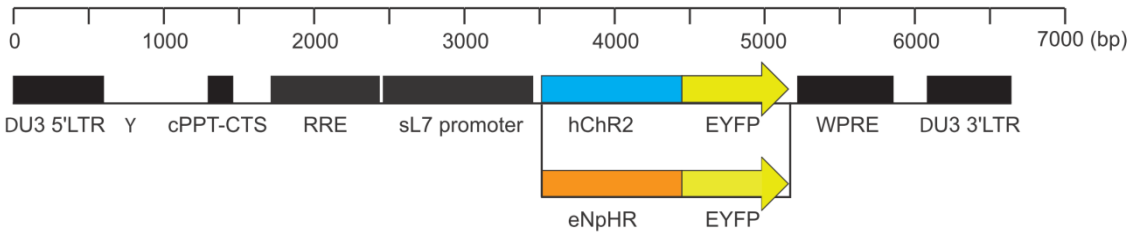

Figure 18. Schematic diagrams of the lentiviral vector constructs, Lenti-sL7-hChR2-EYFP-WPRE (sL7-ChR2) and Lenti-sL7-eNpHR-EYFP-WPRE (sL7-eNpHR). Reprinted from Tsubota et al. (2011) PLoS ONE 6: e22400, doi: 10.1371/journal.pone.0022400.

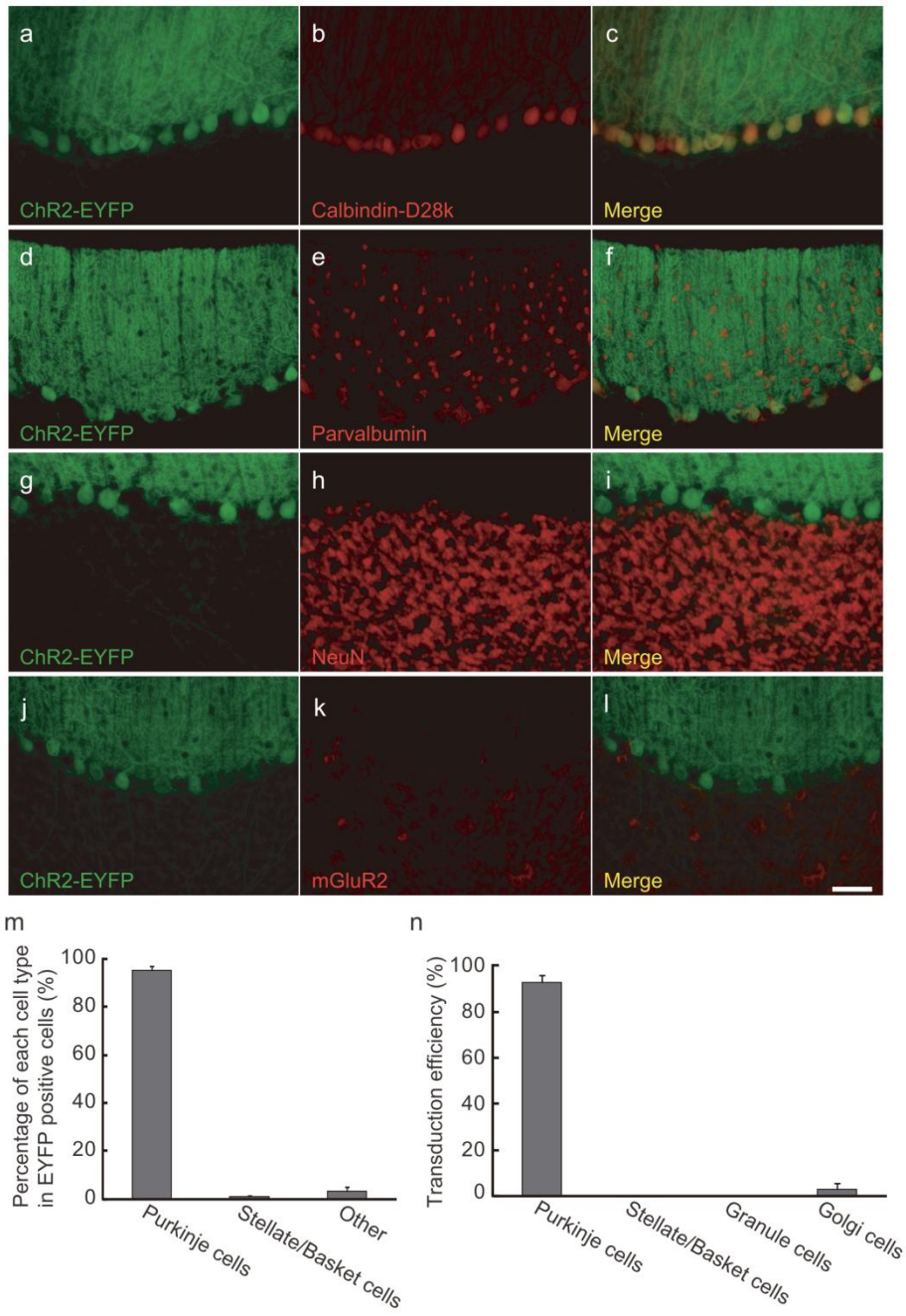

Figure 19. Immunostaining of parasagittal sections of sL7-ChR2 rat cerebellum. Four sections (a−c, d−f, g−i, j−l) are shown. Sections with EYFP fluorescence (a,d,g,j) were counterstained for calbindin-D28k (b), parvalbumin (e), NeuN (h) and mGluR2 (k), respectively. The rightmost panels (c,f,i,l) show the merged image. Scale bar, 50 μm. (m) The percentages of PCs, stellate/basket cells and other cell types among all ChR2-EYFP positive cells. (n) Transduction efficiencies into each cell type. n = 4 rats. Reprinted from Tsubota et al. (2011) PLoS ONE 6: e22400, doi: 10.1371/journal.pone.0022400.

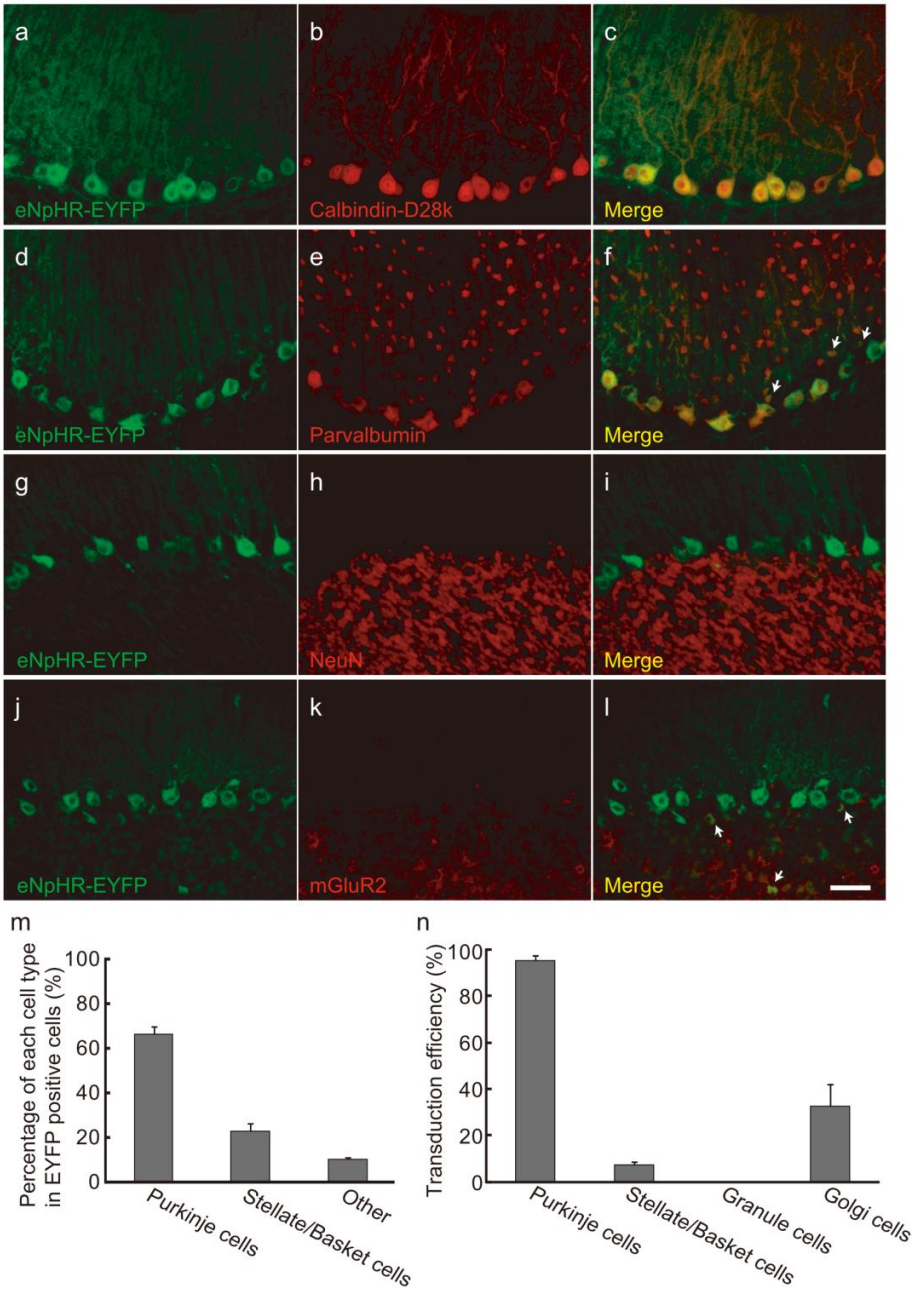

Figure 20. Immunostaining of parasagittal sections of sL7-eNpHR rats. Four sections (a–c, d–f, g–i, j–l) are shown. Sections with EYFP fluorescence (a,d,g,j) were counterstained for calbindin-D28k (b), parvalbumin (e), NeuN (h) and mGluR2 (k), respectively. The rightmost panels (c,f,i,l) show the merged image. Arrows in panel f and l indicate EYFP+/parvalbumin+ basket and EYFP+/mGluR2+ Golgi cells, respectively. Scale bar, 50 μm. (m) The percentages of PCs, stellate/basket and other cell types among all EYFP+ cells. n = 8 rats. (n) Transduction efficiencies into each cell type. n = 8 rats for Purkinje, stellate/basket and granule cells. n = 7 rats for Golgi cells.

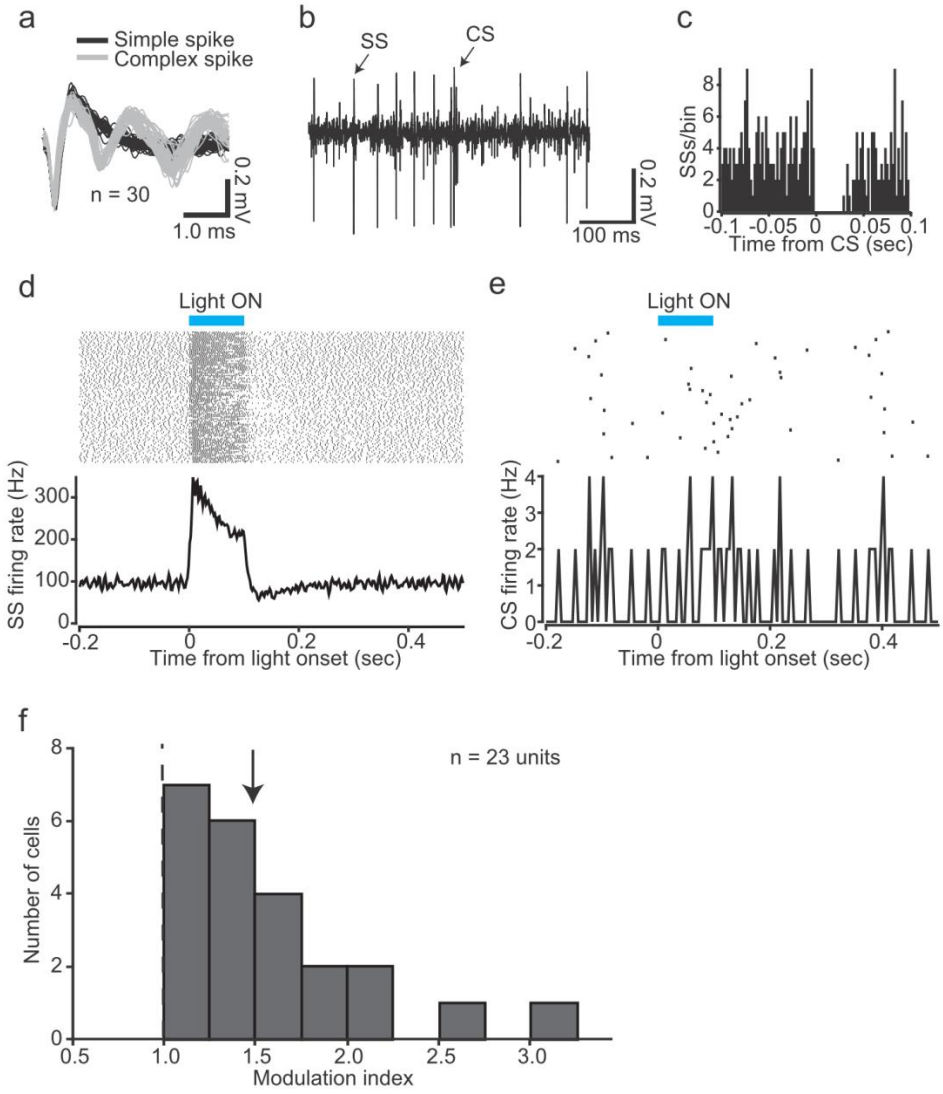

Figure 21. Electrophysiological recordings of light-evoked PC activities in sL7-ChR2 rats. (a) Waveforms of simple spikes (SSs, black lines) and complex spikes (CSs, gray lines). (b) A sample record of spontaneous activity is shown. Transient pause of SS firing was observed after a CS firing. (c) Peri-CS time histogram of SSs. This histogram indicates discharge rate of SSs before and after the occurrence of a CS. Bin width of the histogram is 1 ms. (d) Responses of SSs to blue light illumination. Shown at the top is a spike raster plot (100 trials are shown in horizontal row), and at the bottom is a peri-stimulus time histogram (PSTH), averaged across all trials (bin width, 2 ms). Period of blue light illumination is indicated by a horizontal blue bar (100 ms duration). (e) Same as D, but of CSs. Bin width of the PSTH is 5 ms. (f) A histogram of modulation index (MI) of SS firing rate. An arrow indicates the median value. n = 23 units, 4 rats. Reprinted from Tsubota et al. (2011) PLoS ONE 6: e22400, doi: 10.1371/journal.pone.0022400.

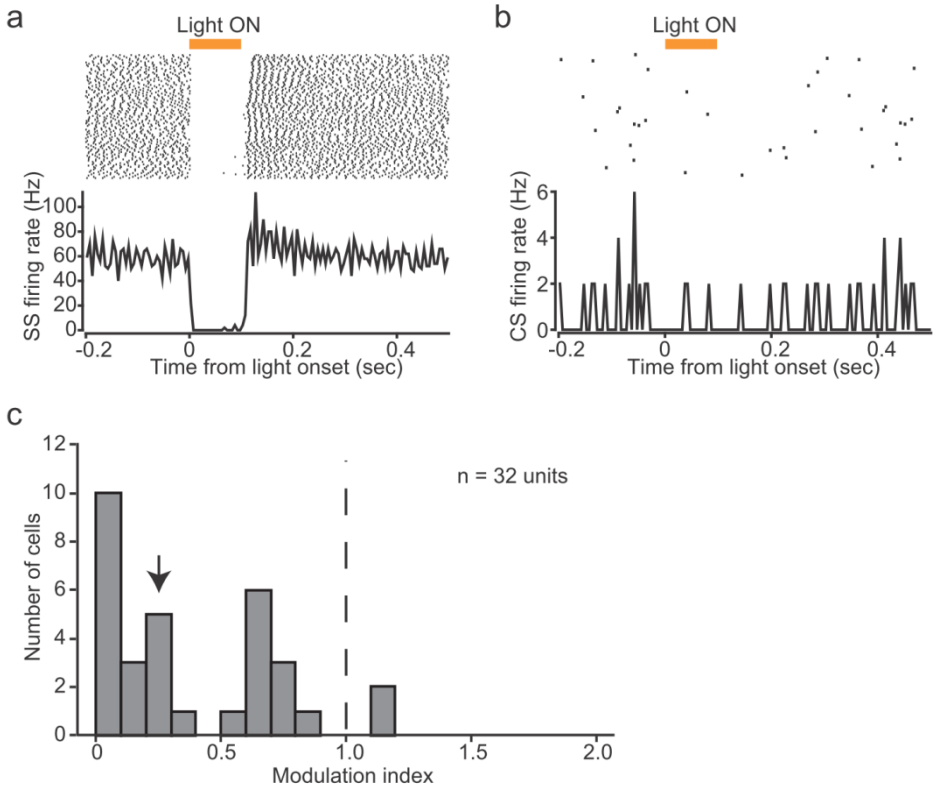

Figure 22. Electrophysiological recordings of PC activity in response to orange light illumination in sL7-eNpHR rats. (a) Responses of SSs. Shown at the top is a spike raster plot (100 trials are shown in horizontal row), and at the bottom is a PSTH, averaged across all trials (bin width, 2 ms for simple spikes). Period of orange light illumination is indicated by a horizontal orange bar (100 ms duration). (b) Same as A, but of CSs. Bin width of the PSTH is 5 ms. (c) A histogram of MI of SS firing rate. An arrow indicates the median value. n = 32 units, 7 rats. Reprinted from Tsubota et al. (2011) PLoS ONE 6: e22400, doi: 10.1371/journal.pone.0022400.

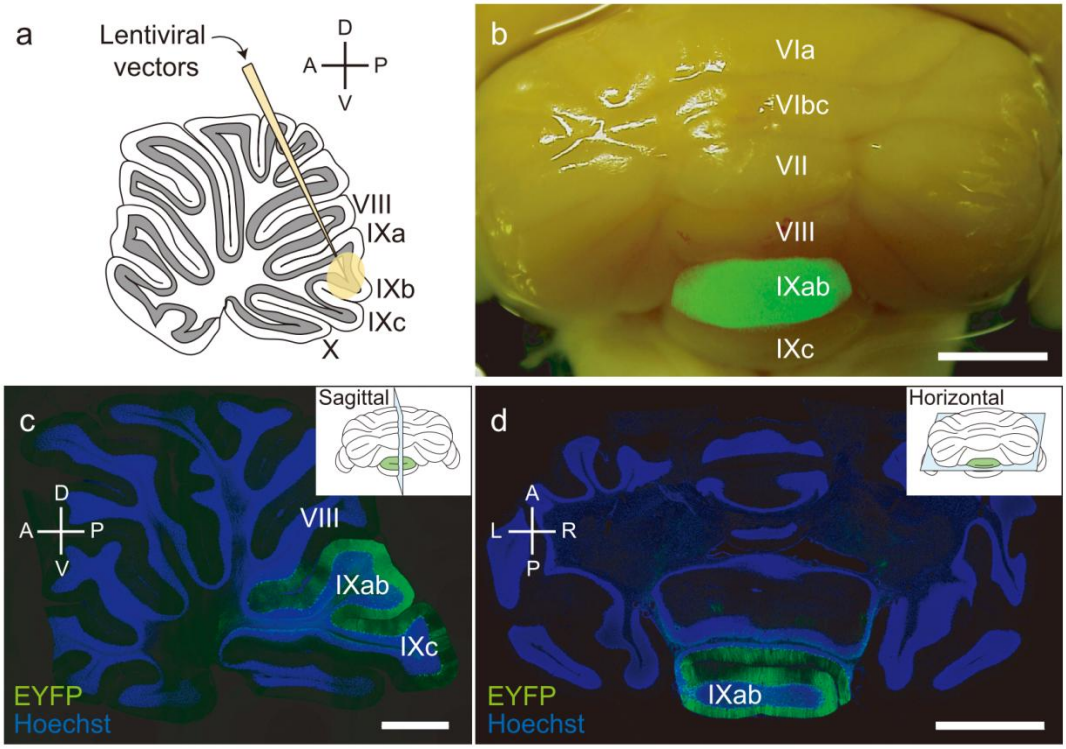

Figure 23. Lentiviral vector-mediated gene transfer into lobule IXab of rat cerebellum. (a) Schematic diagram of lentiviral vector injection into lobule IXab. (b) A representative stereoscopic fluorescent image of a cerebellum injected with sL7-eNpHR. Scale bar, 2 mm. (c,d) A representative sagittal section (c) and horizontal section (d) of lentiviral vector-injected rat cerebellum. The inset of each panel shows cutting plane of each section. EYFP fluorescence was detected mainly in the lobule IXab. Scale bars, 2 mm (b,d) and 1 mm (c). Reprinted from Tsubota et al. (2011) PLoS ONE 6: e22400, doi: 10.1371/journal.pone.0022400.

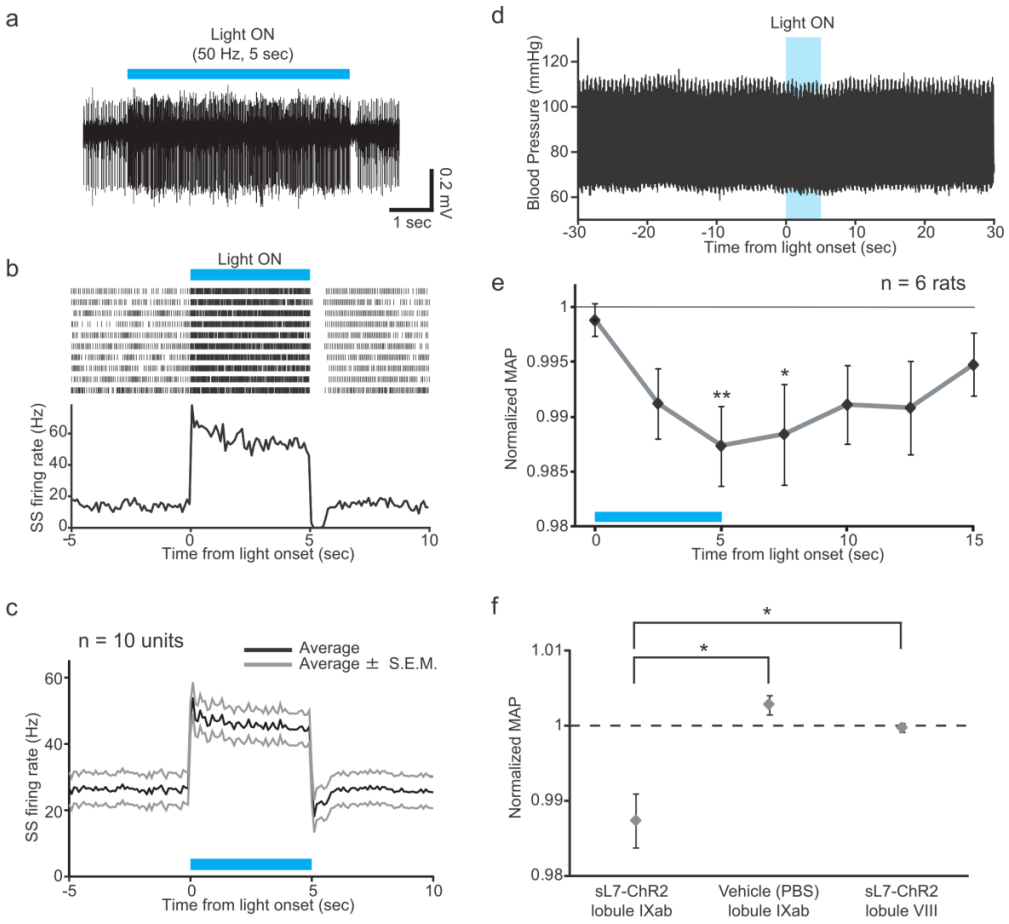

Figure 24. The effects of ChR2-mediated photostimulation of PCs in lobule IXab. (a) Photostimulation by 5 sec, 50 Hz (10 ms illumination/10 ms interval) light train (indicated by a horizontal blue bar) increased firing rate of a PC. (b) Responses of SSs to photostimulation. Shown at the top is a spike raster plot (10 trials are shown in horizontal row), and at the bottom is a PSTH, averaged across all trials (bin width, 100 ms). Period of photostimulation is indicated by a blue bar. (c) Averaged response of SSs. Black line indicates average, and gray lines indicate average ± SEM. n = 10 units, 2 rats. (d) A sample raw BP trace around the time of photostimulation. (e) BP response to photostimulation averaged across rats. *P < 0.05, **P < 0.01, one-way repeated measures ANOVA followed by Bonferroni-corrected t-test. n = 6 rats. (f) The effects of photostimulation of lobule IXab on BP were compared with that of blue light illumination onto vehicle (PBS)-injected lobule IXab (n = 3 rats) and photostimulation of lobule VIII (n = 4 rats). nMAP values averaged during the period from 4 to 5 sec after light illumination onset were plotted. *P < 0.05, Tukey-Kramer multiple comparison test. Reprinted from Tsubota et al. (2011) PLoS ONE 6: e22400, doi: 10.1371/journal.pone.0022400.

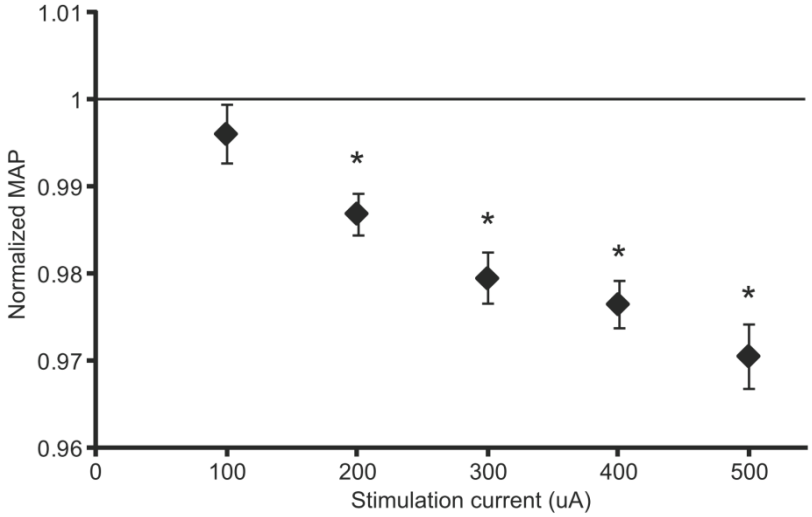

Figure 25. The effects of electrical stimulation of lobule IXab on BP. Stimulus intensity-BP change relationship was examined for stimulus condition of 100, 200, 300, 400 and 500 μA (0.2 ms pulse, 50 Hz, 5 sec). nMAP values averaged during the period from 4 to 5 sec after stimulation onset were plotted for each current condition. $P < 0.001$, one-way repeated measures ANOVA. *$P < 0.05$, Bonferroni-corrected t-test (the null hypothesis stated that the mean was equal to 1). n = 4 rats. Reprinted from Tsubota et al. (2011) PLoS ONE 6: e22400, doi: 10.1371/journal.pone.0022400.

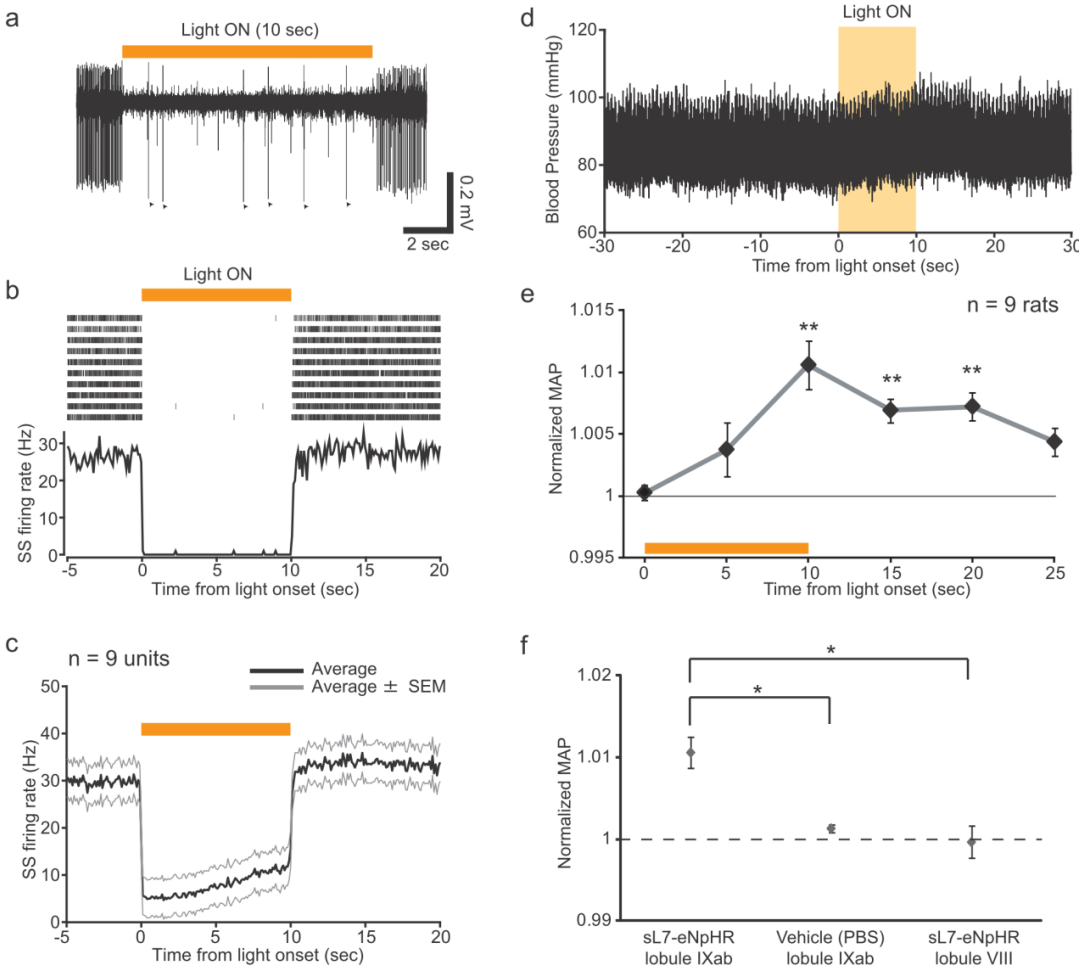

Figure 26. The effects of eNpHR-mediated inhibition of PCs in lobule IXab. (a) Ten sec continuous photoinhibition (indicated by a horizontal orange bar) decreased SS firing rate. Arrowheads indicate CSs. (b) Responses of SSs to photoinhibition. Shown at the top is a spike raster plot (10 trials are shown in horizontal row), and at the bottom is a PSTH, averaged across all trials (bin width, 100 ms). Period of photoinhibition is indicated by an orange bar. (c) Averaged response of SSs. Black line indicates average, and gray lines indicate average ± SEM. n = 9 units, 2 rats. (d) A sample raw BP trace around the time of photoinhibition. (e) BP response to photoinhibition averaged across rats. $^{**}P < 0.01$, one-way repeated measures ANOVA followed by Bonferroni-corrected *t*-test. n = 9 rats. (f) The effects of photoinhibition of lobule IXab on BP were compared with that of orange light illumination onto vehicle (PBS)-injected lobule IXab (n = 3 rats) and photoinhibition of lobule VIII (n = 3 rats). nMAP values averaged during the period from 9 to 10 sec after light illumination onset were plotted. $^{*}P < 0.05$, Tukey-Kramer multiple comparison test. Reprinted from Tsubota et al. (2011) PLoS ONE 6: e22400, doi: 10.1371/journal.pone.0022400.

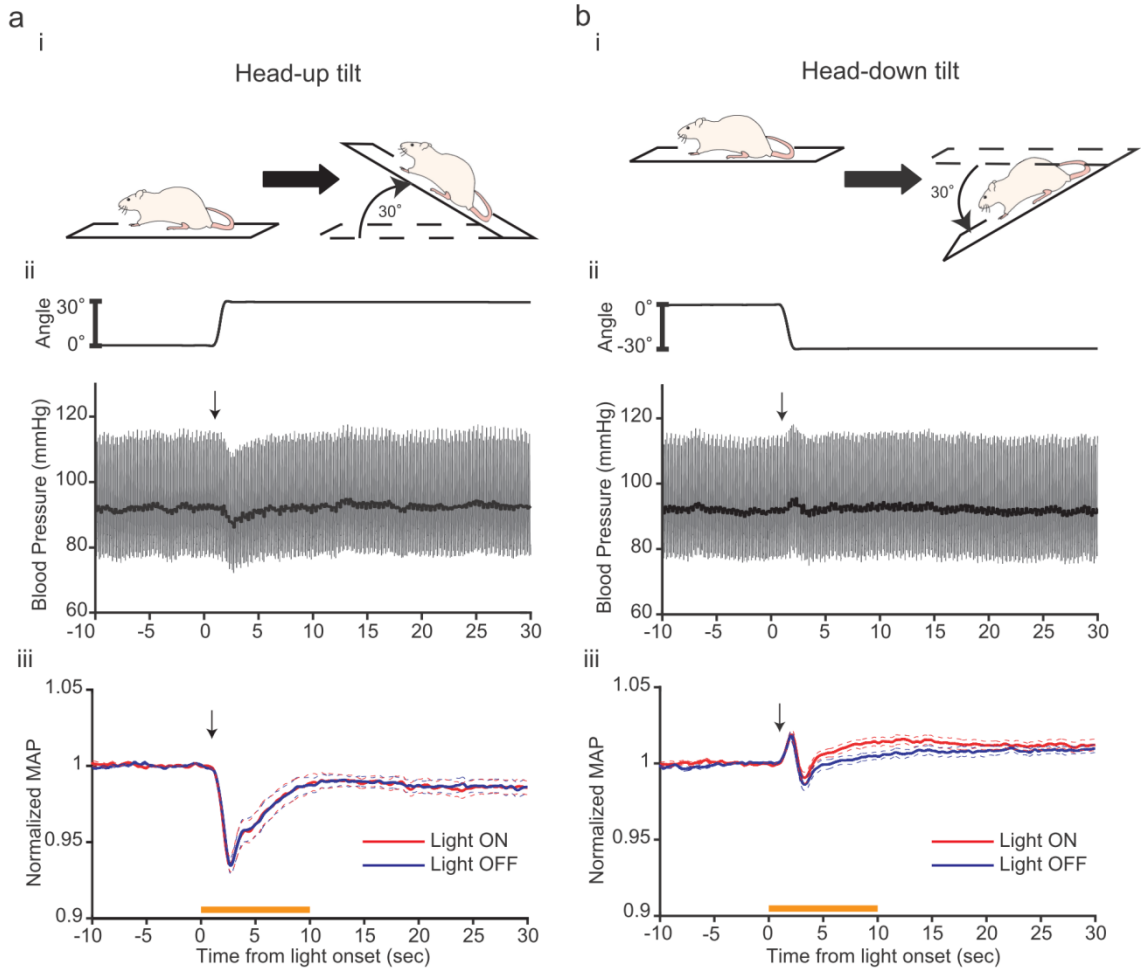

Figure 27. The effects of 10-sec photoinhibition of the uvula on BP during postural alterations in sL7-eNpHR rats. (ai, bi) Schematic diagrams of posture change experiments. (aii, bii) Sample traces of tilt angle (upper traces), raw BP (lower traces, gray) and MAP (lower traces, black) of a head-up tilt trial (aii) and a head-down tilt trial (bii). Arrows indicate the initiations of tilts. (aiii, biii) Population average time courses of baseline-normalized MAP in head-up (aiii) and head-down tilt trials (biii) with or without orange light illumination. Before averaging, MAP data of each trial was low-pass filtered at 0.5 Hz. Blue lines are of light-OFF conditions, and red lines are of light-ON conditions. Thin traces are mean ± SEM. The periods of light illumination are indicated by horizontal orange bars. n = 10 rats. Reprinted from *Neuroscience*, 210, Tsubota et al., P137-144, Copyright (2012), with permission from Elsevier.

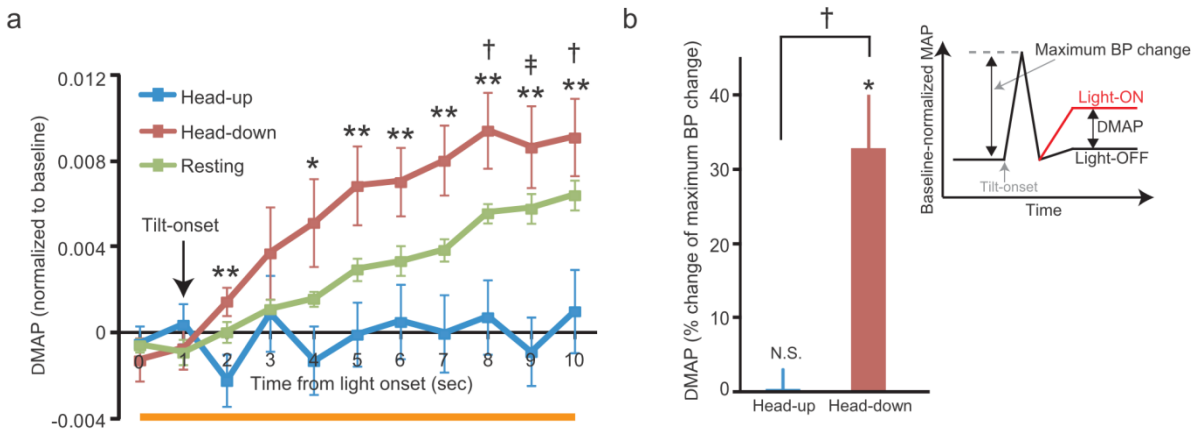

Figure 28. 10-sec photoinhibition attenuates BP recovery during head-down tilts. (a) MAP differences between light-ON and -OFF conditions (ΔMAP) in the head-up (blue), head-down (red) and resting conditions (green), respectively. An arrow indicates the tilt-onset in the head-up and head-down conditions. A significant interaction ($F_{20, 180}$ = 4.11, P < 1×10^{-6}) was revealed by two-way ANOVA with repeated measures on both factors [tilt condition (head-up, head-down, resting) × time]. *P < 0.05, **P < 0.005, difference in ΔMAP between the head-up and head-down conditions; $^{\dagger}P$ < 0.05, $^{\ddagger}P$ < 0.005, difference in ΔMAP between the head-up and resting conditions; one-way ANOVA followed by Fisher's LSD test. Width of time window used for calculating ΔMAP at each time point is 1 sec. A horizontal orange bar indicates the period of light illumination. n = 10 rats. (b) The effects of photoinhibition on the recovery from tilt-induced BP change. ΔMAP was first averaged using 3 sec time window (10-13 sec after tilt-onset for head-up condition, 5-8 sec after tilt-onset for head-down condition), and then further normalized to the maximum BP change during tilts. $^{\dagger}P$ < 0.005, paired *t*-test. *P < 0.005, *t*-test (the null hypothesis stated that the mean was equal to 0). N.S., not significant. Inset, schematic diagram of estimation of the maximum BP change and ΔMAP in the head-down condition. Reprinted from Neuroscience, 210, Tsubota et al., P137-144, Copyright (2012), with permission from Elsevier.

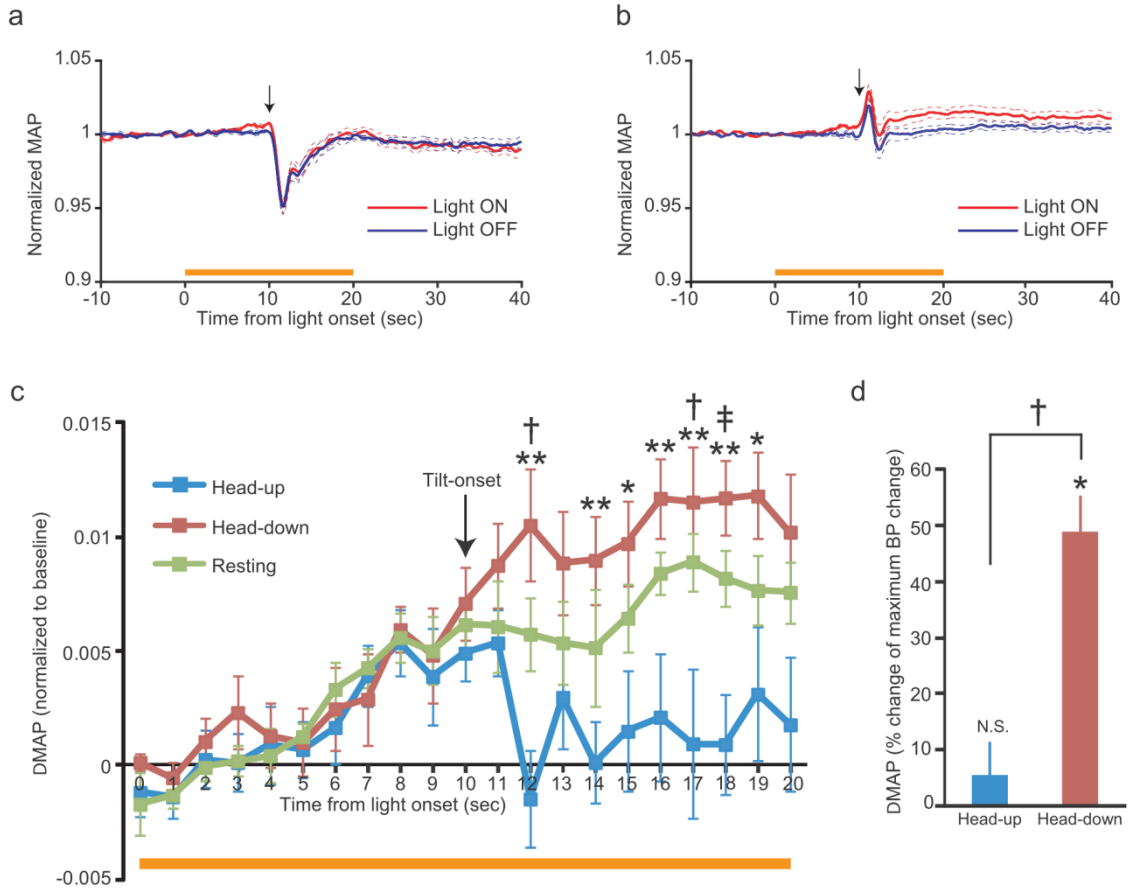

Figure 29. The effects of 20-sec photoinhibition of the uvula on BP during postural alterations. (a,b) Population average time courses of baseline-normalized MAP in the head-up (a) and head-down tilt conditions (b) with (red) or without (blue) orange light illumination. Before averaging, MAP data of each trial was low-pass filtered at 0.5 Hz. Thin traces are mean ± SEM. Arrows indicate the initiations of tilts. The periods of 20 sec orange light illumination are indicated by horizontal orange bars. n = 6 rats. (c) Same as Fig. 28a, but of the 20-sec photoinhibition protocol. A significant interaction ($F_{40, 200}$ = 3.18, $P < 1\times10^{-7}$) was revealed by two-way ANOVA with repeated measures on both factors [tilt condition (head-up, head-down, resting) × time]. *$P < 0.05$, **$P < 0.005$, difference of ΔMAP between head-up and head-down conditions; $^{\dagger}P < 0.05$, $^{\ddagger}P < 0.005$, difference of ΔMAP between head-up and resting conditions; one-way ANOVA followed by Fisher's LSD test. (D) Same as Fig. 28b, but of the 20-sec photoinhibition protocol. $^{\dagger}P < 0.005$, paired *t*-test. *$P < 0.005$, *t*-test (the null hypothesis stated that the mean was equal to 0). Reprinted from Neuroscience, 210, Tsubota et al., P137-144, Copyright (2012), with permission from Elsevier.

4.3 Discussion

In this study, I developed a method for manipulating PC activity using a lentivirus-based optogenetic technique, and then applied it to the analysis of cerebellar cardiovascular module situated in the uvula. ChR2 or eNpHR was efficiently expressed in PCs under the control of the shortened L7 promoter. All of the light-responsive PCs (23 out of 23 cells) in sL7-ChR2 rats were activated by blue light, and almost all of the light-responsive PCs (30 out of 32 cells) in sL7-eNpHR rats were inhibited by orange light. This new method of cerebellar cortex stimulation and inhibition is useful for probing the functions of specific cerebellar areas, since it can be used to manipulate the output of the cerebellar cortex alone, without affecting afferent fibers reaching the cerebellar cortex. Using this technique, I showed that the activation and inhibition of the cerebellar uvula exerted opposite effects on resting BP. I then showed that photoinhibition of the uvula attenuated BP recovery during head-down tilts.

The L7 gene promoter has been extensively utilized for cerebellar PC-specific transgene expression, mainly in transgenic mice [37,93]. The sL7 promoter used in this study had a 0.3 kb sequence upstream of the transcription start site, and included only a part of the structural gene extending from the transcription start site to upstream of the first ATG within exon 2. I used this short promoter because lentiviral titer depends on

the size of packaged inserts, heavily decreasing for large packaged inserts [40]. In a previous study, Mandolesi et al. used an 'L7 minigene', consisting of a 1 kb L7 promoter, 2 exons, and 1 intron, for transgene expression using a lentiviral vector [106]. They showed that GFP expression induced with the L7 minigene was observed mainly in PCs, with ectopic expression also observed in Golgi cells. The L7 promoter sequence of the sL7 promoter is shorter than that used by Mandolesi et al., although the expression pattern of ChR2-EYFP induced by the sL7 promoter was consistent with their observation, since ChR2-EYFP expression in a small number of Golgi cells was also observed in sL7-ChR2 rats (Fig. 19). Although the reason why the PC specificity of eNpHR-EYFP was lower than that of ChR2-EYFP is unclear, it is possible that the sequence of the eNpHR-EYFP gene interacts with L7 promoter activity in a way that promotes ectopic eNpHR-EYFP expression outside PCs [107]. Another possibility is that eNpHR-EYFP expression was affected by the transcription of upstream genes within the non-target cell genome into which the lentiviral genome was inserted [108].

Although ChR2-mediated photostimulation and eNpHR-mediated photoinhibition strongly influenced SS activity, they influenced on the CS activity very little (Fig. 21e, 22b). The mechanism of CS generation is not yet fully understood [109]; however, the following may explain my results. First, because synaptic currents evoked by climbing

fiber are quite large [104], it is possible that photocurrents induced by ChR2 and eNpHR were not sufficient to evoke or inhibit CSs. In addition to the magnitude of the current, the waveform of the stimulation current may also be important for the induction of CSs [110]. Because somatic square current pulse injection into a PC evokes spike bursts instead of physiological CSs [111], and my photostimulation protocol would induce photocurrents like square current pulses, rather than climbing fiber-evoked synaptic conductance, it is plausible that ChR2-mediated photostimulation cannot evoke physiological CSs. However, even if ChR2-mediated photostimulation and eNpHR-mediated photoinhibition cannot directly evoke or inhibit CSs, it is also possible that an enhanced or an inhibited SS firing indirectly affects CS firing through the feedback of the cerebellar cortico-nuclear-olivary circuit. Indeed, Miall et al. found that a subtle enhancement of SS firing ~150 ms before CS firing during spontaneous firing of PCs [112]. It is possible that I was unable to detect a subtle effect on CS firing under my experimental conditions, because CSs occur at low frequencies of approximately 1 Hz *in vivo* [113].

In a previous study of mouse cerebral cortex expressing ChR2 under the control of EF1α, it was shown that some portions of ChR2-negative pyramidal neurons were indirectly activated by light [59]. Lima et al. suggested that one potential source of

indirect activation is polysynaptic activation through recurrent excitatory connections including ChR2-positive neurons. In cerebellar cortex, PCs are presumed to receive inhibitory input from recurrent axon collaterals of nearby PCs activated by ChR2 [114]. In the present study, all of the light-responsive PCs in sL7-ChR2 rats increased SS firing rate in response to blue light (Fig. 21f). This finding suggests that the indirect inhibition by recurrent axon collaterals was not sufficient to inhibit the activity of ChR2-expressing PCs in the presence of direct activation of it by ChR2. In the case of eNpHR-mediated photoinhibition, I found that a small percentage of PCs (2 out of 32 cells) increased SS firing rate in response to orange light (Fig. 22c). There are several possible reasons for the PC excitation by eNpHR-mediated photoinhibition. First, inhibition of recurrent axon collaterals of PCs would lead to disinhibition of PC activity. Second, inhibition of stellate/basket cells would also lead to disinhibition of PC activity. Third, inhibition of Golgi cells would lead to disinhibition of discharge from granule cells and eventually facilitate PC firing [21]. Ectopic eNpHR expression in stellate/basket and Golgi cells observed in sL7-eNpHR rats (Fig. 20f,l,m,n) suggests the possibility that PC excitation by eNpHR-mediated photoinhibition was due to stellate/basket inhibition and/or Golgi inhibition. Nevertheless, since most light-responsive PCs in sL7-eNpHR rats decreased SS firing rate in response to orange

light (Fig. 22c), overall PC activity within lobule IXab of sL7-eNpHR rats appears to have been strongly inhibited by orange light.

ChR2-mediated photostimulation of the uvula caused ~1.3% decrease in BP, which was comparable to the effect of electrical stimulation at a current strength of 200 μA (Fig. 25). The effective current spread from an electrode tip can be expressed by $r = (I/K)^{1/2}$, where r is the distance of effective current spread from the electrode tip in mm, I is the current in μA, and K is the current-distance constant at an average of 1292 μA/mm^2 for cortical pyramidal cells when using 200 μs duration pulses [115]. If this formula is applied to my electrical stimulation experiments in the cerebellar cortex, PCs directly activated by 200 μA electrical stimulation are located within a sphere with a radius of ~0.39 mm centered at the electrode tip (surface area is ~1.9 mm^2). Because the density of PCs in the rat cerebellum is 1.0×10^3 per mm^2 [116], the number of PCs activated by 200 μA electrical stimulation was less than 1.9×10^3. In ChR2-mediated photostimulation experiments, a blue laser was illuminated onto the cerebellar surface of lobule IXab (~50 mW/mm^2 at the cerebellar cortical surface), and the diameter of the beam spot on the cortical surface was ~1.0 mm. Most PCs located deeper than 1.0 mm from the cerebellar surface were ChR2-EYFP-negative in my injection method (Fig. 23). Assuming that the light intensity is enough to activate ChR2-expressing neurons (> 1

mW/mm^2, [117]) at 1.0 mm from the cortical surface, the number of PCs activated by ChR2-mediated photostimulation is less than 4.7×10^3 [(the density of PCs) × (the surface area of a cylinder with a radius of 0.5 mm and with a height of 1.0 mm)]. This number is, at least on its order, comparable with that of electrical stimulation, suggesting that the efficiency of PC stimulation is not so different between electrical and photic stimulations.

The influence of the cerebellar uvula on cardiovascular control has been studied in rabbits and cats [27,41−43]. PCs in this region project to the lateral parabrachial nucleus, through which they connect to the solitary tract nucleus (NTS) [43]. Because NTS receives primary afferent fibers from baroreceptors and plays a fundamental role in baroreceptor reflexes, it has been suggested that cardiovascular responses caused by uvular stimulation are elicited through these connections [41]. In this study, I showed that the electrical stimulation of lobule IXb decreased BP in urethane-anesthetized rats as well as in cats and rabbits (Fig. 25), suggesting that the cardiovascular regulatory function of the uvula is preserved in rats. However, the magnitudes of depressor responses were smaller in rats than in cats and rabbits, despite similar stimulation parameters [41]. In the previous study performed using rabbits, it was shown that the electrical stimulation of lobule IXb evokes depressor responses by more than 20%

under urethane anesthesia [41]. Since my electrical stimulation experiments in rats were also performed under urethane anesthesia, the discrepancy between magnitudes of effects obtained in my study and those obtained in the previous studies is not likely to be due to the difference in anesthesia. Moreover, the difference in the stimulus (electrical stimulation vs. optogenetics) will not explain this discrepancy, as well, because the number of PCs activated by electrical stimulation and that activated by ChR2-mediated photostimulation to evoke depressor responses of the same magnitudes was not so different, as described above. Therefore, the cause of the discrepancy would be mainly due to the species difference (rats vs. cats and rabbits). Because the uvula regulates cardiovascular responses during changes in posture, a possible explanation for the species difference in uvular influence on BP is the length of the body, because the stress to the cardiovascular system during postural alteration is dependent on the length of the body, and would be more severe in animals with large bodies [118]. It is plausible that the cerebellar uvula affects more robustly the cardiovascular system in cats and rabbits than in rats.

Although electrical or chemical stimulation of the medial area of the uvula evokes a pattern of cardiovascular responses that consists of an increase in BP and heart rate accompanied by vasoconstriction in unanesthetized decerebrate cats and rabbits,

stimulation of the same area in anesthetized rabbits yields the opposite responses, i. e., a decrease in BP and heart rate accompanied by vasodilation [41]. Because of this discrepancy, it is still unclear how PC activity in the uvula affects the cardiovascular system. In the present study, I showed that ChR2-mediated photostimulation of lobule IXab decreased BP, while eNpHR-mediated photoinhibition increased it (Fig. 24e, 26e). I also showed that photostimulation and photoinhibition of lobule VIII, the neighboring lobule of IX, had no effect on BP, which is consistent with the result of electrical stimulation of lobule VIII in rabbits [41]. Blue or orange light illumination onto PBS-injected lobule IXab itself didn't affect BP (Fig. 24f, 26f). Electrophysiological recordings showed that ChR2-mediated photostimulation increased population PC activity (Fig. 24c) and eNpHR-mediated photoinhibition decreased it (Fig. 26c). Therefore I can conclude that increase or decrease in PC activity in the uvula of anesthetized rats leads to depressor or pressor responses, respectively.

Because the uvula receives vestibular information during postural alterations [119], it has been hypothesized that the uvula plays a modulatory role in the cardiovascular system during postural alterations. Indeed, in a previous study of cats, it was shown that the chronic lesioning of the uvula significantly alters cardiovascular regulation during postural alterations [47]. However, there are several drawbacks to cerebellectomy: 1) it

lacks cell-type specificity, and fibers projecting to the cerebellar cortex are also injured, 2) it is not possible to reinstate the damaged region to obtain control measures, and 3) there are often neural compensations that mask the original lesion-induced deficits [30]. In contrast, because eNpHR-mediated photoinhibition is rapidly reversible and can specifically control the activity of PCs, it can overcome these shortcomings of lesion experiments. The findings of the present study thus clearly show that PCs in the uvula regulate BP during postural alterations.

Since the effects of electrical stimulation of the uvula in rats are much smaller than those in cats and rabbits (Fig. 26), it is reasonable to anticipate that the absolute value of the magnitude of the impact of photoinhibition on BP would be comparatively small in rats (Fig. 28a, 29c). However, when ΔMAP was normalized to the maximal BP change during tilts (Fig. 28b, 29d), the extent of BP recovery during head-down tilts was reduced by 33% following photoinhibition for the 10-sec photoinhibition condition (Fig. 28b) and by 49% for the 20-sec photoinhibition condition (Fig. 29c). These results suggest that photoinhibition had a substantial impact on the BP maintenance during tilts.

Such BP regulation might be particularly important in quadrupeds such as rodents, because dorsiflexion and ventroflexion movements of the head are very common behavior during locomotion, particularly during rearing and sniffing [120]. Rapid

adjustments in circulation should take place during these movements in order to maintain stable cardiac output and brain perfusion. In the present study, the significant effects of uvula photoinhibition were observed as early as 2 sec after posture changes (Fig. 28a, 29c). This suggests that the uvula plays an important role in rapid regulation of BP during locomotion behavior.

In the cardiovascular regulatory region located in the cerebellar nodulus-uvula transition zone, it has been shown that uvular stimulation affects BP by depressing alpha-adrenergic outflow [121]. In the cardiovascular region focused in the present study, it has been suggested that sympathetic nervous system (and therefore the adrenergic system) also plays an important role in regulation of BP [42]. Therefore, pressor responses that are induced by photoinhibition during the resting condition might potentially be explained by simple disinhibition of a tonic cerebellar effect. However, effects of photoinhibition during tilts cannot be explained by mere disinhibition of a tonic cerebellar effect, because the photoinhibition effects on BP were dynamically different between the three conditions employed in the current study (head-up, head-down and resting, Fig. 28a, 29c). Furthermore, BP was not elevated by photoinhibition during the head-up tilt condition (Fig. 28a, 29c).

The dynamics of the BP response during head-up/down tilts is known to be divided

into three phases: 1) the uncompensated phase corresponding to the initial elevation in BP, 2) the early compensated phase when BP is recovering, and 3) the steady-state adjustment phase when BP is stabilized in spite of the maintained tilt [98,115]. In both 10- and 20-sec photoinhibition experiments, the effects of photoinhibition were decidedly prominent during the early compensated and the steady-state adjustment phases (Fig. 28a, 29c). However, the effects of photoinhibition during the early compensated phase were even more pronounced in the 20-sec compared with the 10-sec experiments. This was particularly well-illustrated by the sudden drop in ΔMAP after tilt-onset in the head-up condition (Fig. 29c). Because the baroreceptor reflex plays a fundamental role in BP recovery during both the early compensated phase and the steady-state adjustment phase [123], one possible explanation for my observations in the 20-sec experiments is that the early initiation of photoinhibition may in turn have caused an adaptation in the neurons related to the central baroreflex system before the tilt-onset, which accordingly limited the ability of the BP to recover during the early compensated phase.

In conclusion, together with the fact that PCs in the uvula are indirectly connected to the NTS and other brainstem nuclei that participate in the baroreceptor reflex (Bradley et al., 1991), it's tempting to suggest that PCs in the uvula dynamically act on the

baroreceptor reflex, and promote the recovery of BP to the baseline level in the steady-state adjustment phase.

5. Conclusion

The present thesis investigated functional modularity in the cerebral and cerebellar cortices of rats from two different perspectives. Because these cortices have a mostly uniform structure throughout the entire cerebrum and cerebellum, it is generally difficult to spatially restrict the perturbation of gene expression or neuronal activity to a particular cortical region of interest. To solve this problem, I employed the lentivirus-based system, and showed that genetic manipulation could be spatially restricted to cortical structures such as a functional neocortical column (Fig. 3) and a cerebellar lobule (Fig. 23). However, cerebral and cerebellar cortices seem to have different properties with regard to diffusibility of injected virus solution. In the cerebellar cortex, virus solution can diffuse more easily. Therefore, injection of a small volume (200 nl) would result in labeling relatively large area in the cerebellar cortex compared to cerebral cortex. To specifically investigate small cerebellar modules such as microzones (Ito, 2006), it may be needed to further decrease the volume of virus injection.

The technique of targeted virus injection via the functional imaging technique (Fig. 3a-c) can be applied to various cortical columns other than barrel columns. The experimental approaches outlined here, therefore, provide new insights into the

functional organization of the cerebral and cerebellar cortices, and are expected to greatly facilitate further investigations of brain function that require the isolation of specific areas. However, there are still technical challenges to overcome in terms of restricting the effects of an experimental perturbation within particular kind of structures, such as thin cortical layers within cerebral (e.g., layer 2) and cerebellar (e.g., molecular layer) cortices. Further confinement of the "spread" of gene manipulation is therefore necessary to investigate precise functions in such structures. The advancement of more refined experimental techniques (such as the optical control of gene expression; [124]) is anticipated to allow the achievement of this goal in the near future.

6. References

[1] Mountcastle VB. Modality and topographic properties of single neurons of cat's somatic sensory cortex. *J. Neurophysiol.* **20**, 408-34 (1957).

[2] Hawrylycz MJ, Lein ES, Guillozet-Bongaarts AL, Shen EH, Ng L, Miller JA, van de Lagemaat LN, Smith KA, Ebbert A, Riley ZL, Abajian C, Beckmann CF, Bernard A, Bertagnolli D, Boe AF, Cartagena PM, Chakravarty MM, Chapin M, Chong J, Dalley RA, Daly BD, Dang C, Datta S, Dee N, Dolbeare TA, Faber V, Feng D, Fowler DR, Goldy J, Gregor BW, Haradon Z, Haynor DR, Hohmann JG, Horvath S, Howard RE, Jeromin A, Jochim JM, Kinnunen M, Lau C, Lazarz ET, Lee C, Lemon TA, Li L, Li Y, Morris JA, Overly CC, Parker PD, Parry SE, Reding M, Royall JJ, Schulkin J, Sequeira PA, Slaughterbeck CR, Smith SC, Sodt AJ, Sunkin SM, Swanson BE, Vawter MP, Williams D, Wohnoutka P, Zielke HR, Geschwind DH, Hof PR, Smith SM, Koch C, Grant SG, Jones AR. An anatomically comprehensive atlas of the adult human brain transcriptome. *Nature* **489**, 391-9 (2012).

[3] Goldstone RL. Perceptual learning. *Annu. Rev. Psychol.* **49**, 585-612 (1998).

[4] Yang T, Maunsell JH. The effect of perceptual learning on neuronal responses in monkey visual area V4. *J. Neurosci.* **24**, 1617-26 (2004).

[5] Fox K. Anatomical pathways and molecular mechanisms for plasticity in the barrel cortex. *Neuroscience* **111**, 799-814 (2002).

[6] Stegmeier F, Hu G, Rickles RJ, Hannon GJ, Elledge SJ. A lentiviral microRNA-based system for single-copy polymerase II-regulated RNA interference in mammalian cells. *Proc. Natl. Acad. Sci. U S A* **102**, 13212-7 (2005).

[7] Yizhar O, Fenno LE, Davidson TJ, Mogri M, Deisseroth K. Optogenetics in neural systems. *Neuron* **71**,9-34 (2011).

[8] Petersen CC. The functional organization of the barrel cortex. *Neuron* **56**, 339-55 (2007).

[9] Feldman DE, Brecht M. Map plasticity in somatosensory cortex. *Science* **310**, 810-5 (2005).

[10] Holtmaat A, Wilbrecht L, Knott GW, Welker E, Svoboda K. Experience-dependent and cell-type-specific spine growth in the neocortex. *Nature* **441**, 979-83 (2006).

[11] Wilbrecht L, Holtmaat A, Wright N, Fox K, Svoboda K. Structural plasticity underlies experience-dependent functional plasticity of cortical circuits. *J. Neurosci.* **30**, 4927-32 (2010).

[12] Cheetham CE, Barnes SJ, Albieri G, Knott GW, Finnerty GT. Pansynaptic Enlargement at Adult Cortical Connections Strengthened by Experience. *Cereb.*

Cortex, Advanced Online Publication (2012).

[13] Matus A. Actin-based plasticity in dendritic spines. *Science* **290**,754-8 (2000).

[14] Tsubota T, Ohashi Y, Tamura K. Optogenetics in the cerebellum: Purkinje cell-specific approaches for understanding local cerebellar functions. *Behav. Brain Res.* **255**, 26-34 (2013).

[15] Fukazawa Y, Saitoh Y, Ozawa F, Ohta Y, Mizuno K, Inokuchi K. Hippocampal LTP is accompanied by enhanced F-actin content within the dendritic spine that is essential for late LTP maintenance in vivo. *Neuron* **38**, 447-60 (2003).

[16] Cingolani LA, Goda Y. Actin in action: the interplay between the actin cytoskeleton and synaptic efficacy. *Nat. Rev. Neurosci.* **9**, 344-56 (2008).

[17] Hayama T, Noguchi J, Watanabe S, Takahashi N, Hayashi-Takagi A, Ellis-Davies GC, Matsuzaki M, Kasai H. GABA promotes the competitive selection of dendritic spines by controlling local Ca(2+) signaling. *Nat. Neurosci.* **16**, 1409-16 (2013).

[18] Rust MB, Gurniak CB, Renner M, Vara H, Morando L, Görlich A, Sassoè-Pognetto M, Banchaabouchi MA, Giustetto M, Triller A, Choquet D, Witke W. Learning, AMPA receptor mobility and synaptic plasticity depend on n-cofilin-mediated actin dynamics. *EMBO J.* **29**, 1889-902 (2010).

[19] Gu J, Lee CW, Fan Y, Komlos D, Tang X, Sun C, Yu K, Hartzell HC, Chen G,

Bamburg JR, Zheng JQ. ADF/cofilin-mediated actin dynamics regulate AMPA receptor trafficking during synaptic plasticity. *Nat. Neurosci.* **13**, 1208-15 (2010).

[20] Wang Y, Dong Q, Xu XF, Feng X, Xin J, Wang DD, Yu H, Tian T, Chen ZY. Phosphorylation of cofilin regulates extinction of conditioned aversive memory via AMPAR trafficking. *J. Neurosci.* **33**, 6423-33 (2013).

[21] Ito M. Cerebellar circuitry as a neuronal machine. *Prog. Neurobiol.* **78**, 272-303 (2006).

[22] Oscarsson O. Functional units of the cerebellum: sagittal zones and microzones. *Trends. Neurosci.* **2**,143-5 (1979).

[23] Oscarsson O, Uddenberg N. Somatotopic termination of spino-olivocerebellar path. *Brain Res.* **3**, 204-7 (1966).

[24] Apps R, Hawkes R. Cerebellar cortical organization: a one-map hypothesis. *Nat. Rev. Neurosci.* **10**, 670-81 (2009).

[25] Nagao S, Ito M, Karachot L. Eye field in the cerebellar flocculus of pigmented rabbits determined with local electrical stimulation. *Neurosci. Res.* **3**, 39-51 (1985).

[26] Noda H. Cerebellar control of saccadic eye movements: its neural mechanisms and pathways. *Jpn. J. Physiol.* **41**, 351-68 (1991).

[27] Nisimaru N. Cardiovascular modules in the cerebellum. *Jpn. J. Physiol.* **54**, 431-48

(2004).

[28] Botterell EH, Fulton JG. Functional localization in the cerebellum of primates II. Lesions of midline structures (vermis) and deep nuclei. *J. Comp. Neurol.* **69**, 47-62 (1938).

[29] Dow, R.S., Moruzzi, G. *The Physiology and Pathology of the Cerebellum.* (University of Minnesota Press, Minneapolis, 1958).

[30] Lomber SG. The advantages and limitations of permanent or reversible deactivation techniques in the assessment of neural function. *J. Neurosci. Methods.* **86**, 109-17 (1999).

[31] Attwell PJ, Cooke SF, Yeo CH. Cerebellar function in consolidation of a motor memory. *Neuron* **34**, 1011-20 (2002).

[32] Histed MH, Bonin V, Reid RC. Direct activation of sparse, distributed populations of cortical neurons by electrical microstimulation. *Neuron* **63**, 508-22 (2009).

[33] Gao W, Chen G, Reinert KC, Ebner TJ. Cerebellar cortical molecular layer inhibition is organized in parasagittal zones. *J. Neurosci.* **26**, 8377-87 (2006).

[34] Goshen I, Brodsky M, Prakash R, Wallace J, Gradinaru V, Ramakrishnan C, et al. Dynamics of retrieval strategies for remote memories. *Cell* **147**, 678-89 (2011).

[35] Fenno L, Yizhar O, Deisseroth K. The development and application of optogenetics.

Annu. Rev. Neurosci. **34**, 389-412 (2011).

[36] Zhang F, Wang LP, Brauner M, Liewald JF, Kay K, Watzke N, Wood PG, Bamberg E, Nagel G, Gottschalk A, Deisseroth K. Multimodal fast optical interrogation of neural circuitry. *Nature* **446**, 633-9 (2007).

[37] Oberdick J, Smeyne RJ, Mann JR, Zackson S, Morgan JI. A promoter that drives transgene expression in cerebellar Purkinje and retinal bipolar neurons. *Science* **248**, 223-6 (1990).

[38] Oberdick J, Schilling K, Smeyne RJ, Corbin JG, Bocchiaro C, Morgan JI. Control of segment-like patterns of gene expression in the mouse cerebellum. *Neuron* **10**, 1007-18 (1993).

[39] Serinagaoglu Y, Zhang R, Zhang Y, Zhang L, Hartt G, Young AP, et al. A promoter element with enhancer properties, and the orphan nuclear receptor RORalpha, are required for Purkinje cell-specific expression of a Gi/o modulator. *Mol. Cell. Neurosci.* **34**, 324-42 (2007).

[40] al Yacoub N, Romanowska M, Haritonova N, Foerster J. Optimized production and concentration of lentiviral vectors containing large inserts. *J. Gene. Med.* **9**, 579-84 (2007).

[41] Bradley DJ, Ghelarducci B, Paton JF, Spyer KM. The cardiovascular responses

elicited from the posterior cerebellar cortex in the anaesthetized and decerebrate rabbit. *J. Physiol.* **383**, 537-50 (1987).

[42] Bradley DJ, Ghelarducci B, Spyer KM. The role of the posterior cerebellar vermis in cardiovascular control. *Neurosci. Res.* **12**:45-56, 1991.

[43] Paton JF, Spyer KM. Brain stem regions mediating the cardiovascular responses elicited from the posterior cerebellar cortex in the rabbit. *J. Physiol.* **427**:533-552, 1990.

[44] Barman SM, Gebber GL. The posterior vermis of the cerebellum selectively inhibits 10-Hz sympathetic nerve discharge in anesthetized cats. *Am. J. Physiol. Regul. Integr. Comp. Physiol.* **297**:R210-217, 2009.

[45] La Noce A, Bradley DJ, Goring MA, Spyer KM. The influence of lobule IX of the cerebellar posterior vermis on the baroreceptor reflex in the decerebrate rabbit. *J. Auton. Nerv. Syst.* **32**:31-36, 1991.

[46] Yates BJ, Holmes MJ, Jian BJ. Adaptive plasticity in vestibular influences on cardiovascular control. *Brain Res. Bull.* **53**:3-9, 2000.

[47] Holmes MJ, Cotter LA, Arendt HE, Cass SP, Yates BJ. Effects of lesions of the caudal cerebellar vermis on cardiovascular regulation in awake cats. *Brain Res.* **938**:62-72, 2002.

[48] Tsubota T, Ohashi Y, Tamura K, Sato A, Miyashita Y. Optogenetic manipulation of cerebellar Purkinje cell activity *in vivo*. *PLoS One* **6**:e22400, 2011.

[49] Tsubota T, Ohashi Y, Tamura K, Miyashita Y. Optogenetic inhibition of Purkinje cell activity reveals cerebellar control of blood pressure during postural alterations in anesthetized rats. *Neuroscience* **210**:137-44, 2012.

[50] Hanawa H, Kelly PF, Nathwani AC, Persons DA, Vandergriff JA, Hargrove P, Vanin EF, Nienhuis AW. Comparison of various envelope proteins for their ability to pseudotype lentiviral vectors and transduce primitive hematopoietic cells from human blood. *Mol. Ther.* **5**:242-251, 2002.

[51] Sastry L, Johnson T, Hobson MJ, Smucker B, Cornetta K. Titering lentiviral vectors: comparison of DNA, RNA and marker expression methods. *Gene Ther.* **9**:1155-1162, 2002.

[52] Tamura K, Ohashi Y, Tsubota T, Takeuchi D, Hirabayashi T, Yaguchi M, Matsuyama M, Sekine T, Miyashita Y. A glass-coated tungsten microelectrode enclosing optical fibers for optogenetic exploration in primate deep brain structures. *J. Neurosci. Methods* **211**:49-57, 2012.

[53] Brecht M, Roth A, Sakmann B. Dynamic receptive fields of reconstructed pyramidal cells in layers 3 and 2 of rat somatosensory barrel cortex. *J. Physiol.*

553:243-65, 2003.

[54] Jacob V, Petreanu L, Wright N, Svoboda K, Fox K. Regular spiking and intrinsic bursting pyramidal cells show orthogonal forms of experience-dependent plasticity in layer V of barrel cortex. *Neuron* **73**, 391-404 (2012).

[55] Armstrong-James M, Fox K. Spatiotemporal convergence and divergence in the rat S1 "barrel" cortex. *J. Comp. Neurol.* **26**, 265-81 (1987).

[56] Cohen JY, Haesler S, Vong L, Lowell BB, Uchida N. Neuron-type-specific signals for reward and punishment in the ventral tegmental area. *Nature* **482**, 85-8 (2012).

[57] Wong-Riley M. Changes in the visual system of monocularly sutured or enucleated cats demonstrable with cytochrome oxidase histochemistry. *Brain Res.* **17**, 11-28 (1979).

[58] Zhang SJ, Ye J, Miao C, Tsao A, Cerniauskas I, Ledergerber D, Moser MB, Moser EI. Optogenetic dissection of entorhinal-hippocampal functional connectivity. *Science* **340**, 1232627 (2013).

[59] Lima SQ, Hromádka T, Znamenskiy P, Zador AM. PINP: a new method of tagging neuronal populations for identification during in vivo electrophysiological recording. *PLoS One* **4**, e6099 (2009).

[60] Polley DB, Chen-Bee CH, Frostig RD. Two directions of plasticity in the

sensory-deprived adult cortex. *Neuron* **24**, 623-637 (1999).

[61] Margolis DJ, Lütcke H, Schulz K, Haiss F, Weber B, Kügler S, Hasan MT, Helmchen F. Reorganization of cortical population activity imaged throughout long-term sensory deprivation. *Nat. Neurosci.* **15**,1539-1546 (2012).

[62] Yaguchi M, Ohashi Y, Tsubota T, Sato A, Koyano KW, Wang N, Miyashita Y. Characterization of the properties of seven promoters in the motor cortex of rats and monkeys after lentiviral vector-mediated gene transfer. *Hum. Gene. Ther. Methods* **24**, 333-344 (2013).

[63] Aronoff R, Petersen C. Layer- and column-specific knockout of NMDA receptors in pyramidal neurons of the mouse barrel cortex. *Front. Integr. Neurosci.* **1**, 1 (2007).

[64] Grinvald A, Lieke E, Frostig RD, Gilbert CD, Wiesel TN. Functional architecture of cortex revealed by optical imaging of intrinsic signals. *Nature* **324**, 361-364 (1986).

[65] Adesnik H, Scanziani M. Lateral competition for cortical space by layer-specific horizontal circuits. *Nature* **464**, 1155-1160 (2010).

[66] Racz B, Weinberg RJ. Spatial organization of cofilin in dendritic spines. *Neuroscience* **138**, 447-56 (2006).

[67] Cheetham CE, Hammond MS, Edwards CE, Finnerty GT. Sensory experience alters

cortical connectivity and synaptic function site specifically. *J. Neurosci.* **27**, 3456-3465 (2007).

[68] Glazewski S, Fox K. Time course of experience-dependent synaptic potentiation and depression in barrel cortex of adolescent rats. *J. Neurophysiol.* **75**, 1714-1729 (1996).

[69] Cullen BR. Enhancing and confirming the specificity of RNAi experiments. *Nat. Methods* **3**, 677-81 (2006).

[70] Petreanu L, Mao T, Sternson SM, Svoboda K. The subcellular organization of neocortical excitatory connections. *Nature* **457**, 1142-5 (2009).

[71] Makino H, Malinow R. Compartmentalized versus global synaptic plasticity on dendrites controlled by experience. *Neuron* **72**, 1001-1011 (2011).

[72] Chen JL, Villa KL, Cha JW, So PT, Kubota Y, Nedivi E. Clustered dynamics of inhibitory synapses and dendritic spines in the adult neocortex. *Neuron* **74**, 361-373 (2012).

[73] Fu M, Yu X, Lu J, Zuo Y. Repetitive motor learning induces coordinated formation of clustered dendritic spines in vivo. *Nature* **483**, 92-95 (2012).

[74] Cauli B, Audinat E, Lambolez B, Angulo MC, Ropert N, Tsuzuki K, Hestrin S, Rossier J. Molecular and physiological diversity of cortical nonpyramidal cells. *J.*

Neurosci. **17**, 3894-3906 (1997).

[75] Brennecke J, Stark A, Russell RB, Cohen SM. Principles of microRNA-target recognition. *PLoS Biol.* **3**, e85 (2005).

[76] Trachtenberg JT, Chen BE, Knott GW, Feng G, Sanes JR, Welker E, Svoboda K. Long-term in vivo imaging of experience-dependent synaptic plasticity in adult cortex. *Nature* **420**, 788-94 (2002).

[77] Marik SA, Yamahachi H, McManus JN, Szabo G, Gilbert CD. Axonal dynamics of excitatory and inhibitory neurons in somatosensory cortex. *PLoS Biol.* **8**, e1000395 (2010).

[78] Lübke J, Roth A, Feldmeyer D, Sakmann B. Morphometric analysis of the columnar innervation domain of neurons connecting layer 4 and layer 2/3 of juvenile rat barrel cortex. *Cereb. Cortex.* **13**:1051-63 (2003).

[79] Glazewski S, Giese KP, Silva A, Fox K. The role of alpha-CaMKII autophosphorylation in neocortical experience-dependent plasticity. *Nat Neurosci.* **3**, 911-918 (2000).

[80] Silva AJ, Stevens CF, Tonegawa S, Wang Y. Deficient hippocampal long-term potentiation in alpha-calcium-calmodulin kinase II mutant mice. *Science* **257**, 201-206 (1992).

[81] Bamburg JR. Proteins of the ADF/cofilin family: essential regulators of actin dynamics. *Annu. Rev. Cell Dev. Biol.* **15**,185-230 (1999).

[82] Mulkey RM, Endo S, Shenolikar S, Malenka RC. Involvement of a calcineurin/inhibitor-1 phosphatase cascade in hippocampal long-term depression. *Nature* **369**, 486-488 (1994).

[83] Zhou Q, Homma KJ, Poo MM. Shrinkage of dendritic spines associated with long-term depression of hippocampal synapses. *Neuron* **44**, 749-57 (2004).

[84] Allen CB, Celikel T, Feldman DE. Long-term depression induced by sensory deprivation during cortical map plasticity in vivo. *Nat. Neurosci.* **6**, 291-9 (2003).

[85] Bender KJ, Allen CB, Bender VA, Feldman DE. Synaptic basis for whisker deprivation-induced synaptic depression in rat somatosensory cortex. *J. Neurosci.* **26**, 4155-65 (2006).

[86] Arber S, Barbayannis FA, Hanser H, Schneider C, Stanyon CA, Bernard O, Caroni P. Regulation of actin dynamics through phosphorylation of cofilin by LIM-kinase. *Nature* **393**, 805-809 (1998).

[87] Merla G, Howald C, Henrichsen CN, Lyle R, Wyss C, Zabot MT, Antonarakis SE, Reymond A. Submicroscopic deletion in patients with Williams-Beuren syndrome influences expression levels of the nonhemizygous flanking genes. *Am. J. Hum.*

Genet. **79**, 332-341 (2006).

[88] Martens MA, Wilson SJ, Reutens DC. Research Review: Williams syndrome: a critical review of the cognitive, behavioral, and neuroanatomical phenotype. *J. Child Psychol. Psychiatry* **49**, 576-608 (2008).

[89] Mountcastle VB. The columnar organization of the neocortex. *Brain* **120**, 701-722 (1997).

[90] Yamahachi H, Marik SA, McManus JN, Denk W, Gilbert CD. Rapid axonal sprouting and pruning accompany functional reorganization in primary visual cortex. *Neuron* **64**, 719-729 (2009).

[91] Yoshida M, Naya Y, Miyashita Y. Anatomical organization of forward fiber projections from area TE to perirhinal neurons representing visual long-term memory in monkeys. *Proc. Natl. Acad. Sci. USA* **100**, 4257-4262 (2003).

[92] Gilbert CD, Li W. Adult visual cortical plasticity. *Neuron* **75**, 250-264 (2012).

[93] Paxinos G, Watson C. *The rat brain in stereotaxic coordinates* (Elsevier, San Diego, 2007).

[94] Neki A, Ohishi H, Kaneko T, Shigemoto R, Nakanishi S, Mizuno N. Pre- and postsynaptic localization of a metabotropic glutamate receptor, mGluR2, in the rat brain: an immunohistochemical study with a monoclonal antibody. *Neurosci. Lett.*

202, 197-200 (1996).

[95] Thach WT, Jr. Somatosensory receptive fields of single units in cat cerebellar cortex. *J. Neurophysiol*. **30**, 675-696 (1967).

[96] Cardin JA, Carlen M, Meletis K, Knoblich U, Zhang F, Deisseroth K, Tsai LH, Moore CI. Targeted optogenetic stimulation and recording of neurons in vivo using cell-type-specific expression of Channelrhodopsin-2. *Nat. Protoc.* **5**, 247-254 (2010).

[97] Han X, Qian X, Bernstein JG, Zhou HH, Franzesi GT, Stern P, Bronson RT, Graybiel AM, Desimone R, Boyden ES. Millisecond-timescale optical control of neural dynamics in the nonhuman primate brain. *Neuron* **62**, 191-198 (2009).

[98] Abbott SB, Stornetta RL, Fortuna MG, Depuy SD, West GH, Harris TE, Guyenet PG. Photostimulation of retrotrapezoid nucleus phox2b-expressing neurons in vivo produces long-lasting activation of breathing in rats. *J. Neurosci.* **29**, 5806-5819 (2009).

[99] Nisimaru N, Okahara K, Yanai S. Cerebellar control of the cardiovascular responses during postural changes in conscious rabbits. *Neurosci. Res.* **32**, 267-271 (1998).

[100] Yoshihara Y, Mizuno T, Nakahira M, Kawasaki M, Watanabe Y, Kagamiyama H, Jishage K, Ueda O, Suzuki H, Tabuchi K, Sawamoto K, Okano H, Noda T,Mori

K. A genetic approach to visualization of multisynaptic neural pathways using plant lectin transgene. *Neuron* **22**, 33-41 (1999).

[101] Sawada Y, Kajiwara G, Iizuka A, Takayama K, Shuvaev AN, Koyama C, Hirai H. High transgene expression by lentiviral vectors causes maldevelopment of Purkinje cells in vivo. *Cerebellum* **9**, 291-302 (2010).

[102] Geurts FJ, Timmermans J, Shigemoto R, De Schutter E. Morphological and neurochemical differentiation of large granular layer interneurons in the adult rat cerebellum. *Neuroscience* **104**, 499-512 (2001).

[103] Granit R, Phillips CG. Excitatory and inhibitory processes acting upon individual Purkinje cells of the cerebellum in cats. *J. Physiol.* **133**, 520-547 (1956).

[104] Eccles JC, Llinas R, Sasaki K. The excitatory synaptic action of climbing fibres on the purinje cells of the cerebellum. *J. Physiol.* **182**, 268-296 (1966).

[105] Doba N, Reis DJ. Cerebellum: role in reflex cardiovascular adjustment to posture. *Brain Res.* **39**, 495-500 (1972).

[106] Mandolesi G, Autuori E, Cesa R, Premoselli F, Cesare P, Strata P. GluRdelta2 expression in the mature cerebellum of hotfoot mice promotes parallel fiber synaptogenesis and axonal competition. *PLoS One* **4**, e5243 (2009).

[107] Russo AF, Crenshaw EB 3rd, Lira SA, Simmons DM, Swanson LW, Rosenfeld

MG. Neuronal expression of chimeric genes in transgenic mice. *Neuron* **1**, 311-320 (1988).

[108] Frecha C, Szécsi J, Cosset FL, Verhoeyen E. Strategies for targeting lentiviral vectors. *Curr. Gene Ther.* **8**, 449-460 (2008).

[109] Schmolesky MT, Weber JT, De Zeeuw CI, Hansel C. The making of a complex spike: ionic composition and plasticity. *Ann. N Y Acad. Sci.* **978**, 359-390 (2002).

[110] Davie JT, Clark BA, Häusser M. The origin of the complex spike in cerebellar Purkinje cells. *J. Neurosci.* **28**, 7599-7609 (2008).

[111] Llinás R, Sugimori M. Electrophysiological properties of in vitro Purkinje cell somata in mammalian cerebellar slices. *J. Physiol.* **305**, 171-195 (1980).

[112] Miall RC, Keating JG, Malkmus M, Thach WT. Simple spike activity predicts occurrence of complex spikes in cerebellar Purkinje cells. *Nat. Neurosci.* **1**, 13-15 (1998).

[113] Ekerot CF, Oscarsson O. Prolonged depolarization elicited in Purkinje cell dendrites by climbing fibre impulses in the cat. *J. Physiol.* **318**, 207-221 (1981).

[114] Orduz D, Llano I. Recurrent axon collaterals underlie facilitating synapses between cerebellar Purkinje cells. *Proc. Natl. Acad. Sci. U S A* **104**, 17831-17836 (2007).

[115] Stoney SD Jr, Thompson WD, Asanuma H. Excitation of pyramidal tract cells by intracortical microstimulation: effective extent of stimulating current. *J. Neurophysiol.* **31**, 659-669 (1968).

[116] Harvey RJ, Napper RM. Quantitative study of granule and Purkinje cells in the cerebellar cortex of the rat. *J. Comp. Neurol.* **274**, 151-157 (1988).

[117] Aravanis AM, Wang LP, Zhang F, Meltzer LA, Mogri MZ, Schneider MB, Deisseroth K. An optical neural interface: in vivo control of rodent motor cortex with integrated fiberoptic and optogenetic technology. *J. Neural. Eng.* **4**, S143-156 (2007).

[118] Yates BJ. Vestibular influences on the autonomic nervous system. *Ann. N Y Acad. Sci.* **781**, 458-473 (1996).

[119] Yakhnitsa V, Barmack NH. Antiphasic Purkinje cell responses in mouse uvula-nodulus are sensitive to static roll-tilt and topographically organized. *Neuroscience* **143**, 615-626 (2006).

[120] Crusio WE, Schwegler H, Abeelen JHF Behavioral responses to novelty and structural variation of the hippocampus in mice. I. Quantitative-genetic analysis of behavior in the open-field. *Behav. Brain Res.* **32**, 75-80 (1989).

[121] Henry RT, Connor JD, Balaban CD. Nodulus-uvula depressor response: central

GABA-mediated inhibition of alpha-adrenergic outflow. *Am. J. Physiol.* **256**, H1601-1608 (1989).

[122] Doba N, Reis DJ. Role of the cerebellum and the vestibular apparatus in regulation of orthostatic reflexes in the cat. *Circ. Res.* **40**, 9-18 (1974).

[123] Koyama S, Ammons WS, Manning JW. Visceral afferents and the fastigial nucleus in vascular and plasma renin adjustments to head-up tilting. *J. Auton. Nerv. Syst.* **4**, 381-392 (1981).

[124] Konermann S, Brigham MD, Trevino AE, Hsu PD, Heidenreich M, Cong L, Platt RJ, Scott DA, Church GM, Zhang F. Optical control of mammalian endogenous transcription and epigenetic states. *Nature* **500**, 472-6 (2013).

7. Acknowledgement

I thank Prof. Yasushi Miyashita for supervision, Drs. Masao Ito (RIKEN Brain Science Institute, Saitama, Japan), Naoko Nisimaru (Oita University, Oita, Japan) and Yasuo Ohashi (Department of Public Health, The University of Tokyo School of Medicine, Tokyo, Japan) for helpful comments to the manuscript, Drs. Hideki Kashiwadani (Department of Physiology, The University of Tokyo School of Medicine), Masanori Matsuzaki (National Institute for Basic Biology, Aichi, Japan), Shinichi Watanabe (Department of Physics, The University of Tokyo School of Science), Hiroshi Kawasaki (Department of Biophysical Genetics, Graduate School of Medical Sciences, Kanazawa University, Ishikawa, Japan), Manabu Tanifuji (RIKEN Brain Science Institute, Saitama, Japan) for technical advice, Dr. Karl Deisseroth (Stanford University) for the pcDNA3.1-hChR2-EYFP and pLenti-CaMKIIα-eNpHR-EYFP-WPRE plasmids, Dr. Yoshihiro Yoshihara for the pL7-tWGA plasmid and Dr. Ryuichi Shigemoto for the anti-mGluR2 monoclonal antibody. The St. Jude lentiviral vector system was kindly provided by St. Jude Children's Research Hospital (Dr. Arthur W. Nienhuis) and George Washington University.

Special thanks to members of the Miyashita laboratory, my parents and a sister for generous supports during my doctoral course.